Alma Mater Studiorum - Università di Bologna

DOTTORATO DI RICERCA IN

GEOFISICA

Ciclo 34

Settore Concorsuale: 02/C1 - ASTRONOMIA, ASTROFISICA, FISICA DELLA TERRA E DEI PIANETI

Settore Scientifico Disciplinare: FIS/06 - FISICA PER IL SISTEMA TERRA E IL MEZZO CIRCUMTERRESTRE

COMPREHENSIVE CHARACTERIZATION OF SNOWFALL IN TERMS OF MICROPHYSICAL FEATURES, QUANTITATIVE PRECIPITATION ESTIMATION AND SCAVENGING PROPERTIES BY IN SITU AND REMOTE SENSING OBSERVATIONS AT AN ANTARCTIC COASTAL SITE

Presentata da: Alessandro Bracci

Coordinatore Dottorato

Nadia Pinardi

Supervisore

Federico Porcù

Co-supervisore

Luca Baldini

Esame finale anno 2022

Abstract

Snow plays a crucial role in the Earth's hydrological cycle and energy budget, making its monitoring necessary. In this context, ground-based radars and in situ instruments are essential thanks to their spatial coverage, resolution, and temporal sampling. Deep understanding and reliable measurements of snow properties are crucial over Antarctica to assess potential future changes of the surface mass balance (SMB) and define the contribution of the Antarctic ice sheet on sea-level rise. However, despite its key role, Antarctic precipitation is poorly investigated due to the continent's inaccessibility and extreme environment. In this framework, this Thesis aims to contribute to filling this gap by in-depth characterization of Antarctic precipitation at the Mario Zucchelli station from different points of view: microphysical features, quantitative precipitation estimation (QPE), vertical structure of precipitation, and scavenging properties. For this purpose, a K-band vertically pointing radar collocated with a laser disdrometer and an optical particle counter (OPC) were used. The radar probed the lowest atmospheric layers with high vertical resolution, allowing the first trusted measurement at only 105 m height. Disdrometer and OPC provided information on the particle size distribution and aerosol concentrations. An innovative snow classification methodology was designed by comparing the radar reflectivity (*Ze*) and disdrometer-derived reflectivity by means of DDA simulations. Results of classification were exploited in QPE through appropriate *Ze*-snow rate relationships. The accuracy of the resulting QPE was benchmarked against a collocated weighing gauge. Vertical radar profiles were also investigated to highlight hydrometeors' sublimation and

growth processes. Finally, OPC and disdrometer data allowed providing the first-ever estimates of scavenging properties of Antarctic snowfall. Results presented in this Thesis give rise to advances in knowledge of the characteristics of snowfall in Antarctica, contributing to a better assessment of the SMB of the Antarctic ice sheet, the major player in the global sea-level rise.

Contents

List of Figures

List of Tables

Chapter 1

1 Introduction

1.1 Role and Importance of Antarctica in the Earth System

The Antarctic Continent and the Southern Ocean are critical drivers of the Earth's atmospheric and oceanic systems, and the processes occurring in these regions are known to play a significant role in the global climate system (Mayewski et al., 2009; Cavanagh et al., 2021; Choudhary and Khare, 2022). The Southern Ocean is the primary source of much of the oceans' deep water and provides the primary return pathway for this deep water to the surface (Frölicher et al., 2015; Gjermundsen et al., 2021; Li et al., 2021; Auger et al., 2021). The upwelling waters represent a primary source of nutrients and a significant sink of $CO_{2,}$ making the Southern Ocean the most biologically productive ocean (Sarmiento et al., 2004; Marshall and Speer, 2012; Hong et al., 2021; Joy-Warren, 2021) and, at the same time, by far the most significant conduit by which anthropogenic CO_2 enters the ocean system (Khatiwala et al., 2009; Hong et al., 2021).

The Antarctic Continent represents about 10% of the Earth's land surface (14 million km^2). Along with its surrounding sea ice, Antarctica plays a significant role in the radiative forcing of high southern latitudes and is a critical driving component for atmospheric circulation (Mayewski et al., 2009; Turner et al., 2009; Choudhary and Khare, 2022). Thick ice sheet (the so-called Antarctic Ice Sheet-AIS) covers almost the whole continent (around 98%) with an ice volume of approximately 27 million km^3 (Fretwell et al., 2013), and it contains more than 70% of the world's

freshwater resources (Jia et al., 2022; Pan et al., 2022). AIS deeply drives the Antarctic climate, influencing the Southern Hemisphere temperatures and stabilizing the cyclone tracks around the continent (Mayewski et al., 2009). Due to the peculiar climate, the Antarctic continent also experienced the strongest depletion of the stratospheric ozone layer when photochemical processes together with a unique set of meteorological conditions led to a significant increase in the effectiveness of ozone-depleting gases and more than half of the total overhead ozone was destroyed (Thompson et al., 2011; Choudhary and Khare, 2022).

Recently, the polar regions are increasingly recognized as being geopolitically and economically significant but, at the same time, extraordinarily vulnerable and affected by current and projected climate change (Johnston, 2009; Wehrmann, 2018; Didenko and Cherenkov, 2018; McGee et al., 2022). The Poles are also regions with the greatest potential to condition global climate and thus human populations and biodiversity (IPCC, 2007; Werner, 2021; Worm and Lotze, 2021). In particular, AIS probably represents the most critical factor and an essential contributor to the global sea-level rise considering its volume is equivalent to about 58 meters on global mean sea level rise (Vaughan et al., 2013). Furthermore, current estimates have linked the 10% of the observed sea-level rise since 1993 to the Antarctic continent, and its contribution is still increasing (Mottram et al., 2021).

In order to assess the AIS contribution to sea-level rise, the understanding of its surface mass balance (SMB) is of crucial importance (Souverijns et al., 2018a; Kim et al., 2020; Hansen et al., 2021). In general, to monitor and study a glacier's stability and evolution, the knowledge of its surface mass balance is essential. The mass balance is defined as the difference between accumulation and ablation at the

surface of a glacier and represents a measure of the change in mass of a glacier over a period of time, also providing the link between the glacier and the local climate (Van Tricht et al., 2021). Analyzing SMB data contributes to understanding variations in a glacier system, finding out the reasons for which a glacier is advancing or retreating, and suggesting the responsible processes (Cogley et al., 2010; Smith et al., 2020).

In response to the increase of global mean temperature, several studies pointed out that global glaciers show negative SMB during the last decades, corresponding to a 27 ± 22 mm contribution to global sea level (Zemp et al., 2019; Wouters et al., 2019). Furthermore, according to Rignot et al. (2019) and Shepherd et al. (2020), even the AIS has been having net mass loss since 2002, with evidence for higher mass-loss rates during 2005–2010 (Previdi and Polvani, 2016).

In this framework, the measurements and estimates of the local SMB are crucial for understanding changes in the total mass of the AIS, thus including its contribution to sea-level rise (Souverijns et al., 2018a; Kittel et al., 2021). Surface snow accumulation is the primary mass input to the Antarctic ice sheets (Bromwich et al., 2004; Kittel et al., 2018). Snow accumulation is derived primarily from solid precipitation, the dominant term among the various components of surface snow accumulation: precipitation, sublimation/vapor deposition, and snowdrift (Bromwich, 1988; Kittel et al., 2018; Gilbert and Kittel, 2021). Therefore, its spatial and temporal variability is necessary to assess the surface mass balance, making the in-depth knowledge of precipitation over the Antarctic continent crucial to quantifying the mass balance of the AIS and its contribution to global sea-level change (Bromwich et al., 2004).

1.2 Snowfall: a challenge for remote sensing and in situ measurements

Snow plays a crucial role in climate and weather, influencing the hydrological cycle and the energy budget of the Earth system (Field and Heymsfield, 2015; Levizzani et al., 2020; Heymsfield et al., 2020). In addition, snowfall is a reservoir of fresh water and sensibly affects human activities impacting infrastructures, commerce, energy, and the environment (Vajda, 2015; Croce et al., 2018; Rome et al., 2019), prompting for continuous improvements of techniques for measurements and now/forecasting of snowfall events, in which operational and scientific communities are deeply committed. In this framework, the use of remote sensing instruments for snowfall observations is essential since, in principle, it ensures the necessary spatial coverage and temporal sampling for monitoring purposes. Among such instruments, scanning radars have the unique capability of describing the three-dimensional structure of precipitating systems, while radar profilers provide frequent high-resolution measurements along the vertical axis, yielding insights into vertical structures. Despite such importance, the ability to measure snowfall rate, accumulation, and physical properties is still inadequate depending on the instrument used and environmental conditions (Rasmussen et al., 2012). Quantitative estimation of snowfall rate using meteorological radars is by far more challenging than the estimation of rainfall rate because the solid phase of precipitation adds several uncertainties, primarily due to the sizeable microphysical variability of hydrometeors such as habits, shapes, orientation, fall behavior, and density (Mitchell et al., 1990; Mitchell, 1996; Pruppacher and Klett, 2010; von

Lerber et al., 2017). Moreover, snowfall rate measurements performed by in situ ground-based instruments, usually taken as reference for remote sensing estimates, are particularly prone to the wind-induced under-catch caused by the limited mass and low falling velocity of ice hydrometeors compared to the liquid ones (Rasmussen et al., 2012), and are also affected by blowing snow effect (Naaim-Bouvet et al., 2014; Seefeldt et al., 2021).

Focusing on the Antarctic continent, the properties of precipitation remain largely unknown (Grazioli et al., 2017b), and its rate and amount are not well-estimated by numerical weather/climate models or satellite measurements, although some progress has been made recently (Palerme et al., 2014; Milani et al., 2018). In addition, the difficulty in obtaining continuous snowfall measurements on the ground due to complex logistical operations, instrument maintenance (Knuth et al., 2010), and extreme climatic conditions (Scarchilli et al., 2010) should be taken into account. However, the knowledge of precipitation amounts is of particular interest in Antarctica. Solid precipitation is indeed the most important positive term of the surface mass balance of the Antarctic Ice Sheet (Van Wessem et al., 2014; Turner et al., 2019) with respect to the various components of the surface snow accumulation (precipitation, sublimation/vapor deposition, and snowdrift). In fact, AIS plays a significant role in global climate variability and could represent a significant contributor to sea-level rise (DeConto and Pollard, 2016; Shepherd et al., 2018). Moreover, mean precipitation and precipitation intensity are projected to increase during the 21st century, according to the Sixth Assessment Report of the Intergovernmental Panel on Climate Change (IPCC, 2021; Ranasinghe et al., 2021). Furthermore, the Antarctic water cycle knowledge is essential even for assessing

the lower atmosphere's radiative budget and evaluating the ice sheet variation and the surface mass balance (Scarchilli et al., 2011; Gorodetskaya et al., 2015).

1.3 The role of snowfall as aerosol sink

Besides having a crucial role in climate and weather patterns, snowfall is also heavily involved in removing aerosol particles in the atmosphere.

The removal of below-cloud aerosol particles by precipitation, either rain or snow, decreases particulate matter concentrations and contributes to the wet deposition of pollutants (Wang et al., 2014). The below cloud scavenging process (from now on BCS) has been identified as one of the most efficient removal mechanisms for atmospheric particles (Textor et al., 2006).

Atmospheric aerosol can be defined as a collection of fine solid particles or liquid droplets in a volume of air (Seinfeld and Pandis, 2008). They are characterized by dimensions ranging between about 0.01 and 100 μm, whereas their atmospheric residence time goes from a few hours to several days. In spite of their scarcity in terms of mass, they are of crucial importance in the climate and biogeochemical systems, besides contributing to the most significant uncertainty in the global radiative forcing (Loeb and Su, 2010). The comprehensive knowledge of atmospheric aerosol is still an open issue due to inherent large variability and complexity in terms of sources (Calvo et al., 2013).

The characterization of aerosol sources and sinks plays a crucial role in studying atmospheric aerosols and pollution (Blanco-Alegre et al., 2018). The scavenging of aerosol particles by dry deposition and wet depositions represents one of the sinks

of atmospheric aerosols, besides being a critical process for maintaining a balance between the sources and sinks of aerosol particles (Andronache, 2003). Wet deposition includes several natural processes by which gases and aerosol particles can be removed from the atmosphere and deposited to the Earth's surface. These removal mechanisms are driven by ice particles or liquid water drops inside the clouds and/or by solid/liquid precipitation hydrometeors just below clouds (Seinfeld and Pandis, 2008). Usually, the former process is called rain-out and refers to in-cloud scavenging, whereas wash-out or below-cloud scavenging phenomena involve falling particles. Both these processes contribute to the wet deposition during a precipitation episode. Indeed, the gases can be dissolved into clouds, and aerosol particles can serve as cloud condensation nuclei for the formation of cloud droplets, remaining trapped inside.

Similarly, raindrops or snowflakes can remove particles via collision or dissolution of water-soluble gaseous pollutants during their fall towards the ground. Since hydrometeors can capture large amounts of gases and particles, the BCS tends to be the most critical process, and it is also crucial for cleansing the atmosphere from what is generally called pollutants, although this mechanism can lead to significant effects and impacts on the ground (e.g., acid rains) (Chate et al., 2011; Chate, 2011; Zhao et al., 2015). Moreover, BCS of aerosol particles by snow is an essential mechanism of wet deposition in mid-latitude, polar, and mountainous regions (Paramonov et al., 2011). As mentioned above, wet removal systems depend on multiple and composite processes. For these reasons, the complete understanding of wet deposition processes is one of the most challenging in atmospheric sciences.

1.4 State of the art

Ground-based measurements from vertically pointing radar, coincident observations from disdrometer, and backscattering simulations are commonly used to quantitatively estimate solid precipitation from radar observations (Souverijns et al. (2017), Falconi et al. (2018), Genthon et al. (2018), Schirle et al. (2019), Scarchilli et al. (2020), Capozzi et al. (2020), among others). In such cases, QPE is commonly obtained by comparing radar measurements and other ground sensors data: the equivalent radar reflectivity factor (*Ze*) is linked to the liquid-equivalent snowfall rate (*SR*) by means of a power-law relationship ($Ze = a \times SR^b$). However, due to the high variability of the microphysics of the hydrometeors, such relationship cannot be univocal, resulting in significant uncertainty of the a and b parameters in the *Ze-SR* relationship (Matrosov, 2007).

Previous studies on snowfall QPE have proposed and validated various *Ze-SR* relationships based on different snowflake habits and properties, also associating reflectivity observations from meteorological radar to ground measurements from snow-gauge, disdrometer, as well as snowflake numerical modelling. For example, Falconi et al. (2018) derived *Ze-SR* relationships testing the consistency of simultaneous observations of radar and a Particle Imaging Package (PIP) video-disdrometer and distinguishing the different degrees of riming for snowflakes and different radar frequencies. (Matrosov, 2007) explored W- and Ka-frequencies to derive *Ze-SR* relationships accounting for the aspect ratio of the particles and changes in velocity-diameter and mass-diameter relationships, using aggregate and single-crystal dendrite snowflake properties. Results once more showed the substantial variability of the *Ze-SR* coefficients, which can result in up to a factor

of 2 in the estimated snowfall rates. According to Matrosov et al. (2009), six *Ze-SR* formulas, derived under different microphysical assumptions, were used to measure snowfall amounts in the US. The comparison of the results with a hot-plate instrument (Rasmussen et al., 2002), taken as reference, confirmed a wide variability of *Ze-SR* coefficients. Finally, focusing on the Antarctic continent, Grazioli et al. (2017a) investigated the snowfall amount at the Dumont D'Urville station through seven different *Ze-SR* relationships resulting in a wide range of the total accumulated values.

Therefore, it is worth underlining that, in determining the *Ze-SR* relationship suitable for a specific site for QPE purposes, one can find different parameters for different snowfall events (Huang et al., 2010). However, since the atmospheric conditions and particle habits often change, even at the temporal scale of a few minutes (von Lerber et al., 2017), the choice of the specific *Ze-SR* to be used is not a trivial matter.

Nevertheless, QPE retrievals can be substantially improved by using adjustable *Ze-SR* relationships (von Lerber et al., 2017), determining a proper real-time relationship (Rasmussen et al., 2003), or adopting a variable *Ze-SR* relationship based on temperature profile as in the CloudSat Snow Profile satellite product (2C-SNOW-PROFILE) (Wood, 2011; Wood et al., 2013). Moreover, since most of the uncertainty of the relationship lies in the prefactor a, linked to the assumed *m(D)*, i.e., the mass-diameter relationship of particles (von Lerber et al., 2017), the knowledge of falling habit is expected to contribute to a more precise definition of the *Ze-SR* parameters. However, only specific radar measurements, such as dual-polarization scanning radar or multi-frequency Doppler profilers, make it possible

to clearly distinguish among the various types of hydrometeors (Rasmussen et al., 2003; Chandrasekar et al., 2013; Li et al., 2020).

Commonly, the below-cloud scavenging of precipitation is assessed by means of the scavenging coefficient (λ). This parameter is widely used in aerosol experimental studies as well as in aerosol chemical transport models to describe the BCS of aerosol particles by rain and snow (Paramonov et al., 2011; Wang et al., 2014). Aerosol observations in terms of number concentration provided by an Optical Particle Counter (from now on OPC) are coupled with disdrometer measurements to evaluate changes in aerosols counting during precipitation events. Several works in literature have calculated scavenging coefficients for the aerosol particles measured in case of rainfall (Andronache, 2003; Castro et al., 2010; Duhanyan and Roustan, 2011; Chate et al., 2011; Bae et al., 2012; Li et al., 2016; Blanco-Alegre et al., 2018; Cugerone et al., 2018a,b; Luan et al., 2019; Blanco-Alegre et al., 2019). However, very few studies have dealt with snow (Kyrö et al., 2009; Paramonov et al., 2011; Zikova and Zdimal, 2016), and, to the best of my knowledge, no works have been performed for assessing the BCS in terms of scavenging coefficients using ground-based instrumentation in Antarctica. On the contrary, aerosol and snowfall chemistry were instead widely investigated, even sampling fresh snow at the ground (e.g., Hillamo et al., 1998; Wolff et al., 1998; Legrand et al., 1999; Tomasi et al., 2007).

1.5 Motivation and Aim of the Thesis

This Thesis proposes a novel and innovative insight into Antarctic precipitation focusing on microphysical features, quantitative precipitation estimation (QPE) at the ground and height, and sublimation and scavenging processes.

In this context, the Thesis aims to highlight how the synergic use of a ground-based disdrometer, a K-band vertically pointing radar, the knowledge of particle scattering properties, and aerosols concentrations can be used to derive different *Ze-SR* relationships, based on a classification of the particle habits of the falling hydrometeors, to explore the vertical structure of precipitation, and to calculate the BCS coefficients.

Focusing on the Antarctic region, this Thesis also intends to develop an accurate snowfall rate estimation strategy and validate it for Antarctic precipitation, to enhance the knowledge in sublimation processes of precipitation, and to provide the first assessment for BCS coefficients in Antarctica, which represents an ideal site to investigate natural background processes being geographically far from any anthropogenic emissions.

For such purposes, data by a Parsivel disdrometer (OTT GmbH) and a co-located K-band Micro Rain Radar (Metek GmbH) collected during austral summer periods 2018–2019 and 2019–2020 and data by Parsivel and OPC-N2 (Alphasense Ltd.) collected during austral summer period 2020–2021, were handled and processed. Measurements were carried out at the Italian Antarctic station "Mario Zucchelli" (MZS) in the framework of the long-term project APP (Antarctic Precipitation Properties) funded by the Italian PNRA-National Antarctic Research Program. This Thesis presents a new approach to the radar QPE in Antarctica and, more generally,

for solid precipitation estimation making use of detailed information from snow particle size distribution (PSD) and radar reflectivity close to the ground coupled with discrete dipole approximation (DDA) backscattering simulations. Finally, this Thesis provides the first quantification of scavenging processes at MZS using aerosol observations in terms of particle concentrations.

1.6 Outline

The Thesis is organized as follows. In Chapter 2, a theoretical background is set out, divided into two main sections. First, the solid precipitation microphysics is deeply discussed, then the precipitation scavenging theory is provided. Chapter 3 describes the MZS site, the experimental deployment, the database of the properties of the solid hydrometeors, and the datasets used. Moreover, the methodologies followed in hydrometeor classification and disdrometer data correction are set out, underlining their novelty with respect to other state-of-the-art techniques. In addition, the approach to evaluate and use the OPC measurements for scavenging investigation is explained. Chapter 4 presents, discusses and evaluates the main results. Finally, in Chapter 5, the conclusions are drawn, underlining the main findings and the potential of the proposed methods.

Chapter 2

2 Theoretical Background

2.1 Solid Precipitation Microphysics

A necessary condition for precipitation formation is that the air becomes saturated with water vapor, and clouds form. Precipitation particles grow in the clouds by the complex interplay of different mechanisms until the particles become heavy and large enough to reach the ground (i.e., “to precipitate”). This mechanism involves several processes driving the growth and evolution of the precipitation event.

Generally, two alternative microphysical conceptual models describe precipitation processes and make the matter more accessible: warm and cold rain. Warm rain takes place in clouds where the temperatures are above the freezing level, so no ice phase particles are involved in the process (Lau and Wu, 2003): collision and coalescence of water droplets of different dimensions and terminal velocity are the dominant mechanisms for the growth of the cloud elements to reach the size of precipitation elements. For example, in some regions such as the Tropics, strong instability-driven vertical currents promote rain formation, allowing a large number of water droplets to grow and become raindrops in a relatively short time (around 20 minutes).

The conceptual model of the cold rain is instead referred to processes that take place (all or in part) above the freezing level (i.e., at a temperature below 0°C), in clouds formed by different types of ice crystals and/or supercooled liquid droplets (Wang and Georgakakos, 2005). Ice particles overgrow to the detriment of moisture of the

cloud droplets, according to the Wegener-Bergeron-Findeisen (WBF) process, due to the differences in the equilibrium vapor pressures between ice and liquid water (Glickman and Zenk, 2000). However, it is worth underling that in nature, the mentioned differences between warm and cold rain are not so clearly distinguishable, and therefore there is always considerable uncertainty in detecting warm and cold rain processes.

2.1.1 Ice Nucleation and Ice Nuclei in the atmosphere

Ice formation in clouds is of vital importance to life on Earth, as ice formation is one of the key processes initiating precipitation. A large fraction of Earth's rain originates as snow that melts before reaching the ground (Field and Heymsfield, 2015). Therefore ice nucleation can be considered the starting mechanism that leads to precipitation, so much that the poorly understood processes of ice initiation and secondary ice multiplication in clouds result in significant uncertainties in modeling precipitation production and predicting climate changes (Heymsfield and DeMott, 2010).

The formation of ice in clouds can take place in two ways: primary processes (nucleation of ice from the liquid or water vapor phases), either homogeneously or heterogeneously triggered by aerosol particles called ice nuclei (IN) (Santachiara et al., 2014) and secondary processes in which single ice crystals may act as IN, favoring the generation and the nucleation of new ice particles in certain conditions. The homogeneous freezing of a tiny water droplet occurs when random fluctuations of water molecules produce a structure acting as IN. The result is that enough water molecules stick together within the droplet to form an ice structure that leads to the

ice particle formations. Similar to the homogeneous nucleation of the cloud drops from water vapor, the size and probability of the formation of the starting ice structure act as critical factors connected to the solid-liquid interfacial free energy. Since the formation of ice particles in the atmosphere takes place more efficiently through heterogeneous nucleation, it is relatively rare to observe homogeneous nucleation that needs very low atmospheric temperatures (around -40°C). Indeed ice phase is commonly observed in the atmosphere as cloud temperature approaches -20°C because of heterogeneous nucleation (Pruppacher and Klett, 2010).

The formation of ice crystals can also be promoted by homogeneous depositions, namely random collisions of water vapor molecules resulting in a stable ice embryo. However, this mechanism is quite ineffective in the atmosphere as it needs very high levels of supersaturation, where, instead, atmospheric values rarely exceed the values of 1-2% with respect to the water due to the more efficient heterogeneous nucleation of liquid droplets that starts at lower values of atmospheric saturation (Liou and Yang, 2016).

Furthermore, the heterogeneous nucleation (nucleation beginning at the surface of an IN) depends on the nature of the particles, but it generally acts several degrees below the freezing point. Temperatures around -20°C are needed for heterogeneous nucleation and are assumed as a threshold for this mechanism. The probability of efficient nucleation most relies on the IN's chemical properties and crystal structures, besides the atmospheric temperature. The more tightly bound the water molecules are to the foreign particles, the greater the probability of ice nucleation (Liou and Yang, 2016). Nevertheless, INs are quite rare in the atmosphere compared to the cloud condensation nuclei, as they generally represent only 1 out

of 10^5 aerosol particles in the free troposphere. However, despite their scarcity, INs can profoundly influence the cold cloud microphysical processes (DeMott et al., 2010). Indeed, supercooled or mixed-phase clouds (consisting of supercooled liquid droplets and ice particles) can occur precisely because of the enormous concentration of aerosol particles in the atmosphere, of which a small percentage acts as ice nuclei.

According to Vali (1985), Murray et al. (2011), and Broadley et al. (2012), four mechanisms can lead to heterogeneous nucleation: deposition, condensation, immersion, and contact. The first mode involves the deposition of ice over solid surface directly from the vapor phase and needs supersaturated conditions with respect to the ice, and it is probably significant in the upper-tropospheric clouds. Ice formation during the condensation of liquid water onto a solid particle represents the second mode. In comparison, immersion occurs when ice nucleates on a solid particle immersed in a supercooled liquid droplet. Finally, when ice nuclei collide or contact the water-air interface, it gives rise to contact mode.

However, heterogeneous ice nucleation remains an enigmatic topic because it involves, as described, multiple mechanistic processes (DeMott et al., 2010) in which immersion mode and contact freezing are thought to be most significant in mixed-phase clouds.

As mentioned above, INs play a vital role in the whole process of precipitation, acting as trigger mechanisms, although their relative scarcity in the atmosphere. Several studies, in both laboratory (Santachiara et al. (2014) among others) and field (e.g., Jiang et al., 2014; Patade et al., 2014), have been carried out to understand the concentration and composition of the ice nuclei more deeply.

Results show that IN number varies as a function of supersaturation and air temperature. Outcomes also point out the significant variability of concentration depending on site. Over the Antarctic continent, studies have found a concentration of 1 IN liter^{-1} at the South Pole Station over the Plateau (Ardon-Dryer et al., 2011) and up to 10 IN liter^{-1} in the Palmer Station in the Antarctic Peninsula (Saxena and Weintraub, 1988). Values ranging from 5 to 35 IN m^{-3} have been found near MZS at a temperature of -17°C (Belosi et al., 2012). Compositions of IN strictly depend on their origin. Sources can be anthropic (Belosi et al., 2014) or natural (e.g., pollen, lichen, fungi, bacteria, soil, clay). Among the latter, the clay minerals, particularly the kaolinite, are particularly effective as IN, with a relatively high activation temperature (Liou and Yang, 2016). Therefore such observations suggest that desert and arid regions can be considered the primary sources of atmospheric IN (Pruppacher and Klett, 2010). Also, biogenic materials, particularly bacteria, are an effective substrate for heterogeneous nucleation being able to catalyse freezing of supercooled droplets at temperatures below 0°C. It is worth underlining that the features of IN are decisively different from those of CCN. Ice nuclei must be water-insoluble, preferably of large dimensions, not necessarily hygroscopic, but having crystallographic features that recall the structure of ice (Wang, 2013).

2.1.2 Secondary ice production

In-cloud measurements of ice crystals show a higher concentration by orders of magnitude than IN concentration, meaning that an efficient mechanism works inside the clouds, producing multiplication of ice particles. The Secondary Ice Production (SIP) can significantly enhance ice particle number concentrations in

mixed-phase clouds, and it is especially important at temperatures warmer than -10°C, for which primary ice nucleation is less effective (Luke et al., 2021). SIP consists of different mechanisms as fracture of ice crystals exposed to dry air layers or collision of pre-existing ice crystal, as fragmentation of large cloud drops during freezing in free fall, or as fragmentation of freezing droplets following their collision with ice particles in the cloud (Santachiara et al., 2014). The best-known mechanism of SIP is the rime-splintering, also known as the Hallett–Mossop process (Field et al., 2016). This process produces small ice splinters during riming and preferably takes place at air temperature between -8°C and -3°C (Luke et al., 2021). New ice crystals are then generated exploiting such fragments as IN.

2.1.3 Growth of ice crystals

It is common knowledge that ice crystals can have a very large variety of habits, shapes, and particle size distributions. This variety depends on ice nuclei's chemical and physical properties and the dynamical and thermodynamic conditions. After nucleation, ice crystals of different habits such as pristine needles, plates, columns, dendrites, and stellar crystals start to grow in accordance with atmospheric temperature and humidity (see Figure 1) (Gultepe et al., 2017). Inside-cloud conditions are particularly favorable for crystal growth as the water-saturated environment is supersaturated in respect to the ice. Since the equilibrium vapour pressure of ice is lower than that of liquid water, this results in a rapid enhancement of crystal dimensions by deposition and diffusion mechanisms. Such processes will last until liquid droplets can evaporate, maintaining an equilibrium saturation condition relative to the water.

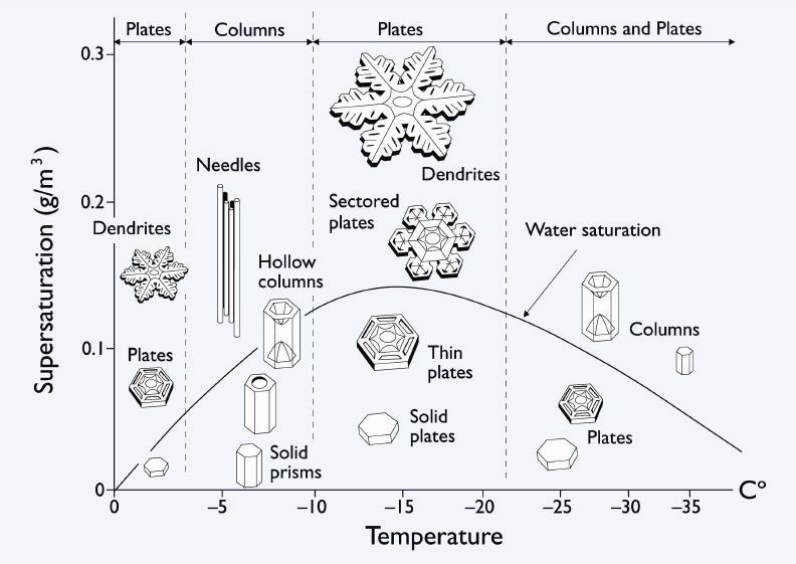

Figure 1 – Snow crystal morphology diagram showing how snow crystal shape or habit changes with temperature and humidity. Source: Libbrecht, (2011).

The growing processes of ice crystals can be mathematically described by an analogy to electrostatics (Pruppacher and Klett, 2010). Given a charged body, if Φ is the electrostatic potential function, then Φ satisfies the Equation of Laplace and the considered boundary conditions, namely $\Phi = \Phi_s$ on the surface and $\Phi = \Phi_\infty$ far away from the charged body. Starting from equations, the governing growth equations can be achieved by replacing the electrostatic potential functions with the vapor density of the environment. Going more into detail, the generalized growth equation can be derived starting from the rate charge change of the spherical conductor exploting the electrostatics analogy again (Wang, 2013). The latter can be expressed as the difference in the potential:

$$\frac{dq}{dt} = 4\pi C(\Phi_\infty - \Phi_s) \qquad (1)$$

where q is the charge of the conductor body, C is the conductor's electrical capacitance, and Φ is the potential on the surface and far away from the body. Therefore, equivalently, the diffusion growth rate (mass over time) of an ice crystal can be calculated by:

$$\frac{dm}{dt} = 4\pi D_v C(\rho_{v,\infty} - \rho_s) \quad (2)$$

The growth rate depends on C, on the vapor diffusivity D_v and the difference in vapor density ρ. C is a function of particle dimension and shape. In the case of a sphere, C is equal to the radius *r*, reducing the Equation to the growth rate of a droplet. Different C values must be used based on the habits and shapes of ice crystals. For example, *C* equals $2r/\pi$ for plate ice crystals, while approximations are needed for more complicated shapes such as the needle or dendrites.

While growing, the crystal surface is heated by the latent heat of sublimation, which increases the ρ_s. The latter reaches a higher value than that at the start of the process. The latent heating rate and the rate of heat transfer away from the crystal surface are balanced, considering stationary growth conditions, and can be expressed as follows:

$$\frac{\rho_v - \rho_s}{T_s - T} = \frac{K}{LD_v} \quad (3)$$

in which the difference in temperature between crystal surface (*Ts*) and air temperature (*T*) is considered, as well as the thermal conductivity coefficient (*K*)

and the latent heat (L). Combining the two previous equations and considering saturation ratio with respect to the ice, the growth rate of an ice crystal can be calculated by the following analytic Equation:

$$\frac{dm}{dt} = \frac{4\pi C\ (S_i - 1)}{\left(\frac{L}{R_v T} - 1\right)\frac{L}{KT} + \frac{R_v T}{e_i(T) D_v}} \tag{4}$$

where S_i is the ratio between environment vapor pressure (e) and the saturation pressure relative to the ice (e_i), and R_v is the gas constant. This Equation represents the basic model of the Wegener Bergeron Findeisen mechanism in which tiny ice crystals grow to the detriment of the supercooled droplets. However, this model does not consider ventilation and kinetic effects that are not negligible in the growth of ice crystals, leading instead to an increase in the growth rate. Furthermore, experimental studies on small ice crystals showed that the growth rate is about half what is predicted by the equations (Fukuta, 1969), while large crystals result in accordance with the theoretical growth rate.

2.1.4 Additional growth mechanisms

The growth of the ice crystal through diffusion processes is by far more efficient than in the liquid drop formation in which the collision and coalescence mechanism takes the leading role. However, in the mixed-phase conditions (i.e., at temperatures where supercooled water drops coexist with ice particles), ice crystals can collide with cloud drops and other ice particles, besides growing by water vapor diffusion. Collisions with supercooled water drops result in the so-called riming process in

which drops freeze on the ice surface, causing an increase of particle dimensions and forming graupels, soft hail, and snow or ice pellets. As a result, ice crystals have lost their pristine identity in these solid hydrometeors, which appear white and opaque because of air intrusions.

On the other hand, ice crystals dimensions can increase by colliding and capturing other crystals, a mechanism known as clumping, resulting in aggregates of crystals (i.e., snowflakes). However, collisions between crystals do not always result in snowflakes, as crystals can stick together but also interlock without cohesion or bounce apart (Wang, 2013).

The clumping process depends on crystals' fall speed and, mainly, on the air temperature (Brandes et al., 2008; Liou and Yang, 2016). An increase of the aggregation efficiency with the temperature was indeed observed, explaining the maximum dimensions of snowflakes at temperatures around 0° C (Magono, 1960), even though large dimensions were also observed for temperatures ranging between -5° and -15°C (Brandes et al., 2008). Snowflakes usually consist of an aggregation of planar snow crystals with dendritic habits that tend to adhere to each other due to the tangle after collisions. Aggregates of needles were also observed, while aggregates of plates and columns rarely appear as they tend to reject each other (Wang, 2013).

2.1.5 Habits and shapes of ice crystals

As mentioned above, atmospheric temperature and saturation drive the growth rate from the water vapor of an ice crystal, creating a snow crystal (or snowflake). On the other hand, atmospheric conditions also drive the preferential growth pattern of

ice crystals, resulting in an instability of the morphology of the crystals and leading to a variety of crystals with different microphysical features. Different researches have been carried out on crystals' habits using theoretical and experimental approaches or combining the two methods. Pruppacher and Klett (2010) report several works in this respect, and most of them have tried to describe such variety of shapes by a simple diagram that links atmospheric conditions (i.e., temperature and saturation) with the morphology of the crystals and to attempt an initial classification of snowflakes at the ground. For instance, Magono and Lee (1966) tried to classify ice crystals by combining snowfall observations at the ground, obtaining 80 distinct shapes, summarized in 8 principal snow categories (needles, column, plate, column and plate combination, side plane, rime, irregular, germ). Bailey and Hallett (2009) noted that the habit prediction from the traditional habit diagrams existing in the literature often disagreed with in situ observations at temperatures below −20°C, while recent laboratory and in situ studies have achieved a consensus on atmospheric ice crystal habits that differs from the traditional habit diagrams. They combined literature with recent studies to draw a comprehensive description of ice crystal habits for the atmosphere as a function of temperature and supersaturation for temperatures ranging from 0° to −70°C and ice supersaturation from 0.1 to 0.6.

Results are summarized in the diagram in Figure 2. The new habit diagram is similar to those in the literature for temperatures from 0°C to -22°C (from plates (0° to −4°C) to columns (−4° to −8°C) to plates (−8° to −22°C)). However, it differs for the lower temperature. Moreover, it is worth underlining the close relationship between supersaturation and crystal shape, as a habit may be different at the same

temperature due to a change in the supersaturation value. At higher temperatures, also single crystals (pristine) can appear. However, the natural snow crystals are dominated by polycrystalline forms (Libbrecht, 2005). These complex habits are often mistakenly identified as aggregates that form because of different mechanisms (i.e., accretion processes) (Bailey and Hallett, 2009).

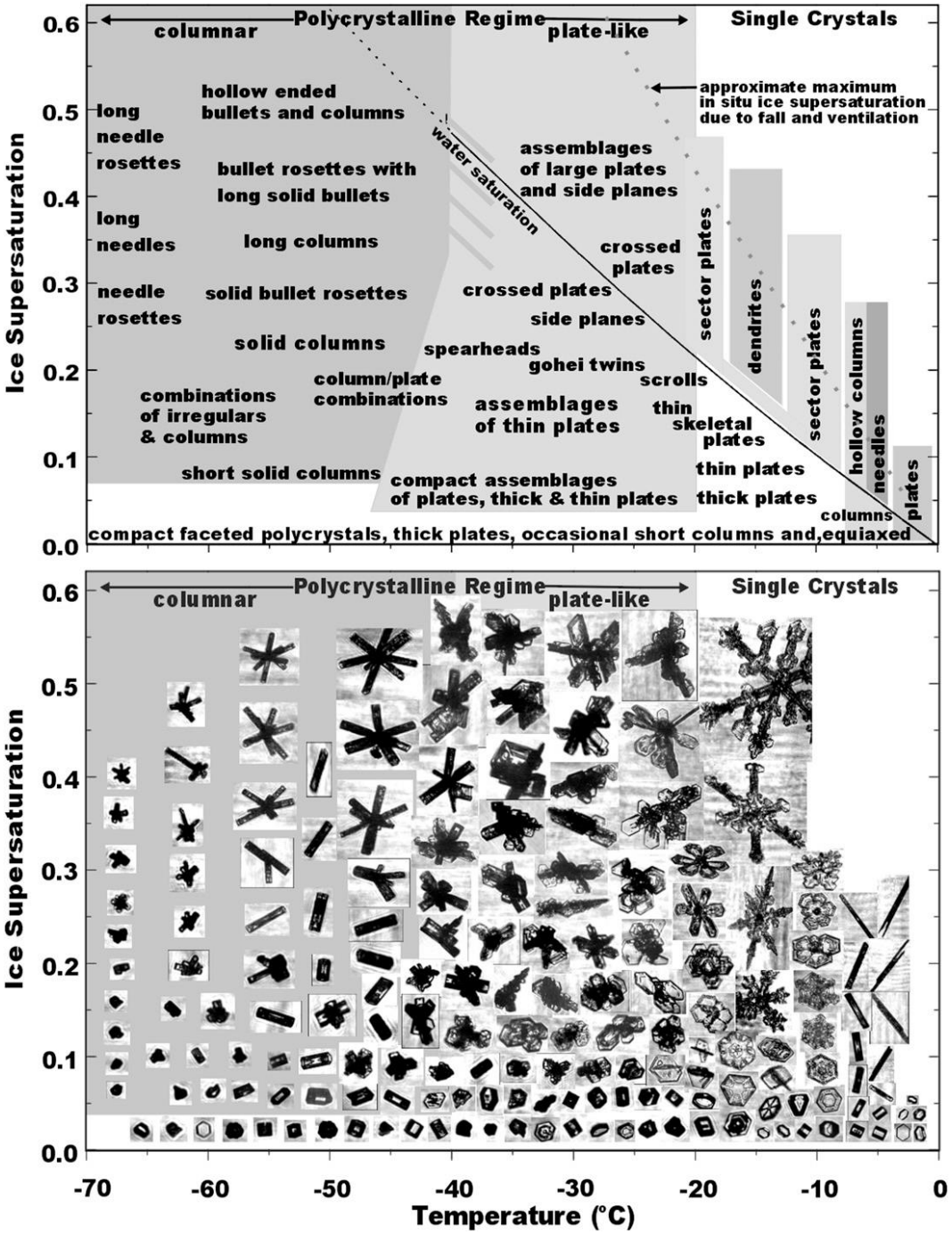

Figure 2 - Habit diagram in text and pictorial format for atmospheric ice crystals. Source: Bailey and Hallett (2009).

2.1.6 Microphysical properties

The large variety in shapes and habits reflects on the large variety of values assumed by the microphysical properties of solid hydrometeors, such as dimension/diameter, density/mass, and fall velocity. These features are usually employed to describe snowflakes and are generally profoundly interlinked. Such bonds are expressed using relationships connecting size properties with mass/density and fall velocity. Mass-size relationship and velocity-size relationship deeply depends on the morphology of the snowflakes and play a key role in the characterization of the snow as well as in the calculation of the ice water content or snowfall rate (Heymsfield et al., 2002) or the simulations of the radar reflectivity factor (Botta et al., 2013).

Although fundamental in solid precipitation research, the parametrization of mass and velocity relationships is a hard task, and several works have proposed microphysical laws (commonly in power-law form) using ground-based observations or aircraft data for mass-size (Locatelli and Hobbs, 1974; Heymsfield et al., 2004; Brandes et al., 2007) or for velocity-size (Locatelli and Hobbs, 1974) relationships. However, it is worth mentioning that the definition of the parameter describing the crystal dimension is not straightforward, and discrepancies can be found in the literature as the choice is often related to the instrumentation used or the methodology followed to derive relationships. For instance, the following density-size relationship is reported in Brandes et al. (2007):

$$\rho(D) = 0.178\, D_0^{-0.92} \tag{5}$$

where density is expressed as a function of the median volume diameter (D_0), meaning that half of the total volume is contributed by particles larger than D_0. This is mathematically defined as:

$$\int_{D_{min}}^{D_0} D^3\, N(D)\, dD = \int_{D_0}^{D_{max}} D^3\, N(D)\, dD \qquad (6)$$

where *N(D)dD* stands for particle size distribution (namely the number of hydrometeors per unit of particle diameter interval and per unit volume) as a function of the "real" diameter (D). Other mass-size relationships (e.g., Muramoto et al., 1995) use the maximum horizontal dimension as a size parameter, or even the diameter of the minimum circumscribed circle that encloses the projected area of the particle is employed in the relationships contained in Heymsfield et al. (2004). These discrepancies warn in making simple relationship comparisons because conversion between different size definitions is not straightforward.

Besides size definitions, density/mass differences exist between single crystals and snowflake aggregates. The latter usually have a lower density than the former containing air within (Keat and Westbrook, 2017). Furthermore, the power-law relationship suggests that smaller particles typically show higher density and that snowflakes may be thought of as particles with decreasing density from the inner to the edges (Ori et al., 2014).

2.1.7 Size distribution of solid precipitation

The size distribution of precipitation is the frequency distribution in diameters of hydrometeors in a given volume, which may be considered characteristic of rainfall or snowfall. Size distribution, also known as drop size distribution (DSD) in case of rain or particle size distribution (PSD) in solid precipitation, is usually expressed in mm^{-1} m^{-3}. It also provides valuable suggestions on processes that occurred in-cloud or during the fall of the particles, in addition to being one of the primary factors involved in determining radar reflectivity.

Most used parametrization for size distribution for rainfall is formulated by Marshall and Palmer (1948), which model DSD in exponential form and based on populations of drops collected on dyed filter paper during precipitation events. A similar parametrization was also used to obtain size distribution for snowflake exploiting ground observations (Gunn and Marshall, 1958):

$$N_s(D) = N_0 \exp(-\Lambda_s D) \tag{7}$$

where $N_s(D)$ is the particle concentration as a function of diameter (here intended as the drop diameter of melted snowflake), N_0 (mm^{-1} m^{-3}), and Λ_s (mm^{-1} m^{-3}) are the intercept and slope parameter respectively. In contrast to the DSD parametrization, the PSD intercept is not fixed but is a function of the rainfall rate (R, in mm h^{-1}):

$$N_0 = 3.8 * 10^3 \, R^{-0.87} \tag{8}$$

that leads to different behaviors of the modeled PSD (see Figure 3) according to rain rate.

While the exponential model seems to work well in the case of aggregate, it fails to replicate PSD in precipitation consisting of single/pristine crystals in which log-normal distribution agrees better (Schlenczek et al., 2017), and even some studies found deviations of the measured size distribution with respect to the exponential model. To overcome this problem and to describe a broader range of PSD, the three-parameter gamma distribution was typically used (Ulbrich, 1983):

$$\mathrm{N(D)} = N_0 \, D^{\mu} \exp\left(-\Lambda D\right) \tag{9}$$

where μ, Λ (mm^{-1}) and N_0 ($mm^{-1-\mu}$ m^{-3}) are the shape, slope, and intercept parameters, respectively. Such distribution has been observed to agree with PSDs collected during winter storms (Heymsfield et al., 2004; Brandes et al., 2007).

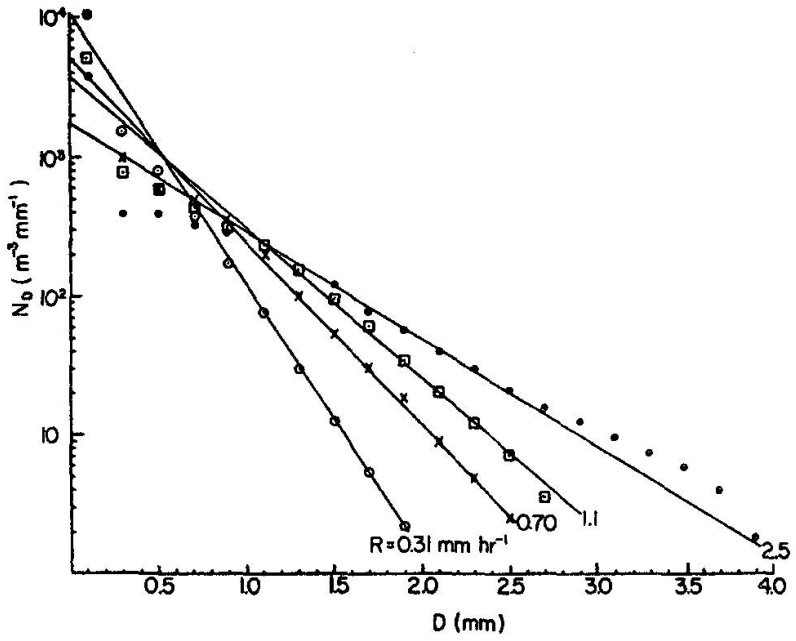

Figure 3 - Averaged distribution of aggregate flakes (markers) against melted diameter and fitted distributions (solid lines) following exponential law. Adapted from: Gunn and Marshall (1958).

2.2 Theoretical Representation of Precipitation Scavenging

During precipitation, a single droplet of diameter D_p, falling through the atmosphere, creates an airflow with streamlines that deviates from the drop surface. As a result, some aerosol particles can end up in the volume swept by the raindrop, collide with the raindrop, and be captured. Therefore, the total rate W_{bc} of the collection of aerosol particles of diameter d_p can be written as:

$$W_{bc}(d_p) = n_M(d_p) dd_p \int_0^{\infty} \frac{\pi}{4} D_p^2 U_t(D_p) E(D_p, d_p) N_D(D_p) dD_p \quad (10)$$

where the $n_M(d_p)$ is the mass size distribution of aerosol, $U_t(D_p)$ the terminal velocity of the raindrop, $N_D(D_p)$ is the drop size distribution, whereas $E(D_p,d_p)$ stands for the collection efficiency (usually equals to the collision efficiency). The integral on the right side of Equation (10) represents the so-called scavenging coefficient λ (in s^{-1}), which typically is a function of location, time, aerosol size distribution, as well as of DSD, and thus it is widely used to evaluate the below-cloud scavenging episode. Through scavenging coefficient, the below-cloud scavenging rate of aerosol particles of diameter d_p can be expressed as:

$$\frac{dC(d_p)}{dt} = -\lambda(d_p) C(d_p) \quad (11)$$

where $C(d_p)$ is the concentration of aerosol particles with diameter d_p, dt is the time interval, and λ is the scavenging coefficient due to precipitation collection (Seinfeld and Pandis, 2008).

Therefore, to calculate the scavenging rate, the knowledge of scavenging coefficients and the size of aerosol and hydrometeors are mandatory. Neglecting the size distribution of precipitation and focusing on scavenging coefficient, this is simply the ratio between the number of drop-particle collisions and the total number of particles in the drop swept area. A value of the collection efficiency (*E)* near 1 indicates that the drop can collect all aerosol particles along its fall. Even if *E* is higher than 1 under given conditions (e.g., charged particles), its value is generally lower than 1. It is worth recalling that collection efficiency strictly depends on the aerosol particle size distribution and that collisions between drop and particle can be promoted by two different mechanisms, namely Brownian diffusion and inertial impaction. The former refers to diffusional migrations of aerosol particles through the air towards the hydrometeors. Since Brownian diffusion decreases as particle size increases, the diffusional collision mechanism is effective only for smaller particles (d_p < 0.2 μm) because the collision coefficient decreases (Figure 4).

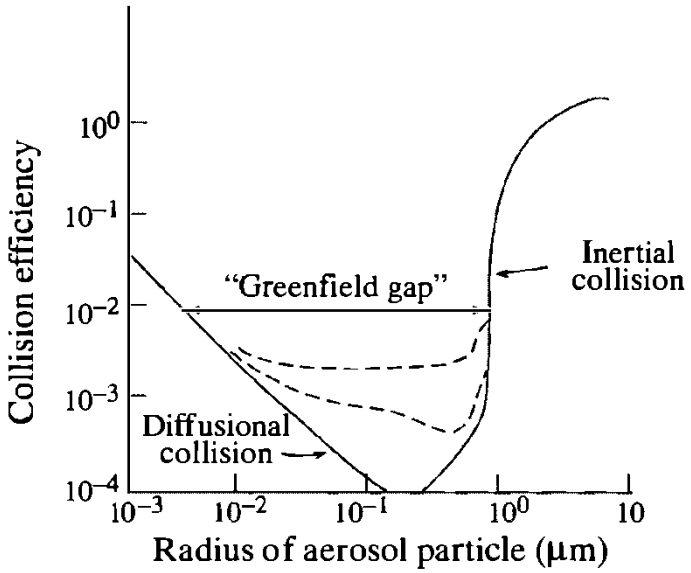

Figure 4 - Collision efficiencies for aerosol particles. Dashed lines represent contributions by phoretic and electrical effects. Source: Hobbs, (2000).

On the other hand, the inertial impacts occur when aerosol particles fail to follow the streamlines around the falling drop because of their size and therefore are collected. This process mainly depends on the aerosol size and is typically more efficient for aerosol larger than 1 μm as diameter (Figure 4). Furthermore, collision efficiency assumes the lowest values for aerosol ranging between 0.2 and 1 μm, in which neither of the two collection mechanisms seems to be effective. This gap is generally referred to as the Greenfield gap for aerosol particles (Figure 4).

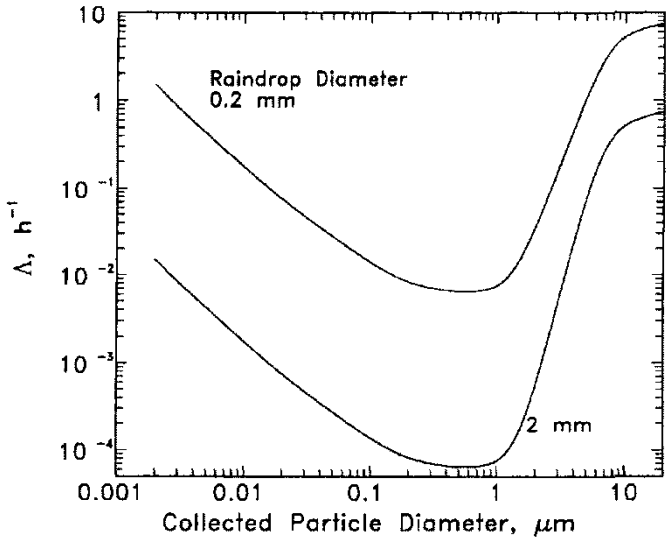

Figure 5 - Scavenging coefficient for aerosol particles as a function of their diameter collected by raindrops of 0.2 and 2 mm diameter. Source: Seinfeld and Pandis (2008).

A practical methodology for highlighting the role of the hydrometeor size in scavenging coefficient is to assume fixed droplet diameter and concentration, which is equivalent to setting the precipitation rate. In this way, λ depends only on the aerosol size and collision efficiency. Using semi-empirical estimates of collision coefficients, the behavior of λ, dependent on collected particle dimensions, is drawn

in Figure 5. This graphic emphasizes the close connection between the scavenging coefficient and both aerosol and drop dimensions. Therefore, simultaneous measurements of aerosol and drop size distributions are needed to obtain valuable estimates of scavenging coefficients. In literature, several studies have dealt with precipitation scavenging and, in particular, with calculating scavenging coefficients for different particle size ranges during precipitation events using aerosol and rain measurements. For this purpose, in most of these works (e.g., Blanco-Alegre et al., 2018; Cugerone et al., 2018a) a slightly modified Equation (11) is adopted to obtain λ using concentrations of the aerosol particles at the beginning (t_0) and the end (t_1) of the rainfall:

$$\lambda(d_p) = \frac{1}{t_1 - t_0} \, ln\left(\frac{C_0(d_p)}{C_1(d_p)}\right) \tag{12}$$

where C_0 and C_1 are the aerosol concentrations at the beginning and the end of precipitation, respectively, whereas t_1-t_0 expresses the event duration is seconds. However, the significance of the hydrometeor size distribution in BCS is still debated in the literature. The action of drop size distribution does not seem to be preeminent as BCS appears to depend on rainfall rate and aerosol dimensions mainly (Andronache, 2003; Luan et al., 2019). On the contrary, the importance of DSD in below cloud scavenging quantification is emphasized several times in Seinfeld and Pandis (2008), and the potential of certain drop diameters in favoring scavenging of specific aerosol sizes was demonstrated in Blanco-Alegre et al. (2018).

The importance and the action of snow in aerosol-removal mechanisms are still controversial. Because of the variety of solid precipitation and its microphysical features, snow scavenging is a more complicated process than rain scavenging. Frozen hydrometeors have different densities and shapes, resulting in different fall velocities and cross-sectional areas, ultimately determining how efficient the falling flakes and crystals are at scavenging suspended aerosol particles (Paramonov et al., 2011). According to Seigneur (2019), rain scavenging tends to be the most crucial process because raindrops can absorb more aerosol particles than snowflake and ice crystals due to the absence of liquid water, which does not promote dissolution. On the other hand, this shortcoming could be counteracted by the more extensive and effective area of snowflakes. Theoretical studies have investigated the variation of the collection efficiency of the hydrometeor with varying aerosol particle diameter (Jung et al., 2015). The collection efficiencies of raindrop and dendrite were compared considering a collector hydrometeor diameter of 0.1 mm. The collection efficiencies due to diffusion of dendrite are resulted lower than those of raindrops (Figure 6). However, the collection efficiencies behavior reverses when larger aerosol particles are considered.

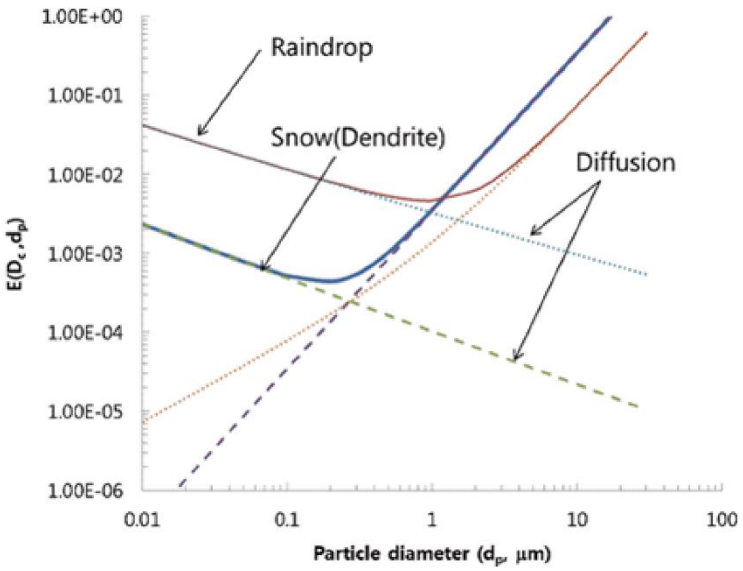

Figure 6 - Collection efficiency as a function of aerosol particle diameter. The hydrometeor collector diameter (D_c) of 0.1mm is used for raindrop and snowflake. Source: Jung et al. (2015).

Finally, it is worth mentioning that precipitation scavenging cannot be considered the unique mechanism which influences aerosol concentration because it can vary due to several other processes. Therefore, as a consequence, Equation (11) should be rewritten as:

$$\frac{dC(d_p)}{dt} = -\lambda(d_p)C(d_p) \pm \left(\frac{dC(d_p)}{dt}\right)_{advection} \pm \pm \left(\frac{dC(d_p)}{dt}\right)_{hygr.\ growth} \pm \left(\frac{dC(d_p)}{dt}\right)_{turb.\ mixing} \pm \pm \left(\frac{dC(d_p)}{dt}\right)_{instr.\ errors} \pm \left(\frac{dC(d_p)}{dt}\right)_{emissions} \quad (13)$$

considering advection, hygroscopic growth, turbulent mixing, instrumental errors, and aerosol emissions. Instrumental errors and turbulence mixing lead to aerosol

variations, which are somewhat challenging to take into account. However, their effects can be omitted compared to those of snow scavenging (Kyrö et al., 2009). Typically, if no other contributions except precipitation removal are present, all the additional terms can be neglected (Laakso et al., 2003).

Chapter 3

3 Data, Methods and Algorithm

3.1 Campaign description

3.1.1 Site

The Italian research station "Mario Zucchelli" (74.7° S, 164.1° E, 10 m a.s.l., Figure 7) has been hosting the ground-based instruments described in this work since December 2016, while the OPC instrument was deployed only for summer season 2020-2021. MZS is located at Terra Nova Bay, a large inlet along the coast of the central part of the Victoria Land, edged by the Transantarctic Mountains Range, at the western margin of the Ross Sea, and the confluence of two glaciers, Reeves and Priestley (Cristofanelli et al., 2011).

The mean annual air temperature is −14.7 °C. The temperature rises up to 5 °C in the summertime and then falls to less than −20 °C in May–August (French and Guglielmin, 2000). Strong winds affect the area due mainly to katabatic effects generated over the Antarctic Plateau by strong radiative cooling. The Priestley and Reeves glaciers are the main paths through which the cold and gravity-driven air flows from the plateau towards the bay (Argentini et al., 1995). Moreover, other flows moving parallel to the Transantarctic Mountains can often set up the so-called barrier winds (Argentini and Mastrantonio, 1994). These flows are also related to large low-pressure systems offshore over the Ross Sea that push air masses towards the steep coast. Such airflows bump into the mountain range and are forced to run parallel to the coastline, hitting MZS.

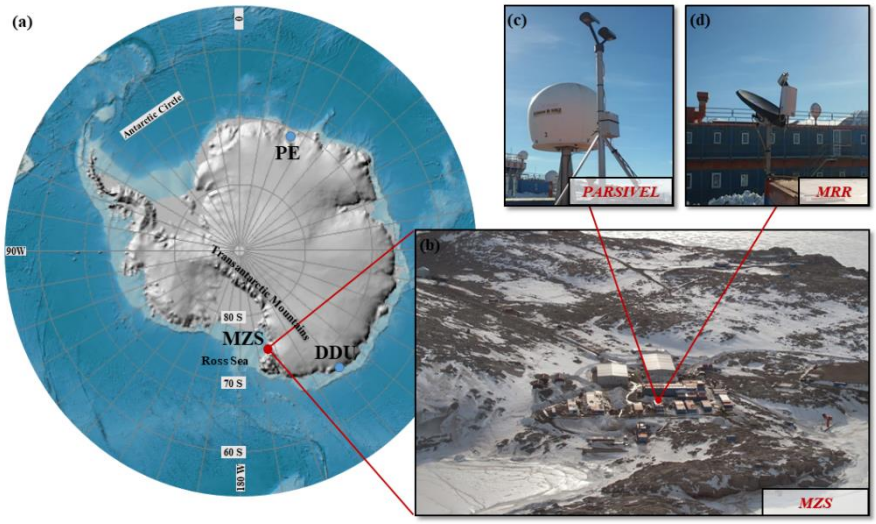

Figure 7 - (a) Geographic map of the Antarctic continent with the locations of Mario Zucchelli (MZS), Dumont D'Urville (DDU), and Princess Elisabeth (PE) research stations (credit: Earthstar Geographics-PGC-UMN-Esri); (b) Aerial view of the Mario Zucchelli research (credit: PNRA.aq) with the position of the co-located instrumentation used in this study, namely disdrometer (c) and radar (d).

3.1.2 Instruments

3.1.2.1 Parsivel Disdrometer

The Particle Size and Velocity (hereafter Parsivel, Figure 7c) deployed at MZS is the optical disdrometer produced by OTT GmbH. This instrument allows for simultaneous measurements of sizes and fall velocities of the hydrometeors (binned in 32 × 32 diameter/speed classes) that cross the horizontal laser matrix of 54 cm^2 produced between the transmitter and receiver heads of the disdrometer (see Löffler-Mang and Joss (2000) for a detailed description of the instrument). Parsivel is easy to handle, robust, and reliable, and such characteristics make it suitable for operating in a harsh environment like Antarctica. Laser disdrometers, historically

used to retrieve the drop size distribution of rain, are now largely employed to study the size distribution of particles in solid precipitation (Löffler-Mang and Blahak, 2001; Yuter et al., 2006; Molthan et al., 2016; Capozzi et al., 2020; Scarchilli et al., 2020), although some intrinsic limitations are known (Battaglia et al., 2010). Moreover, a significant shortcoming is due to the influence of wind on disdrometer measurements (Friedrich et al., 2013a,b; Capozzi et al., 2021), and a large part of the analysis carried out in this Thesis aims to address this issue.

Parsivel data at 1-min time step were used to calculate the PSD using the formula

$$N(D_i) = \sum_{j=1}^{32} \frac{n_{i,j}}{A\ \Delta t\ v_j\ \Delta D_i}, \tag{14}$$

where $n_{i,j}$ is the raw number of hydrometeors at the *i-th* size bin and the *j-th* velocity class detected by the instrument, A the measuring area, Δt the time span, v_j the terminal velocity, and ΔD_i the width of the diameter interval relative to size D_i, while the summation is carried out over all the 32 velocity classes of the disdrometer.

3.1.2.2 Micro Rain Radar

The Micro Rain Radar 2 used in this work (from now on MRR, Figure 7d) is a profiling Doppler radar, typically used in vertical pointing mode that operates at the K-band (24 GHz) to derive Doppler power spectra in 64 bins over 32 vertical range bins (Peters et al., 2002). MRR has a compact design, being composed externally only of a dish with a diameter of ~60 cm, that, coupled with its low power

consumption and robustness, makes it suitable for deployment in remote regions for long-term unattended measurements (Gorodetskaya et al., 2015). Being originally designed only for rain observation, the procedure described by Maahn and Kollias (2012) has been applied to the MRR observations at MZS to obtain reliable radar measurements and increase the sensitivity of the instrument to snowfall. MRR at MZS is located 2 m far from the Parsivel (Figure 7b) and was set with a vertical resolution of 35 m and a temporal resolution of 1 min. This configuration allowed us to obtain the first trustworthy measurement, avoiding clutter contamination, at the third range bin, just 105 m above the ground. The configuration is different from the one most commonly used in Antarctica (Souverijns et al., 2018b) and is more similar to that adopted in the ground validation campaigns of the NASA/JAXA Global Precipitation Measurement (GPM) mission to compare high-resolution vertical profiles of drop size distribution with ground measurements (Adirosi et al., 2020). In this way, such configuration minimizes the distance along the vertical between the two instruments, thus introducing a more meaningful comparison between MRR and ground observations. The MRR measurements collected at the height of 105 m height have been considered in the analysis.

3.1.2.3 TRwS Pluviometer

The Total Rain weighing Sensor (TRwS) manufactured by the MPS system is a weighing gauge used in this work as a valuable reference for snowfall estimations. The instrument is managed by the Italian Antarctic Meteo-Climatological Observatory (IAMCO, https://www.climantartide.it/) and is located a few hundred

meters from the radar and the disdrometer. The instrument has an orifice area of 400 cm^2 and a 1 min sampling period. It is equipped with an Alter-type wind shield and is not heated. An antifreeze agent is added to the collecting bucket to melt the solid precipitation collected progressively. TRwS was evaluated during the WMO Solid Precipitation Intercomparison Experiment (SPICE) (Rha et al., 2014; Earle et al., 2016; Nitu et al., 2019; Kochendorfer et al., 2020) and in Lanza and Vuerich (2009) for rainfall with good performance also in windy conditions. Furthermore, several works have compared TRwS-MPS (even with different collecting areas) with the most common gauges, for example, with a heated tipping bucket (Savina et al., 2012) or with the manually observed values from double fence CSPG (Chinese standard precipitation gauge) (Q. Zheng et al., 2018).

3.1.2.4 OPC-N2

The OPC-N2, manufactured by Alphasense Ltd., is a low-cost optical particle counter that has recently become available for atmospheric monitoring purposes, is characterized by a low price, extreme portability, and slight weight (Sousan et al., 2016; T. Zheng et al., 2018; Sayahi et al., 2019). The OPC-N2 measures particle number concentrations in 16-dimensional bins ranging from 0.38 µm to 17 µm and calculates mass concentration for three particle sizes (PM_1, $PM_{2.5,}$ and PM_{10}) (Sousan et al., 2016). According to Karagulian et al. (2019), OPC-N2 can be classified as OEM (original equipment manufacturers), namely equipment based on low-cost sensors mounted by the customers or already available in a “ready-to-use” format. The Alphasense OPC-N2 sensor was indeed mounted in a waterproof case together with other meteorological and gaseous pollutant sensors not treated in this

Thesis. The whole system (ABBA; Arduino Board Based Air quality monitoring system) was designed, built, and programmed in two units by the author of this Thesis in the context of the Ph.D. programme (Figure 8).

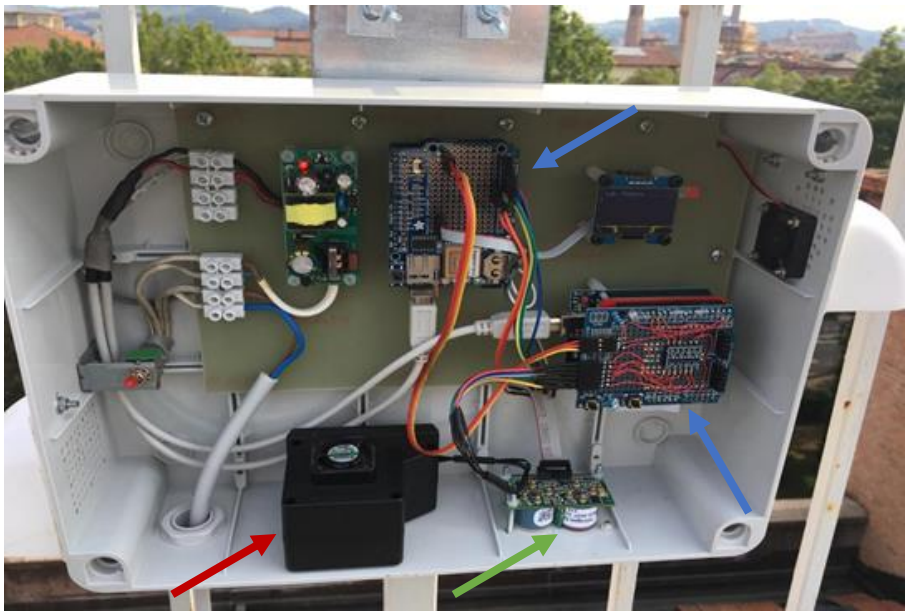

Figure 8 - Internal components of the ABBA monitoring system installed at the rooftop of the Department of Physics and Astronomy of the University of Bologna for the evaluation campaign before being sent and installed at MZS for the Antarctic campaign. Red arrow indicates the OPC-N2, green arrow the electrochemical gas sensors, blue arrows point to the two controlling Arduino boards equipped with meteorological sensors, GPS, and data storage.

OPC-N2 was evaluated in several works in literature (Sousan et al., 2016; Bezantakos et al., 2018; Crilley et al., 2018, 2020; Badura et al., 2018; Masic et al., 2020; Bauerová et al., 2020), pointing out that despite some limitations in the absolute accuracy of the OPC-N2 its low cost and small size offers the ability to assess the temporal-spatial variability of aerosols (Sousan et al., 2016).

However, the discrepancies in performance, arising for different instruments of the same model, suggest the need for testing these systems before any use (Bezantakos et al., 2018). Therefore, the performance of the two built ABBA systems was

evaluated (along with other low-cost sensors) against a calibrated mainstream OPC before the use in the Antarctic campaign (see Section 3.7).

At MZS, the ABBA-1 system containing the OPC-N2 was installed in November 2020 at the rooftop of the *Eliosismo* container (Figure 9), located 300 m far from the Parsivel disdrometer. The positioning was chosen to minimize the influence of research station emission and human activities connected to the MZS on the aerosol measurements performed by the optical counter.

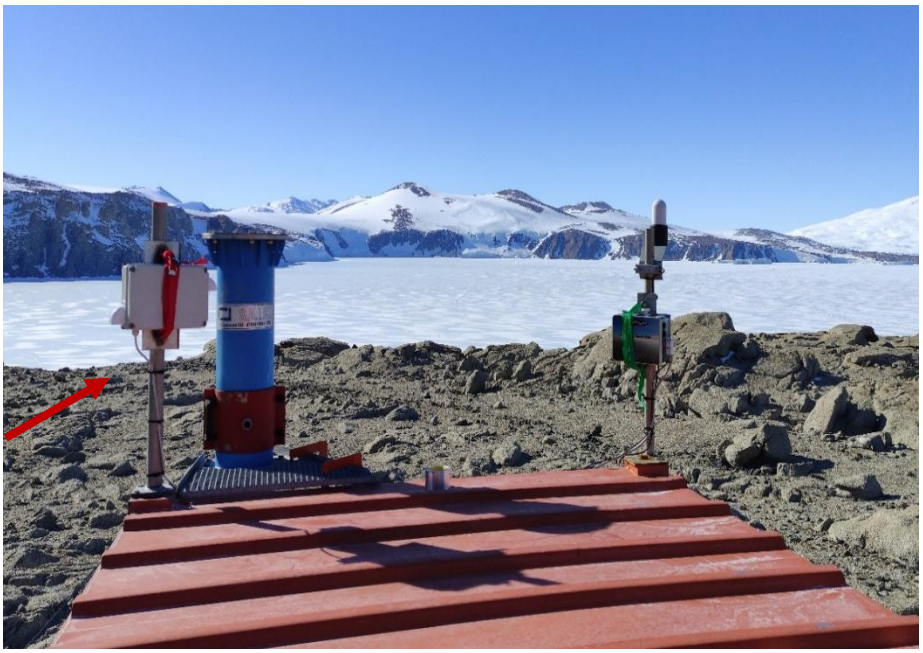

Figure 9 - ABBA system (red arrow) installed at the rooftop of the Eliosismo container at MZS.

3.2 The Kuo Database

The discrete dipole approximation (DDA) is a numerical technique for calculating the scattering and absorption properties of arbitrary-shaped particles (Draine and

Flatau, 1994; Liou and Yang, 2016). The advantages of DDA calculations lie in the possibility of accurately detailing the properties (shape, habit, density) of solid hydrometeors, particularly for aggregate particles (Honeyager et al., 2016). Several DDA databases reporting scattering and absorption properties for different frequencies and particles have been recently developed and made available (Liu, 2008; Botta et al., 2011; Tyynelä et al., 2011; Nowell et al., 2013; Tyynelä and Chandrasekar, 2014; Ori et al., 2014; Leinonen and Szyrmer, 2015; Lu et al., 2016). In this Thesis, the extensive database of single-scattering and microphysical properties of simulated pristine crystals and aggregate particles presented by Kuo et al. (2016) (hereafter referred to as Kuo database) was selected, being the most comprehensive database which also includes the K-band simulations necessary for the MZS setup. This database contains more than 8000 simulated solid no-riming hydrometeors divided into 18 categories, grouped by typology and habit, ranging from 260 μm to 14.26 mm (expressed as maximum dimension of the hydrometeors). Usually, in hydrometeor classification, the choice of classes results from a trade-off between application needs and the actual ability of the classifier to distinguish hydrometeors' signatures. For our purposes, we regrouped categories with similar habits (dendrite and plate) and categories with the same typology (aggregate and pristine), thus obtaining six distinctive categories in terms of radar backscattering cross-sections, namely: aggregate, dendrite aggregate, plate aggregate, pristine, dendrite pristine, and plate pristine. Table 1 shows the categories and the habits contained in the Kuo database and how we mapped them onto the new microphysical categories.

Table 1 - Original hydrometeor categories of the Kuo database (on the left) and how they have been grouped to form the six snow categories used in this work (on the right).

Kuo Database Categories			***Re-Sorted Categories***					
Typology	***Habit***	***Number of Simulated Particles***	***Aggregate***	***Dendrite Aggregate***	***Plate Aggregate***	***Pristine***	***Dendrite Pristine***	***Plate Pristine***
Pristine	*Virtual Snowflake*	*140*				✓		
	Fern Dendrite	*103*				✓	✓	
	Classic Dendrite	*109*				✓	✓	
	Simple Star Dendrite	*148*				✓	✓	
	Thick Classic Dendrite	*122*				✓	✓	
	Needle	*99*				✓		
	Sandwich Plate I	*98*				✓		✓
	Sandwich Plate II	*97*				✓		✓
	Sandwich Plate III	*138*				✓		✓
Aggregate	*Virtual Snowflake*	*286*	✓					
	Fern Dendrite	*459*	✓	✓				
	Classic Dendrite	*425*	✓	✓				
	Simple Star Dendrite	*511*	✓	✓				
	Thick Classic Dendrite	*1028*	✓	✓				
	Needle	*1101*	✓					
	Sandwich Plate I	*1055*	✓		✓			
	Sandwich Plate II	*1049*	✓		✓			
	Sandwich Plate III	*1000*	✓		✓			

In detail, the category of aggregate includes all the nine specific habits of the aggregate typology present in the Kuo database, while the dendrite aggregate category includes the habits Fern Dendrite, Classic Dendrite, Simple Star Dendrite, and Thick Classic Dendrite. The new category of plate aggregate includes the three

habits named Sandwich Plate in the Kuo database. Similar choices were made for the new categories of pristine, dendrite pristine, and plate pristine (see Table 1). Thereby we obtained six distinguishing snow categories to consider the natural variability of snow particles better.

A single backscattering value matching each of the 32 Parsivel size bins was obtained as follows. For each category, assuming the maximum size of a nonspherical hydrometeor (hereinafter referred to as D) as the representative size of the hydrometeor:

1) backscattering cross-section was calculated for all the entries in Table 1 (second column);
2) the particles were distributed into the 32 size bins based on D of each particle;
3) a single backscattering value representative of each size bin was calculated by averaging all the backscattering cross-section values in that size bin, thereby achieving 32 backscattering cross-section values, one value for each Parsivel size bin.

Finally, in addition to the backscattering values, we obtained a mass-D relationship for each category by fitting density and diameter values from the Kuo database with a power-law model.

It is worth underlining that the definition of solid particle dimension in Kuo database can differ from that detected by the Parsivel disdrometer and that such discrepancy could also impact the methodology devised and used in this thesis. Indeed, in characterizing the dimension of solid hydrometeors, Parsivel retrieves only one size parameter, which is approximately equal to the widest horizontal

dimension (Battaglia et al., 2010). Therefore, to minimize the possible discrepancy in size definition and be consistent with Parsivel observations, the maximum dimension value for each particle entry of Kuo database was used. In addition, considering Parsivel detection capability (i.e., one dimension parameter), the discrepancies are expected to be significant in the case of asymmetric shapes whose orientation can be changed during fall due to turbulence or convection affecting the methodology used and leading to a worsening of MRR and Parsivel consistency in terms of radar reflectivity. However, the more significant part of habits used in this thesis has symmetric shapes (i.e., dendrites, plates), resulting in a negligible impact of size definition in the methodology.

3.3 *Ze-SR* Relationships and Method for Hydrometeor Classification

This section describes a methodology aiming to improve QPE by applying different *Ze-SR* relationships based on distinctive microphysical features of the snow categories. At first, six *Ze-SR* relationships (one for each snow category) were derived using the disdrometer measurements at the ground in terms of disdrometer-derived equivalent radar reflectivity (Ze_{disd}) and snowfall rates *SR*s. For each category, Ze_{disd} is expressed as:

$$Ze_{disd} = 10^{18} \frac{\lambda^4}{\pi^5 |K|^2} \int_{D_{min}}^{D_{max}} \sigma(D)\, N(D)\, dD \qquad (15)$$

where λ (in m) is the wavelength of the MRR, $|K|^2$ is related to the dielectric constant of liquid water and conventionally equals 0.92, $\sigma(D)$ (in m^2) are the backscattering cross-sections as deduced from the Kuo database, while $N(D)$, D_{min} and D_{max} are the PSD (m^{-3} mm^{-1}), the minimum and the maximum particle size from the disdrometer.

SRs (in mm liquid water equivalent) are estimated starting from PSD data obtained from the disdrometer and applying proper velocity-diameter and mass-diameter relationships as follows:

$$SR = \frac{3.6}{\rho_w} \int_{D_{min}}^{D_{max}} N(D)\, v(D)\, m(D)\, dD \qquad (16)$$

where ρ_w represents the density of liquid water (in g cm^{-3}), $N(D)$ the PSD (m^{-3} mm^{-1}), and $v(D)$ (m s^{-1}) and $m(D)$ (in g) the velocity and mass of the falling particles, respectively, while D_{min} and D_{max} denote the minimum and maximum size detectable by the disdrometer. For velocity, we used the well-established relationships proposed by Locatelli and Hobbs (1974), while masses are derived, for the new six categories, from the Kuo database as described at the end of the previous section.

Having adopted a power-law form of the relationships linking equivalent radar reflectivity with snow rate, their prefactors and exponents have been derived using a Nonlinear Least-Squares fitting technique.

For QPE calculation, the selected relationship was inverted to obtain the snowfall rate from an observed value of MRR reflectivity. Hence, the choice of the best

relationship to use becomes crucial, as it is deeply connected to the microphysics of snow.

The selection was made as follows:

1. The root mean square errors (RMSE) between the equivalent reflectivity factor at the 105 m height measured by the MRR (from now on Ze_{MRR}) and each of the six values of Ze_{disd}, one for each snow category, were calculated in a 10-min mobile time window. The category with the lowest RMSE value is considered to be representative of the prevailing type of particles in that time window, making it possible to classify the falling hydrometeors;
2. According to the snow category thus determined, the proper *Ze-SR* relationship is applied in that time window to estimate snow precipitation on the ground.

Three main aspects deserve attention. First, since the microphysical properties of snowfall can change in a time scale of a few minutes (von Lerber et al., 2017), the choice of 10 min as the time window for hydrometeor classification is a trade-off between having a sufficient number of measurements to apply our methodology and being short enough to catch the microphysics variations.

Second, the MRR equivalent reflectivity factor at the lowest useful range gate is considered the reference reflectivity value in our analysis. MRR reflectivity measurements are, in principle, negligibly affected by the airflow around the instrument and horizontal wind (Capozzi et al., 2020), unlike other ground-based sensors as disdrometers (Testik and Rahman, 2016), whose observations are prone to artifacts or misleading measurements in case of strong wind, as mentioned above.

Third, comparing simultaneous observations of Ze_{MRR} and the disdrometer-derived Ze_{disd} is the basis of the proposed methodology for hydrometeors classification. Doubts may arise due to the different areas captured by the instruments, as MRR measurements are obtained in sample volumes larger than that of disdrometer measurements and by comparing measurements at the surface with measurements aloft. However, the synergic use of this set of instruments for retrieving precipitation amounts or properties has long been well established, also with scanning radars and both in snow and rain precipitation. Furthermore, adopting a high vertical resolution has minimized the vertical distance between the MRR and the disdrometer, giving strength to the assumption that the differences between Ze_{MRR} and the various Ze_{disd} can primarily be ascribed to the snow type.

3.4 Sublimation Ratio

Low-level sublimation of precipitation typically refers to those hydrometeors that do not reach the ground during snowfall (the so-called *virga*) or to a robust decrease of snowfall intensity close to the surface. This process mainly depends on the microphysical features of the ice particles such as density, velocity, and PSD and the atmospheric conditions, primarily temperature and humidity. Several observations suggest that sublimation of precipitation has a significant role in snowfall processes over Antarctica (Grazioli et al., 2017b; Souverijns et al., 2018b; Durán-Alarcón et al., 2019), especially along the coast and the escarpment region where the interaction with the dry katabatic wind leads to a sublimation enhancement. The sublimation process also affects the comparison between

satellite-based observations and ground-based measurements of snowfall, and it is of considerable significance because, in a warming climate, it may counterbalance the expected increase of precipitation in Antarctica (Grazioli et al., 2017b).

In this work, the MRR profiles were used to assess the sublimation of precipitation in the lower atmospheric levels at the MZS during snowfall events. Quantification of the sublimation was obtained in terms of the Sublimation Ratio (from now on *SubR*), modifying the original definition by Grazioli et al. (2017b), as:

$$SubR = \frac{SR_i - SR_{105}}{SR_{105}} \tag{17}$$

where SR_i is the snowfall rate (1-min time resolution), at the *i-th* MRR range gate, calculated through the proper *Ze-SR* relationship based on snow classification using the MRR reflectivity profiles; SR_{105} is the snowfall rate at the first trustworthy range gate (i.e., 105 m above the ground). Positive values of *SubR* indicate that the sublimation process is taking place.

3.5 Precipitation dataset used for QPE

Both the MRR and Parsivel used for this study have been operational since 2016 at MZS. However, only observations in two summers, from November to March 2018–2019 and 2019–2020, were considered, being other periods discarded due to insufficient time synchronization and other technical issues (i.e., failure/maintenance of the instrumentation or unexpected power outage). We

selected only days with at least 60 min of continuous precipitation, resulting in 52 days with precipitation, of which 32 were in 2018–2019, and 20 in 2019–2020.

Furthermore, the following criteria were adopted in processing 1-min data:

a) minutes with Ze_{MRR} value lower than -5dBZ were discarded from the analysis since, below that threshold, MRR data could be incomplete (Souverijns et al., 2017; Maahn and Kollias, 2012);
b) minutes in which Parsivel detected less than 10 particles or the *SR* calculated for aggregate category is less than 0.01 mm h^{-1} were eliminated (Scarchilli et al., 2020; Maahn and Kollias, 2012);
c) only minutes with simultaneous valid measurements of MRR and Parsivel satisfying criteria a) and b) were included.

A total of 23566 min of solid precipitation at MZS completely fulfil these criteria, corresponding to more than 392 h of snowfall data. At this stage, no control has been placed on data quality regarding wind speed at the ground, unlike other studies (Souverijns et al., 2017; Scarchilli et al., 2020), but this critical issue will be tackled in the following subparagraph.

3.5.1 Wind effect on disdrometer data

The retrieval of hydrometeor size and velocity by optical disdrometers is affected by intrinsic limitations of their measuring principle that post-processing can mitigate (Nešpor et al., 2000), as it is done for other uncertainties (Löffler-Mang and Blahak, 2001; Yuter et al., 2006; Battaglia et al., 2010). Friedrich et al. (2013a) deeply investigated the effects of wind on Parsivel measurements in rain. Observing

artifacts (such as a large number of particles with large diameters but low speeds) when the wind speed is greater than 10 m s^{-1}, they related this effect to the slanted trajectories of the particles caused by the air motions. In snowfall, Capozzi et al. (2020) showed disdrometer spectrographs with an unusually high number of small, high-speed hydrometeors in the presence of wind. Obviously, the incorrect size and fall velocity estimations affect hydrometeor classification and derivation of quantities as *PSD* or *SR*.

Therefore, robust preprocessing techniques are mandatory to mitigate this issue in disdrometer data collected in snowfall, especially in Antarctica, where strong wind is often present. In the works of Molthan et al. (2016) and Capozzi et al. (2020), an upper limit threshold of 5 m s^{-1} was set to ensure reliable disdrometer data; Scarchilli et al. (2020) rejected data with wind over 7 m s^{-1} as a whole and also particles with a measured velocity higher than a theoretical maximum limit; Souverijns et al. (2017) estimated a maximum wind speed based on instrumental limits of PIP that must not be exceeded to preserve measurement quality. However, imposing an upper wind speed threshold, as in Molthan et al. (2016), using concurrent meteorological data from an automatic weather station equipped with a cup anemometer located 300 m from MZS (managed by IAMCO), would have significantly reduced our database (28 days instead of 52 with 5 m s^{-1} daily wind threshold) as precipitation events at MZS are often accompanied by a strong wind. Hence, we propose a different approach that is capable of retaining more events while preserving the reliability of the measurements.

Capozzi et al. (2020) noted that visual inspections of disdrometer spectrographs reveal different apparent regimes related to wind speed. The expected spectrogram

for snow (particles with low terminal velocity over a wide range of diameters) could be recognizable only for low wind speed (Löffler-Mang and Blahak, 2001), whereas significant changes, such as an unusual number of particles with small size and high speed, appear in the presence of stronger winds.

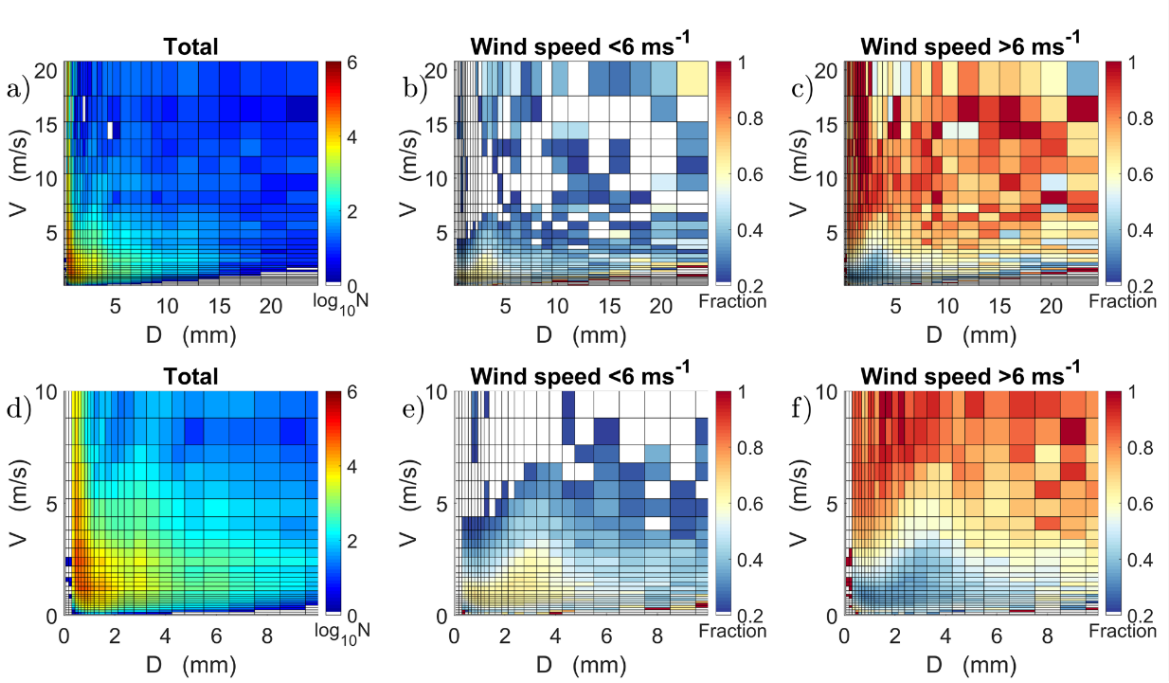

Figure 10 - a) Disdrometer data of the 2019 and 2020 summer seasons at MZS. In Parsivel spectrograph (fall velocity vs. diameter), colors represent the number of particles for each bin. Number of hydrometeors below b) and above c) the wind speed threshold (6 m s^{-1}) divided by the total number of hydrometeors detected in each bin (colors represent fraction values). d), e) and f) as in a), b) and c) but zoomed up to 10 mm and 10 m s^{-1} for diameter and velocity values, respectively.

Figure 10 illustrates these different regimes that appear in MZS disdrometer measurements: Figure 10 a) b) and c) report the whole range of diameters and velocities; Figure 10 d) e) and f) highlight diameters up to 10 mm and velocities up to 10 m s^{-1}. Figure 10a shows the spectrograph of 1-min data of the 2019–2020 summer season. The two regimes appear clearly by plotting the fraction of particles for each disdrometer bin collected with wind speed lower (Figure 10b) and higher

(Figure 10c) than the threshold of 6 m s^{-1}, i.e., the count of particles below/above wind threshold divided by the total number of particles for each bin. In Figure 10b, values greater than 0.6 (i.e., the vast majority of the total number of particles in the considered period) lie in the bins where snow is expected, indicating that Parsivel correctly detected solid hydrometeors at low wind conditions. In contrast, when the wind exceeds that threshold, the higher fractions of minutes are located in unexpected bins for solid precipitation (Figure 10c), indicating the shortcoming of disdrometer snow measurements in windy conditions.

It is worth underlining that a 6 m s^{-1} wind threshold was selected after considering 5 and 7 m s^{-1} also (Figure 11 and Figure 12), resulting in the best trade-off in terms of particle numbers below and above the threshold and also showing a clear distinction between the two different regimes. Likewise, the 6 m s^{-1} value was chosen after a sensitivity analysis to assess its robustness. Indeed, using a threshold of 5 m s^{-1}, as can be clearly seen in Figure 11, would be too penalizing because most of the particles would have been excluded. On the other hand, 7 m s^{-1} appeared not to be the right choice as a significant part of retained particles would be located in unexpected bins for solid precipitation (Figure 12).

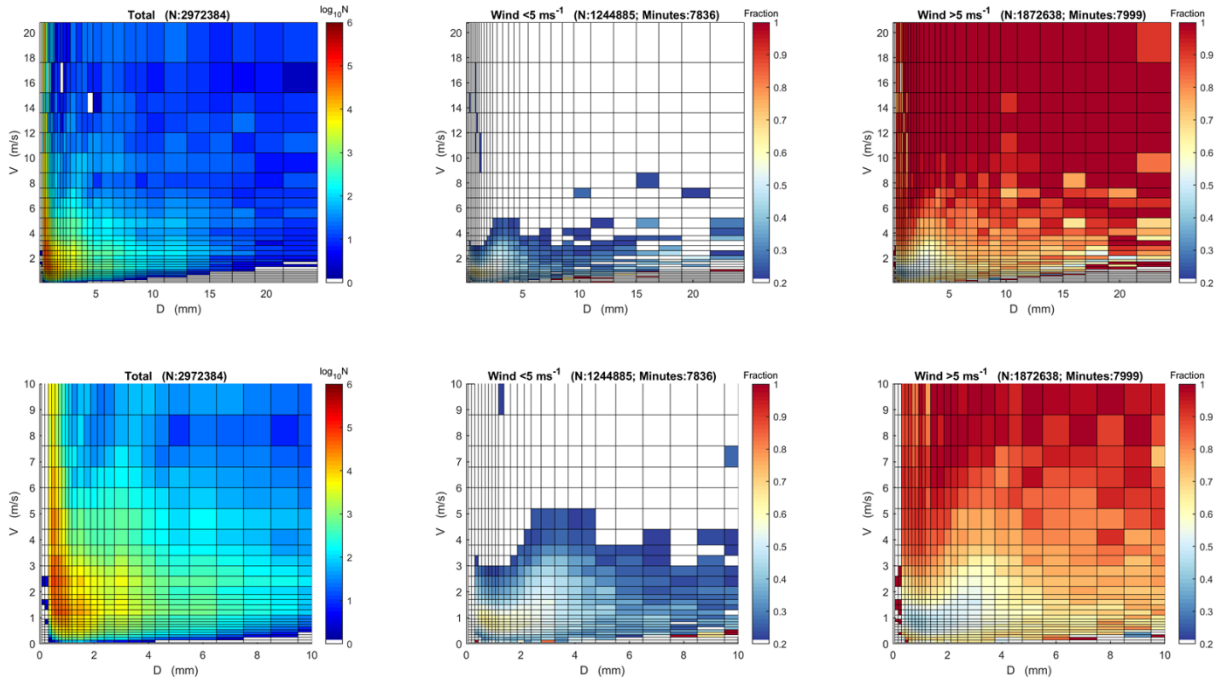

Figure 11 - Same as Figure 10 but for 5 m s^{-1} wind threshold.

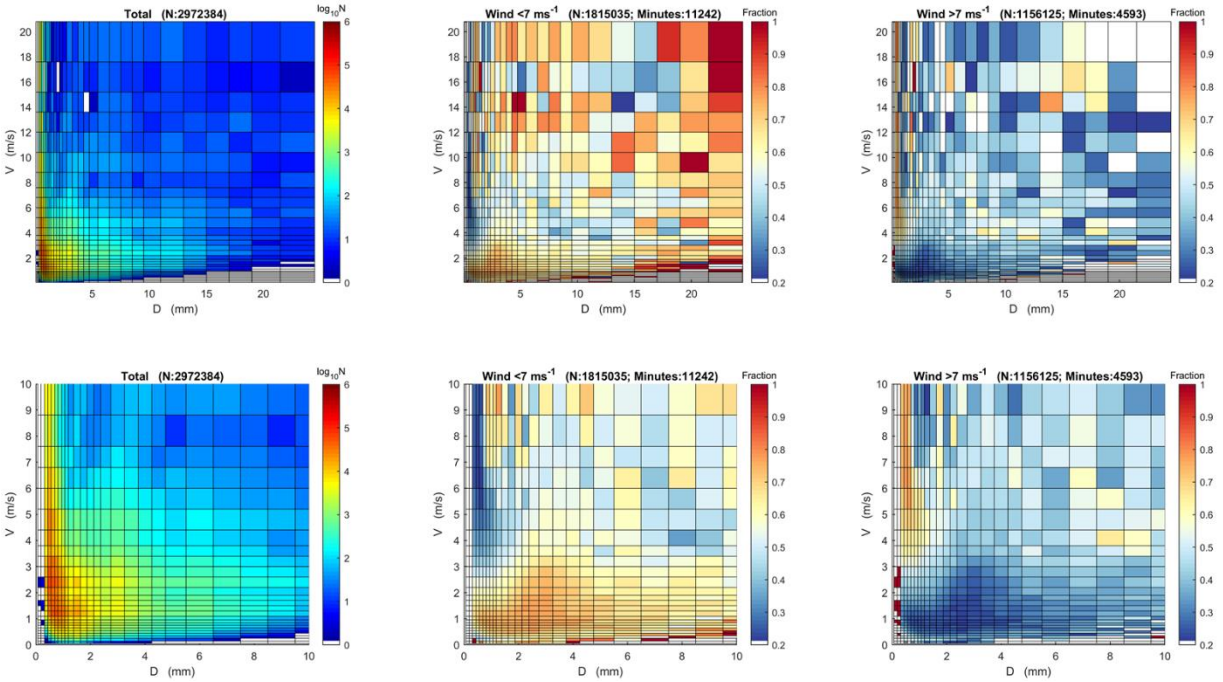

Figure 12 - Same as Figure 10 but for 7 m s^{-1} wind threshold.

This analysis provided information on bin reliability in the case of snow and wind from which to derive how to weigh up the particle numbers detected by the disdrometer in each bin. Consequently, we assigned a weight *w* to each disdrometer

bin: bins with values at least 0.6 in the fraction plots with wind lower than 6 m s^{-1} (Figure 10b,e) were considered as reliable and associated with a weight equal to 1; bins below 0.6 were considered less reliable in windy conditions and associated with a weight ranging between 0 and 0.8, in 0.1-steps.

We generated 104 masks in order to select the best one accounting for wind issues. The procedure followed was:

a) a new weight mask was generated by assigning $w = 1$ to reliable bins and a random weight to less-reliable bins;
b) the weight mask was then applied to the 23566 min of disdrometer raw data, and new PSDs were calculated;
c) new Ze_{disd} were derived for the six snow categories;
d) RMSE between the radar Ze_{MRR} and each of the six values of Ze_{disd} for all PSDs was computed;
e) the mean of the RMSEs values was computed.

The weight mask with the lowest mean value of RMSEs was chosen (Figure 13b) and applied to the entire disdrometer dataset to obtain the spectrogram in Figure 13c. The number of smaller and faster particles was sensibly lowered by means of the weight mask, as well as the particle counts in bins not usually occupied by solid hydrometers. In addition, it is worth noting that the number of particles lying in the reliable bins remained practically unchanged.

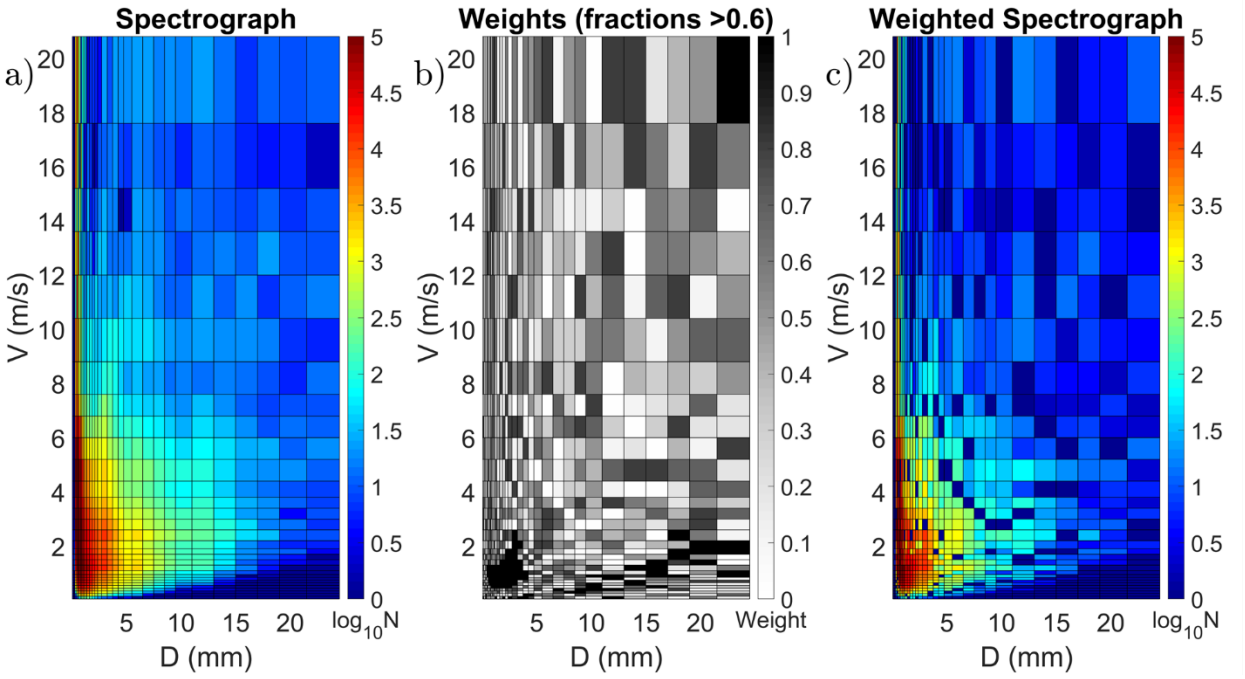

Figure 13 - Application of the weighting method described in the text: a) Original particle spectrograph; b) Selected weight mask for each disdrometer bin; c) Resulting weighted disdrometer spectrograph.

Disdrometer filtered data were then used to derive the PSD, Ze_{disd}, the *Ze-SR* relationships for the different snow categories, and, finally, the hydrometeor classification procedure.

Finally, it is worth remarking that the correction of disdrometer data does not exclude the possibility that some particles detected by the disdrometer during precipitation events may be related to blowing snow. Different from other Antarctic sites, MZS is scarcely affected by blowing snow during katabatic events, despite being on the coast, thanks to a favorable orography (Scarchilli et al., 2020). Indeed, snow particles raised by strong wind over the plateau undergo sublimation before reaching the site (Scarchilli et al., 2010). Nevertheless, being aware of the impact of blowing snow on precipitation estimates, and therefore, to mitigate the influence of blowing snow, the instrumentation was installed at the height of approximately

7 m above the ground, minimizing the interaction of the collection of precipitation with the blowing snow near the surface (Seefeldt et al., 2021). Lastly, a careful visual inspection of MRR data during precipitation events has ruled out the presence of the shallow MRR vertical profiles that would have suggested the presence of blowing snow.

3.6 Scavenging Coefficients

Particle count measurements performed by the OPC-N2 at 1-min time resolution were used to assess the scavenging processes at MZS along with Parsivel observations, useful for retrieving the timing and duration of the snowfall events. The scavenging coefficients were calculated using Equation (12). Bearing in mind that up to 90% of the PM_{10} mass in the MZS region comes from aerosol particles of a size smaller than 1.0 µm (Illuminati et al., 2016, 2020; Vagnoni et al., 2021), only counts of the first five size bins of the N2-OPC (i.e., particles from 0.38 to 1.6 µm) were considered in this analysis. In addition to the scavenging coefficient, the scavenging ratio (ΔC) was also calculated to evaluate scavenging processes regardless of snowfall duration. The scavenging ratio was defined (Luan et al., 2019) as:

$$\Delta C(d_p) = \frac{C_1(d_p) - C_0(d_p)}{C_0(d_p)} \times 100\% \quad (18)$$

where ΔC (%) is the concentration scavenging ratio, C_1 (counts min^{-1}) is the concentration after the snowfall, and C_0 (counts min^{-1}) is the concentration before

the snowfall for a given size (namely for the bin diameter). The negative ΔC values indicate a decrease of aerosol concentration during the snowfall, whereas the positive ΔC indicates an aerosol increase.

It is worth underlining that the aerosol concentration and snowfall timing considered for scavenging investigation were defined as follows:

a) snowfall event is identified as the consecutive precipitation hours. Adapting definitions by Chen et al. (2013) and Luan et al. (2019), if the precipitation-free period is equal to or longer than four hours, the snowfall is considered as two precipitation events;
b) minute in which Parsivel detected more (less) than 10 particles is considered the beginning (ending) of the snowfall event;
c) to limit the impact of the short-term aerosol fluctuation, minimize instrumental weakness, and increase the robustness of the methodology, values of C_0 and C_1 in scavenging coefficient and ratio calculations are the 6-hours averaged values of the OPC concentration measurements (in terms of counts min^{-1}) before and after the precipitation event, respectively.

3.7 Evaluation of OPC-N2 performance

As discussed earlier, performances of the OPC-N2 were evaluated through a comparative study before being installed at the MZS, along with a set of different low-cost and research-oriented laser particle counters in outdoor ambient conditions. Two distinct experimental field campaigns have been carried out for this purpose during the periods June 6th, 2019–August 4th, 2019 and September

23rd, 2019–February 12th, 2020 in Bologna (44°30′ N, 11°21′ E; Northern Italy), located in the Po Valley, a region representing one of the significant pollution hotspots in Europe (e.g., Tositti et al., 2014; Diémoz et al., 2019). The study periods included a range of different meteorological conditions, well representative of the typical weather conditions affecting the city and the surrounding region in the warm and cold seasons. To investigate and compare the performances of the sensors in measuring particle size distributions and particle mass concentrations, they were co-located on the rooftop of the Department of Physics and Astronomy of the University of Bologna. The optical sensors included, in addition to a couple of OPC-N2 low-cost sensors, one Profiler Model 212 (MetOne Instruments), a couple of iSCAPE Citizen Kits (SCK) low-cost sensors, and one LOAC (light optical aerosol counter; MeteoModem). Table 2 summarizes the main technical specifications of the OPC sensors used in this comparative campaign.

Table 2 - Technical specifications of the MetOne Profiler-212, OPC-N2 by Alphasense, Smart Citizen Kit (SCK), and LOAC (Light Optical Aerosol Counter) optical particle counters.

	Instrument			
Specification	***MetOne***	***OPC-N2***	***SCK***	***LOAC***
Size (cm)	*114.3 × 190.5*	*7.5 × 6 × 6.4*	*6 × 6 × 2*	*20 × 10 × 5*
Weight (g)	*1200*	*<105*	*65*	*300*
Size range (µm)	*0.3-10*	*0.38-16*	*0.3-10*	*0.2-50*
Size bins	*8 (selectable)*	*16*	*3*	*19*
Flow rate (L min^{-1})	*1*	*1.2*	*0.1*	*2*

Measurement frequency (s)	*1-60*	*1-5*	*30*	*1-60*
Laser wavelength (nm)	*808*	*658*	*680*	*650*
Scattering angle (°)	*90*	*30*	*90*	*12 and 60*

All the sensors utilized in this analysis were optical particle monitors that use laser beams to detect and count particles, thereby evaluating the scattering signal from suspended particulate to provide a semi-continuous real-time measurement of airborne particulate as a function of size. In particular, the MetOne Profiler 212 is a robust mainstream optical particle counter widely employed in air monitoring (e.g., Pal et al., 2014; Mamali et al., 2018), regularly re-calibrated on an annual basis. This instrument is equipped with a humidity sensor and an inlet heater to prevent moisture from being sampled as particulate mass and therefore was employed in the analysis as a reference instrument.

The measurement time resolution of the MetOne Profiler 212 (hereafter MetOne), OPC-N2, and LOAC sensors was set to 60 s. Instead, the SCKs made measurements integrated over 30 s, which were averaged to the same time resolution of the other sensors for homogeneity.

Observations of meteorological variables (atmospheric pressure, air temperature, air relative humidity, wind speed, and wind direction) were collected by a Davis Vantage Pro2 (Davis Instruments) on a 10-min time basis.

3.7.1 Number Concentration to Mass Conversion

Optical particle counters are typically based on light scattering by aerosol particles in a flow cell (e.g., Jaenicke, 1972; Liu et al. 1974; Welker, 2012). As a result, this broad family of instruments is designed to assess particle number densities as a function of particle size bins based on suitable scattering parameterization. Therefore, particle number density is a fundamental metric to integrate aerosol gravimetry-based metrics efficiently. The MetOne, used as a reference, provides the number densities in previously detailed particle size intervals. In order to make all the data comparable, signals from the MetOne were converted into mass concentration (μg m^{-3}).

Conversely, the OPC-N2 and the SCK sensors estimate PM_1, $PM_{2.5,}$ and PM_{10} mass concentrations from count measurements using embedded proprietary algorithms not disclosed to the public. Similarly, the LOAC sensor estimates $PM_{2.5}$ and PM_{10} mass concentrations from count measurements. In general, the algorithms used by the optical sensors assume a default particle density (1650 kg m^{-3} in the case of OPC-N2; unknown for the SCKs); a volume-weighting factor (default set to 1) to account for errors in sizing due to differences in the refractive index of particles used for calibration and those being measured (Renard et al., 2010); and for SCK, an atmospheric correction factor used in field evaluation whose details are not available from the manufacturer.

Therefore, the number density data obtained by the MetOne was subjected to a suitable inversion procedure for the planned comparison with the other devices. The following computation was used based on the assumptions of spherical particles

with uniform density, a standard approximation, though not complying with real ambient aerosol particles (Crilley et al., 2018).

For each size bin of the instrument, a weighted volume diameter was computed according to (Crilley et al., 2018):

$$D = LB\left[\frac{1}{4}\left(1+\left(\frac{UB}{LB}\right)^{2}\right)\left(1+\frac{UB}{LB}\right)\right]^{\frac{1}{3}} \quad (19)$$

where *LB* and *UB* are respectively the lower and upper boundaries of each size bin. The particle volume (V_p) and mass are then calculated as follows:

$$V_p = \frac{\pi D^3 n}{6} \quad (20)$$

$$m = \rho\, V_p \quad (21)$$

where n is the particle count, and ρ is the particle density (in g cm^{-3}). According to Tittarelli et al. (2008) and Di Antonio et al. (2018), the value of particle density was assumed equal to 1.65 g cm^{-3}, a widely accepted approximation well representative of urban average particle mixture (Crilley et al., 2018; Di Antonio et al., 2018). The particle mass is eventually divided by the sampled air volume to provide aerosol mass concentration per unit air volume. Note that in the case of the LOAC instrument, m is not the particle mass, but it is already the volume mass concentration. Particle mass concentrations for the MetOne (PM_1, $PM_{2.5}$, and PM_{10})

and the LOAC (PM_1) were finally estimated by summing the concentration masses in the various size bins fitting to the respective aerosol cutoff.

3.7.2 Performance Metrics of the OPC Sensors

In order to detect and remove outliers from the 1-min time-series recorded by all the sensors, the Hampel filter based on the calculation of the median and the standard deviation expressed as median absolute deviation (MAD) over a sliding window was used (Hampel, 1974; Liu et al., 2004). The filter identifies as outliers those values differing from the window median by more than *x* standard deviations and substitutes them with the median. The filter has two configurable parameters: the size of the sliding window and the number of standard deviations that identify the outlier (*x*). In this case, a sliding window of 7 observations (given observation and the 2 × 7 surrounding elements) and a value of 2 × MAD to detect outliers were selected.

In particular, besides visual comparisons of the time series, scatterplots, and histograms, a set of merit factors was calculated. Indexes include widely used metrics, such as the mean bias error (MBE), the mean absolute error (MAE), the root mean square error (RMSE), the correlation coefficient (CC), the coefficient of determination (R^2), and the t-score (t). In addition, normalized values were also calculated for MBE, MAE, and RMSE, using the observation range (NMBE, NMAE and NRMSE) or the observation average (CVMBE, CVMAE, and CVRMSE) (details on the formulas used are contained in Brattich et al. (2020) - Appendix A).

The approach, using a combination of qualitative and quantitative analyses including statistical parameters such as the bias, the RMSE, and the MAE, besides the correlation coefficient, is robust and complete for characterizing the performances of the OPC sensors completely (Karagulian et al., 2019).

3.8 Precipitation dataset for BCS at MZS

After the comparison analysis, one of the two OPC-N2 tested (labeled as ABBA-1) was installed at the MZS in the framework of the XXXVI Italian Antarctic expedition. Aerosol measurements started on November 28th, 2020, and ended on January 7th, 2021. During this time, following the aforementioned criteria, two snowfall episodes were identified by Parsivel with a total of more than 50 hours of precipitation.

Chapter 4

4 Results and discussion

4.1 Consistency between MRR and Parsivel measurements

Comparison of the equivalent reflectivity measured by the MRR and the equivalent reflectivity calculated from the disdrometer and Kuo database for each snow category is the first step to evaluate the performance of the proposed method. In Figure 14 and Figure 15, the 23566 min of simultaneous Ze_{MRR} and Ze_{disd} are compared by means of qualitative density scatter plots and quantitative merit factors. The latter are the Root Mean Square Error (RSME, in dBZ), the Mean Difference (MD, in dBZ), and their values normalized with respect to the reference measurements, i.e., Ze_{MRR}, namely the Normalized Standard Error (NSE, in %), and the Normalized Bias (NB, in %), respectively, the Slope (Sl), the Pearson correlation coefficient (CC) (see Gorgucci and Baldini (2015) for a detailed description). Each figure reports the comparison both without wind correction for disdrometric data (left panel) and after applying the wind mask (right panel) discussed in the previous section.

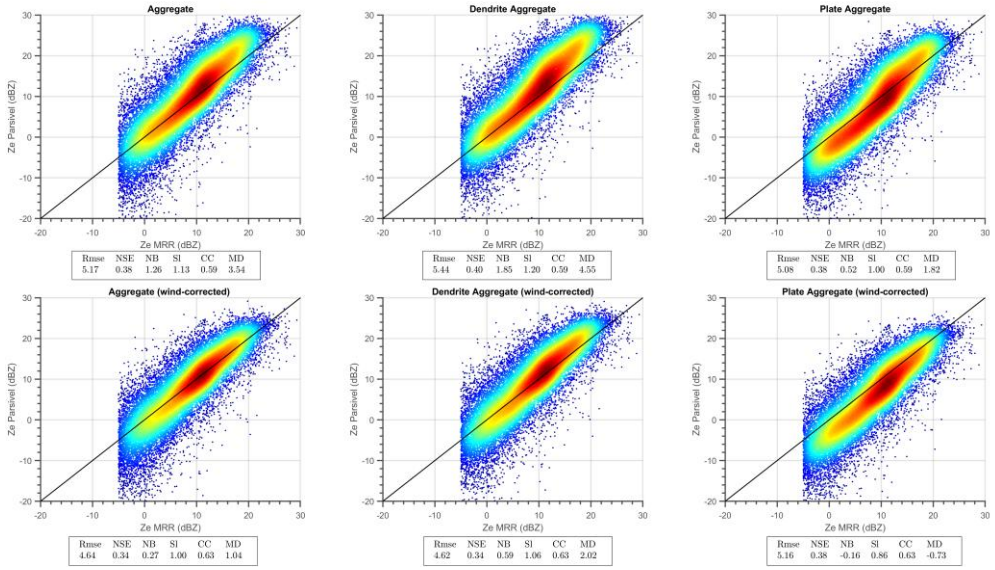

Figure 14 - Density scatter plots for 1-min MRR and disdrometer data in terms of equivalent radar reflectivity for aggregate-like categories. Disdrometer observations are not corrected (upper row) and corrected (lower row) for wind influence. Points are colored based on data density ranging from dark red (high density) to dark blue (low density), whereas the black line represents the bisecting line. Merit factors of the comparisons are also reported next to each plot.

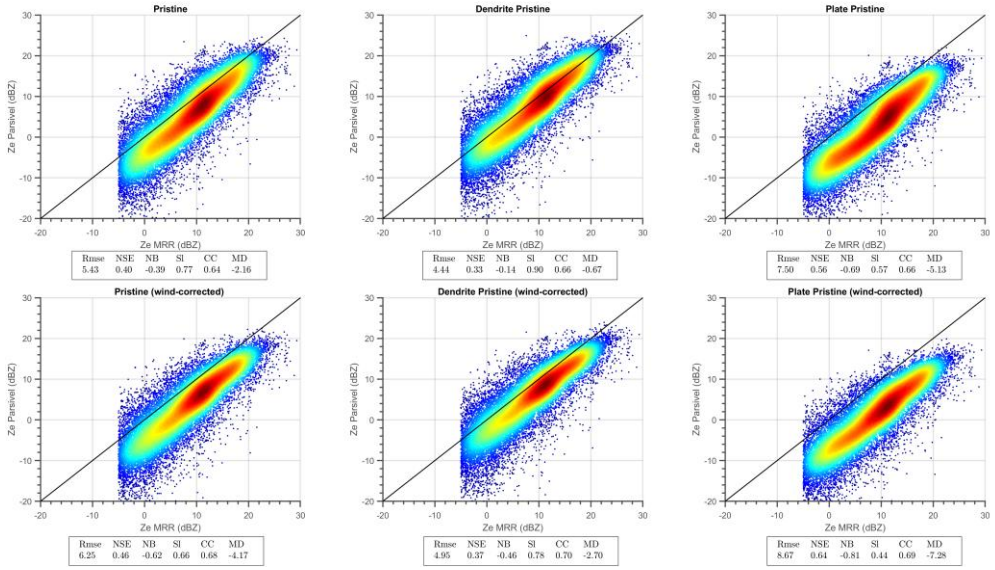

Figure 15 - Same as Figure 14 but for the three categories of pristine particles.

Overall, results show a very good agreement between the two instruments regarding radar reflectivity. In detail, for the aggregate-like categories, the method seems to reach the expected results. Considering scatter plots obtained with uncorrected data, the RMSEs for all the categories of aggregates defined in Table 1 are around 5 dB, with NSE around 0.40 and a correlation coefficient of about 0.6. On the other hand, among the three pristine categories, the statistical indexes of the pristine dendrite category show the best correspondence between the disdrometer and MRR *Ze*, characterized by a mean difference value of -0.67 dBZ.

A visual inspection of the scatter plots of Figure 14 suggests that the three aggregate categories present the best *Ze* comparison for low reflectivity values (below 10 dBZ), along with a clear overestimation for high *Ze*, confirmed by mean difference and normalized bias. The three pristine categories (Figure 15) exhibit a general underestimation of Ze_{MRR}, even though the dendrite pristine category performs satisfactorily for higher reflectivity values. The wind effect on PSD and, consequently, on Ze_{disd} can be highlighted by comparing plots on the upper row (uncorrected data) with those of the lower row (corrected data) of Figure 14 and Figure 15. Density scatters of uncorrected data show a peculiar "slope change" between lower and higher *Ze* values. This behavior yields a bulge in the plots (evident in Figure 14, upper row, and Ze_{MRR} around 10 dBZ), indicating the overestimation of Ze_{disd} with respect to Ze_{MRR}, particularly for higher radar *Ze*. Such behavior disappears in the plots obtained with wind-corrected data (Figure 14 and Figure 15, lower rows), indicating that PSD correction for wind effect on Parsivel measurements (see Section 3.5.1) reflects in lowering disdrometer derived reflectivity for higher *Ze* values.

Therefore, the artifacts due to the wind on raw Parsivel data, which consist mainly of an unusually high number of tiny hydrometeors, can seriously corrupt PSD and its derived quantities. Wind correction on Ze_{disd} seems to be confined to heavy snowfall, as the low reflectivity values do not appreciably change with mask application. This aspect may be explained since significant snow events at MZS are commonly accompanied by strong wind being connected to large low-pressure systems. Indeed, the density scatter plots for 1-min MRR and disdrometer data in terms of radar reflectivity for wind below and above 6 m s^{-1} (Figure 16 and Figure 17) clearly indicate the overestimation of Ze_{disd} and the general high MRR reflectivity values in cases of strong precipitation.

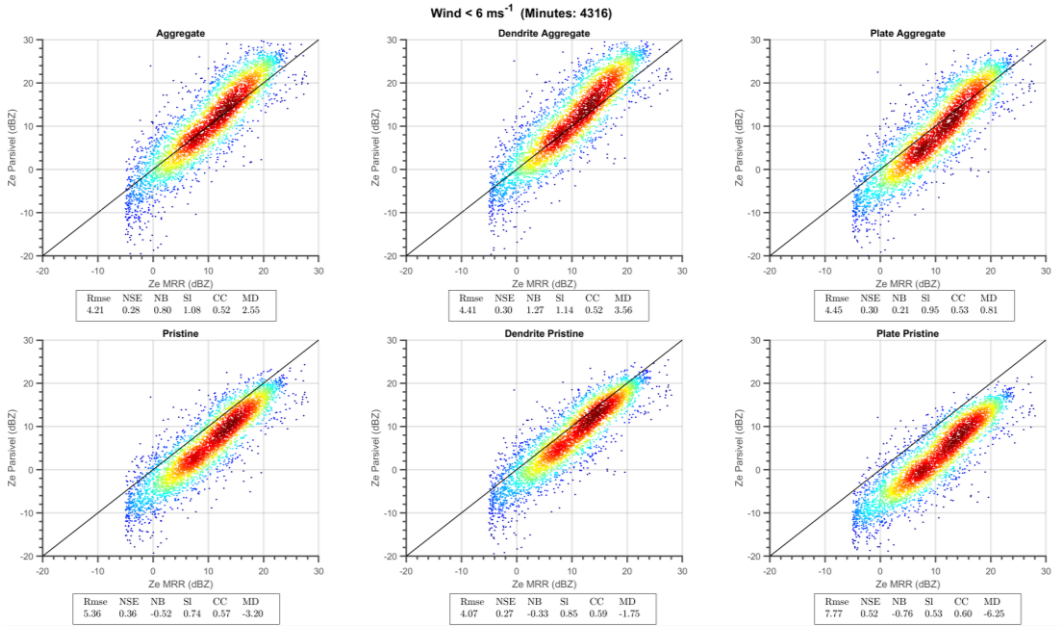

Figure 16 - Density scatter plots for 1-min MRR and disdrometer data in terms of equivalent radar reflectivity for summer season 2019-2020 in case of wind speed below 6 m s^{-1}. Disdrometer observations are not corrected for wind influence. Points are colored based on data density ranging from dark red (high density) to dark blue (low density), whereas the black line represents the bisecting line. Merit factors of the comparisons are also reported next to each plot.

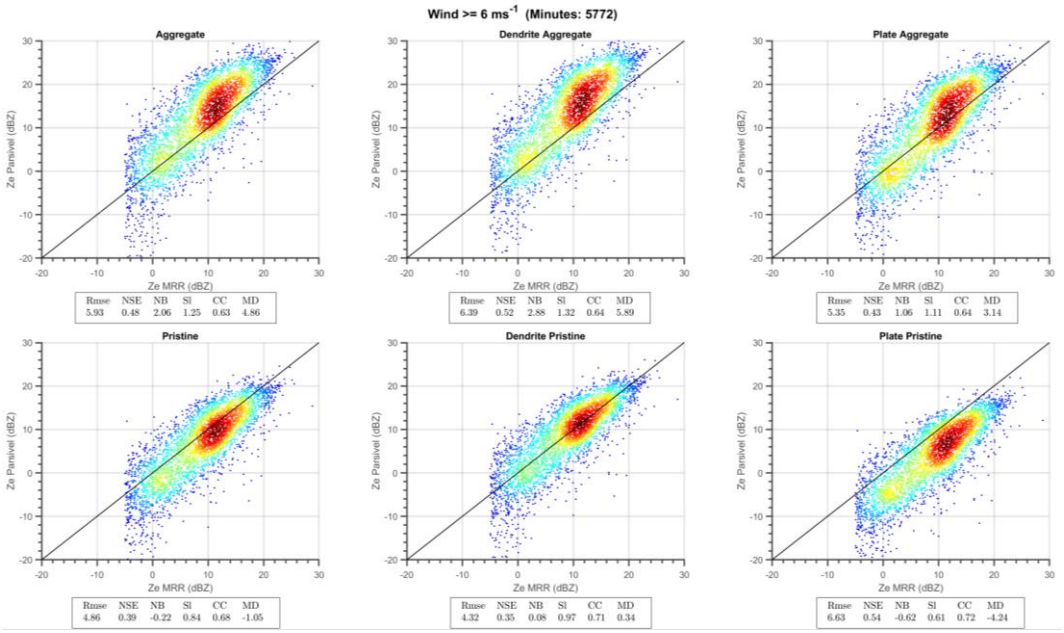

Figure 17 – Same as Figure 16 but in case of wind speed above or equal to 6 m s^{-1}

Correction of wind effects on PSD data significantly improves the correspondence between MRR and disdrometer in terms of equivalent reflectivity, especially for the three categories of aggregates, as shown in Figure 14, by RMSE values as well as normalized bias and normalized standard error for the aggregate and the dendrite aggregate categories. Even the mean differences reach the values of 1.04 and 2.02 dB, respectively, although the radar reflectivity of the two categories still overestimates the reference MRR measurements. On the other hand, the application of wind correction worsens the agreement for the other categories. In particular, the pristine and the plate pristine categories that are marked out by very low backscattering cross-sections failed to replicate MRR signals, resulting in a rough underestimation. In contrast, MRR measurements are simulated correctly for the dendrite pristine category, but only for a limited number of precipitation minutes (see Figure 15).

In summary, these results show that *Ze* obtained from the Parsivel and the MRR at 105 m above the Parsivel exhibits a good correlation. This is partially true if raw disdrometer data are used but applying the procedure for wind correction on disdrometer observations mitigates the effect of wind on the retrieval of the number and the size of falling hydrometeors that leads to an overestimation of the disdrometer-derived reflectivity, especially in case of intense precipitation as shown in Figure 14 and Figure 15.

4.2 *Ze-SR* relationships

Six relationships were calculated, one for each snow category, between radar reflectivity and snowfall rate ($Ze = a \times SR^b$), all computed from disdrometer observations, using a nonlinear regression approach to derive prefactor *a* and exponent *b* of the power-law relationship for each snow category. Then the proper relationship was applied to Ze_{MRR} measurements to obtain snowfall rates. Moreover, to appraise uncertainty, we performed 1000 iterations of the fit with 10% of randomly chosen observation data (~2360 min) for each snow category. Finally, from the 1000 values of prefactor and exponent obtained, we used the 5th and 95th percentile to assess the variability of *a* and *b* parameters in the *Ze-SR* relationships. Figure 18 shows the fits of the data and the related parameters of the *Ze-SR* relationships found. In each plot, the x-axis reports the snowfall rates derived from wind-corrected PSD, *m(D)*, and *v(D)* relationships for the different categories of particles as a function of the Ze_{disd} values.

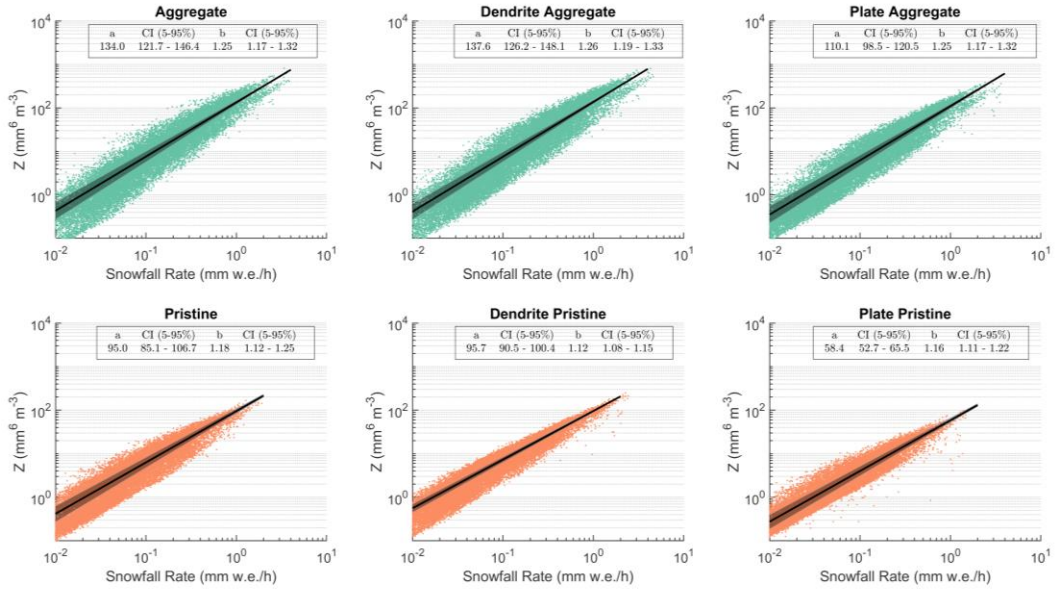

Figure 18 - Scatter plots of the snowfall rate and radar reflectivity both computed from disdrometer observations for each snow category. Black lines and shaded areas represent the Ze–SR relationships obtained through Nonlinear Least-Squares fitting and their uncertainties, respectively. Text boxes contain the fitting parameters found for each snow type.

Results show different values of *a* and *b* for the categories of aggregates and those of pristine particles (Figure 18, upper and lower row, respectively), whereas the variability is less marked within the two groups of categories. The dendrite aggregate and the aggregate categories reveal the larger prefactor values, while, in contrast, the exponents are similar.

The three categories of pristine particles show lower values of prefactors, especially that of plate pristine, while the exponents are similar but smaller than those of the categories of aggregates. These results are not unexpected. In fact, prefactor a is connected to the prefactors of the mass-diameter and the v-D relationships (von Lerber et al., 2017), and the used relationships have larger prefactor values for the aggregate categories (particularly for dendrite aggregate category) than for pristine categories, reflecting the m(D) relationships derived from Kuo database for each

snow category and used in this thesis (see Table 3). In the same way, *Ze-SR* exponents are similar within the same group (aggregate categories or pristine categories) but differ between the two groups, as they are linked to the exponent of *m(D)* relationships utilized that present the same behavior in its coefficient (Table 3). As discussed in some works (e.g., Schoger et al., 2021), the intercept (N_0) of the PSD expressed in exponential form can also have a role in shaping the *Ze-SR* relationship. However, fitting the observed PSD for each snow category (after the classification procedure) with an exponential form, a clear link between *Ze-SR* and N_0 was not found in this respect (cfr. Table 3 and *Ze-SR* relationships in Figure 18).

Table 3 – A list of the mass-diameter relationships in power-law form as derived from the Kuo database and of the intercepts of the measured PSDs (after classification procedure) fitted by an exponential function for each snow category.

Category	***Mass-diameter relationship*** $m = a_m D^{bm}$		***PSD exponential*** $N(D) = N_0 e^{-\lambda D}$
	Prefactor a_m	***Exponent*** b_m	***Intercept*** N_0
Aggregate	5.98×10^{-5}	*2.09*	*2.86*
Dendrite Aggregate	6.52×10^{-5}	*2.15*	*2.84*
Plate Aggregate	5.46×10^{-5}	*2.06*	*3.12*
Pristine	4.14×10^{-5}	*1.77*	*2.86*
Dendrite Pristine	4.93×10^{-5}	*2.01*	*2.86*
Plate Pristine	3.43×10^{-5}	*1.85*	*3*

Despite agreeing with several *Ze-SR* relationships found in the literature (Locatelli and Hobbs (1974), Matrosov et al. (2009), Grazioli et al. (2017a), von Lerber et al. (2017), Falconi et al. (2018), Scarchilli et al. (2020), and reference therein), the found *Ze-SR* parameters differ markedly from those reported in other works focusing on the Antarctic continent (see Table 4).

Souverijns et al. (2017) proposed a relationship (hereinafter S17) for Princess Elisabeth (PE) base, a research station approximately 200 km away from the coast. They found a very low value of prefactor (namely 18) that the authors associated with the small diameter of falling particles at that location, quite different from the larger ones observed in coastal sites. Thus, differences in snowflake size between inner and coastal Antarctica can translate into the characteristics of the *Ze-SR* relationship parameters.

Table 4 - List of the Ze-SR parameters in the literature for Antarctic sites and those found and used in this work. The location and the instrumentation set of each work are also included. Values in the brackets in the last two columns represent the confidence intervals.

Work			***Ze – SR relationship***	
Reference	***Antarctic Site***	***Instruments***	***Prefactor***	***Exponent***
Souverijns et al. (2017)	*Princess Elisabeth*	*MRR (300 m a.g.l) and PIP*	*18 (11-43)*	*1.10 (0.97–1.17)*
Grazioli et al. (2017a)	*Dumont D'Urville*	*MRR (300 m a.g.l.) and Pluvio*	*76 (69-83)*	*0.91 (0.78-1.09)*
Scarchilli et al. (2020)	*Mario Zucchelli*	*MRR (300 m a.g.l.) and LPM*	*54 (51-56]*	*1.15 (1.13-1.17)*
This Thesis (Aggregate)	*Mario Zucchelli*	*MRR (105 m a.g.l.) and Parsivel*	*134 (122-146)*	*1.25 (1.17-1.32)*
This Thesis (Dendrite Aggregate)	"	"	*137 (126-148)*	*1.26 (1.19-1.33)*
This Thesis (Plate Aggregate)	"	"	*110 (98-120)*	*1.25 (1.17-1.32)*
This Thesis (Pristine)	"	"	*95 (85-107)*	*1.18 (1.12-1.25)*
This Thesis (Dendrite Pristine)	"	"	*96 (90-100)*	*1.12 (1.08-1.15)*
This Thesis (Plate Pristine)	"	"	*58 (53-65)*	*1.16 (1.11-1.22)*

Our results also differ from the parameterization in Grazioli et al. (2017a) obtained at Dumont D'Urville (DDU) (from now on G17), a French coastal station, and even from those in Scarchilli et al. (2020) (henceforth S20) that used measurements from MZS that are partially overlapped with the database investigated in this Thesis. Since the instrumentation employed in S20, which consists of a different MRR set with the first usable measurements at 300 m a.g.l. and a Thies LPM disdrometer, is comparable with that used in this work; the differences include the MRR setting, disdrometer and MRR data processing, and assumptions in snowflake mass-diameter relationships. Indeed, it is worth highlighting that the unique characteristic of MRR measurements used in this Thesis is that they are collected at the 105 m height above the ground, while the other works listed in Table 4 were based on measurements collected at the height of 300 m and with a coarser resolution; only in Souverijns et al. (2017) was height correction for MRR data applied. In Antarctica, even during precipitation events, katabatic wind can lead to sublimation mechanisms acting on snowfalls in the lower atmospheric layers, as discussed earlier and widely described by Grazioli et al. (2017b). Such process can affect the correspondence between MRR and ground-based observations that, in turn, affects *Ze-SR* retrieval. In this respect, our MRR setup aims precisely to minimize this drawback and effectively maximize the correlation between MRR and disdrometer measurements.

Different data filtering or data processing methods can lead to different values of prefactor and exponent of the *Ze-SR* relationship. In this regard, we expect that the correction of raw disdrometer observations from wind artifacts, which implies censoring many particles, plays a prominent role in establishing adequate *Ze-SR*

relationships. Our approach aims to preserve most of the measurements with respect to data censoring approaches followed in other studies. In fact, PSD strongly affects the parameters, and large particles in PSD can result in a large *a* value and vice versa (Souverijns et al., 2017). Surprisingly, our results for aggregate are consistent with relationships found by (Huang et al., 2015) for snowfall events observed in Finland in which large aggregate hydrometeors were observed through a 2D video-disdrometer.

The mass-diameter relations derived from mass and size values of hydrometeors included in the Kuo database are consistent with field observations (Kuo et al., 2016). However, it is worth mentioning that the choice of the *m(D)* relationships has a significant influence that can result in different *Ze-SR* parameters. For this reason, several *m(D)* relationships and proposed *Ze-SR* relationships tuned on hydrometeor classification were used in order to consider the large variability of snow microphysical features in precipitation estimation.

Finally, it is worth noting that the relationship for the plate pristine category is nearly equal to S20. However, this snow category does not adequately represent features of the falling particle in the investigated events, as is evident from the density scatter plot shown in Figure 15.

4.3 Selection of the predominant hydrometeor class

Precipitation minutes were grouped into time frames of 10 min for each of the 52 snow events. Then, the methodology described in Section 3.3 using wind-corrected

Parsivel PSDs was applied for characterizing the falling particles in terms of the prevailing category. The results obtained are shown in Figure 19.

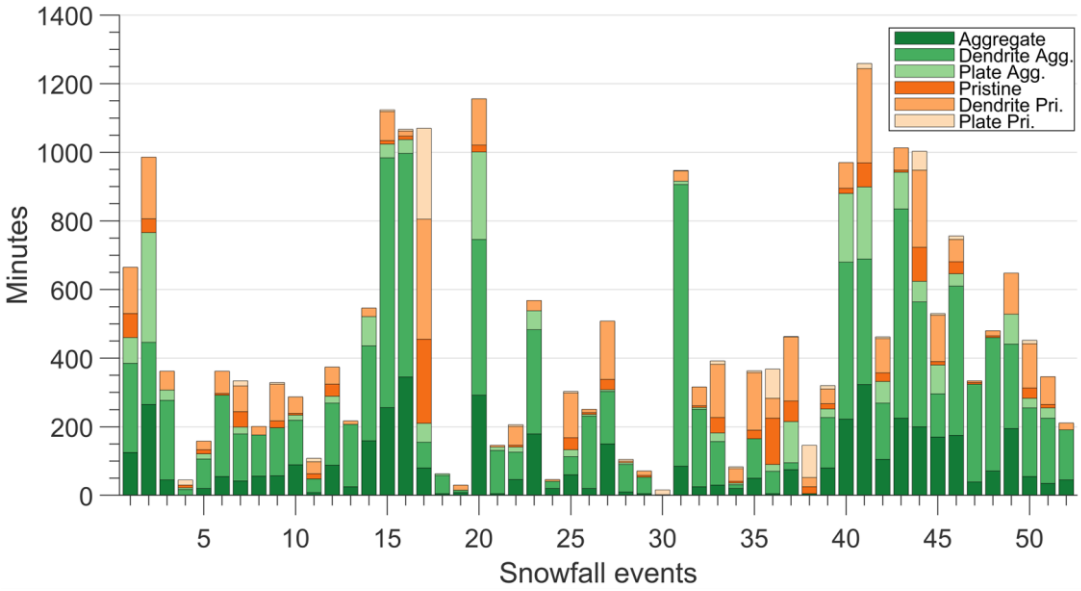

Figure 19 - Minutes of precipitation for each snow category and for each of the 52 snowfall events investigated in this Thesis for QPE purposes.

Categories of aggregates seem to better approximate the hydrometeors fallen at MZS during the periods investigated. Overall, the aggregate categories account for 17735 min out of 23566, with an incidence of more than 75%. In particular, the classification procedure identifies particles having specific dendrite aggregate features amounting to 45% of the total database, while 20% of the precipitation minutes are classified as belonging to the generic aggregate category. On the other hand, the categories of pristine snow seem to represent a minority (5830 min) and mainly exhibit dendrite pristine characteristics, while plate pristine appears only in 2.8% of the total minutes. However, most snowfall events show a mix of the different categories, and many of them display both aggregate and pristine features.

In contrast, only a single event (number 17 of 22 January 2020) consists almost solely of hydrometeors belonging to pristine-like categories. These results are consistent with other particle observations during snowfalls on the Antarctic continent, as Souverijns et al. (2017) also mentioned. Such measurements indicate that precipitation events can be formed either by the coexistence of pristine and aggregate hydrometeors (Lachlan-Cope (2010) and references therein) or by a singular pristine habit (Lawson et al., 2006).

Microphysical estimates from an X-band dual-polarization radar measurements and the high-resolution snowflake images collected by a Multiangle Snowflake Camera (MASC) performed at DDU coastal station (Grazioli et al., 2017a) showed that aggregates account for about 40% of all falling particles, a lower percentage than that of the events observed at MZS. However, MASC identified as small particles the vast majority (56%) of the hydrometeors at the ground level due to the strong influence of blowing snow in the measurement outcomes. Moreover, results also underlined the frequent occurrence of riming particles at that site, indicating that 11% of the hydrometeors are fully rimed, and many others have a rimed degree up to 0.5 (see Praz et al. (2017) for a detailed description). It is worth recalling that the Kuo database used in this work does not account for riming processes. Therefore, some rimed particles could not be appropriately classified. Finally, as classification is based on a comparison between instruments in terms of radar reflectivity, some large hydrometeors (aggregates) producing high *Ze* values could somehow hide the simultaneous presence of smaller and pristine crystals.

Density scatter plots and merit factors are again used to evaluate the classification methodology. In Figure 20, all the Ze_{MRR} measurements are compared with the

corresponding disdrometer-derived reflectivities after applying the hydrometeor classification procedure.

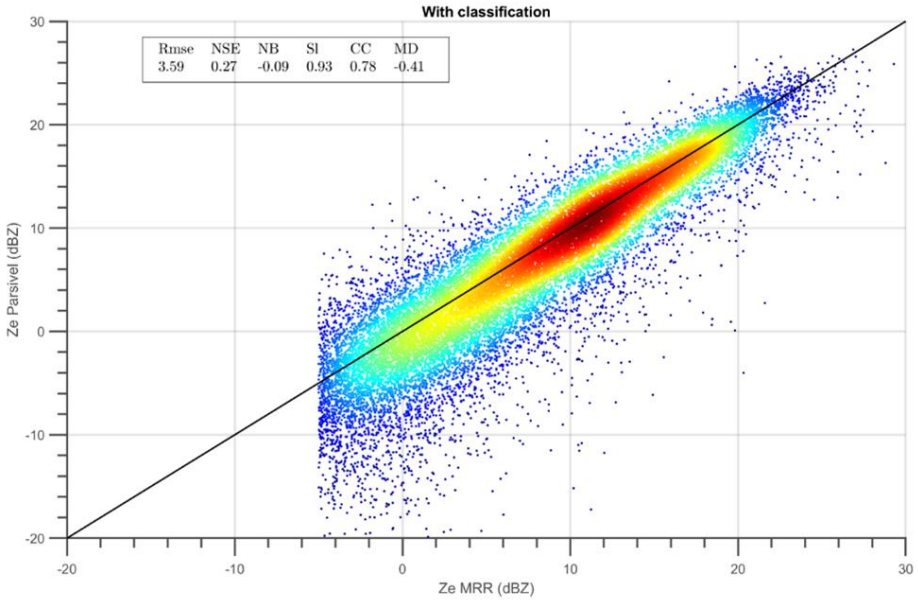

Figure 20 - Density scatter plots for 1-min radar and disdrometer data in terms of radar reflectivity after hydrometeor classification, as described in the text. Dots are colored based on data density, ranging from dark red (high density) to dark blue (low density). Black line represents the bisecting line. Merit factors of the comparison are reported in the text box.

As we can infer from the scatter graph, the applied methodology better matches the two estimates. On the one hand, the two reflectivities result in excellent agreement for the higher *Ze* values and even for the most occurring range of values around 10 dBZ (red and dark-red color). However, on the other hand, the MRR observations of lower reflectivities appear to be underestimated regarding the corresponding disdrometer-derived *Ze* values, which can occur in weak precipitation episodes. The corresponding improvement is also confirmed by the statistical indexes included as a text box in the figure (see Figure 14, Figure 15, and Figure 20): RMSE drops to 3.59 dBZ, while the NSE and the MD reach their minimum values. NB is slightly

negative, probably related to the underestimation at lower radar *Ze* discussed above. Finally, the correlation coefficient rises to 0.78.

4.4 Quantitative Precipitation Estimation

In each 10 min time frame, the proper *Ze-SR* relationship based on the classification procedure is applied to MRR measurements at the 105 m height to obtain the quantitative estimation of snow at the ground as:

$$SR = \left(\frac{Ze}{a}\right)^{\frac{1}{b}} \tag{22}$$

The accumulated snowfall at MZS for the events of the Antarctic summer periods of 2018–2019 and 2019–2020 is 84.6 water equivalent mm (mm w.e.), with uncertainty between 75.4 mm and 94.8 mm w.e., expressed by means of 5th and 95th percentile of the *a* and *b* parameters.

Firstly, to benchmark these outcomes, the results have been compared with other estimations obtained following different approaches, that is using only disdrometric data or employing only radar observations coupled with literature *Ze-SR* relationships.

Lastly, results have been compared with the independent estimates of accumulated snowfall from the TRwS-MPS weighing pluviometer.

4.4.1 QPE benchmark

4.4.1.1 *m(D)* and *v(D)* relationships

Accumulated snowfall values were determined using the formula for *SR* calculation (see Equation (16)) with wind-corrected Parsivel PSDs and different mass/velocity-diameter relationships to explore and quantify their influence in accumulation estimation. Moreover, this comparison can also highlight the extent to which a stand-alone disdrometer can return valuable estimates in snowfall without the support of co-located observations by other instruments that constrain microphysical relationships since the disdrometer does not perform any classification of the falling hydrometeors. Well-known mass-diameter relationships (Holroyd, 1971; Heymsfield et al., 2004; Brandes et al., 2007; Huang et al., 2010) were used, coupled with *v(D)* derived from Locatelli and Hobbs (1974), obtained with different methods and for different locations and particle types, to consider the natural variability of snow features better.

The comparison results are summarized in Table 5 (upper rows). They show high variability in the estimation of snowfall amounts obtained using only disdrometer data. The accumulated values range between 88 and 253 mm w.e. Comparing such values to the estimate obtained using the variable *Ze-SR*, differences vary from a minimum of +4% to a maximum of +199%.

Table 5 - Total precipitation estimation for the considered snow episodes calculated by different methodologies and relationships, specified in the first and second column, respectively. Note that 1 and 2 in the second column indicate the use of v(D) relationships for classes of aggregates (1) or of

pristines (2) derived from Locatelli and Hobbs (1974). *Differences in the last column are with respect to Variable Ze-SR estimation.*

Method	***Work***	***Accumulated precipitation (mm w.e.)***	***Difference (%)***
Variable Ze-SR	***This Thesis***	***84.6 (75.4 - 94.8)***	**-**
Disdrometer data, m(D) and v(D)	Holroyd (1971) - *1*	*227.5*	*+168.9*
	Holroyd (1971) - *2*	*152.5*	*+80.3*
	Heymsfield et al. (2004) - *1*	*144.6*	*+70.9*
	Heymsfield et al. (2004) - *2*	*97.7*	*+15.5*
	Brandes et al. (2007) - *1*	*253.1*	*+199.2*
	Brandes et al. (2007) - *2*	*171.6*	*+102.8*
	Huang et al. (2010) - *1*	*135*	*+59.6*
	Huang et al. (2010) - *2*	*88.2*	*+4.3*
Ze-SR relationship	Souverijns et al. (2017)	*629.2*	*+643.7*
	Grazioli et al. (2017a)	*74.6 (30.1 – 179)*	*-11.8*
	Scarchilli et al. (2020)	*259.4 (216.9 – 281.6)*	*+206.6*

The wide range of accumulation values indicates the dependency not only on the different mass-diameter relationships used but also on the considered terminal speed of hydrometeors. As mass and velocity are intrinsically connected to the habit and, more broadly, to the type of snow particles, the classification of solid hydrometeors seems necessary for applying the most proper microphysical relationships in *SR* calculation. Otherwise, in the absence of microphysical information or constraints from distinct instruments, selecting the suited relationships could be mere guesswork.

4.4.1.2 Literature *Ze-SR* relationships

The *Ze-SR* relationships developed for Antarctic sites and listed in Table 4 were employed to benchmark our methodology by applying them to MRR measurements at the 105 m height. The accumulated precipitation amounts are reported in Table 5 (lower rows). Results reflect the values of prefactors of each relationship, as expected. S17 returns the highest accumulation value (629.2 mm w.e.) as it is tailored for PE station, located far from the coast and with snowfall characterized by small precipitation particles and has a prefactor of 18. Instead, using the prefactor of 44 suggested in Souverijns et al. (2017) for locations close to the shoreline, the amount lowers to 279 mm w.e., which is still quite far from our findings. Calculation through G17 coefficients for the DDU site (74.6 mm w.e.) seems instead to be in line with our accumulation estimates. DDU is a coastal research station that, to some extent, presents snowfall characteristics comparable to the MZS site, and, in fact, G17 was also used to compute snowfall amount at MZS (e.g., Souverijns et al., 2018b).

Furthermore, we found a value of 259.4 mm w.e. making use of S20 developed for the MZS site, resulting in a difference of +206% compared to our findings and aligned with the formulas of Souverijns et al. (2017) modified for coastal sites.

Some considerations arise from these results. Again, the high spread of accumulated snowfall values indicates that choosing the proper relationship to be used is fundamental. Moreover, the extreme variability of snow microphysics suggests that using a single relationship in estimating the snowfall rate appears too limited, as differences have been found not only between different sites but even among events recorded at the same location. The latter evidence also indicates that the

methodology applied to achieve the *Ze-SR* formula can play a role in determining the *a* and *b* parameters, and, consequently, using the relationships described in the literature for *SR* estimations could lead to significant errors. Moreover, focusing on the MZS site, the discrepancies using S20 can also be explained not only by the differing mass-diameter parametrization but also by the different heights of the MRR measurements that can lead to quite different reflectivity measurements due to the well know sublimation mechanism acting in the lower Antarctic atmospheric levels (Grazioli et al., 2017b).

4.4.1.3 Weighing Pluviometer

Finally, estimates obtained with the *Ze-SR* mentioned above have been compared with the Alter shield weighing gauge observations provided by the TRwS-MPS described in Section 3.1.2.3. This instrument was already used in the comparative analysis with snowfall amount calculated through the *Ze-SR* relationship in Scarchilli et al. (2020). The TRwS was in operation for 32 out of 52 snow events of the analyzed period.

Figure 21 shows the comparison, in terms of accumulated snowfall values, between the weighing gauge measurements and the estimates using *Ze-SR* relationships, namely variable *Ze-SR* (proposed in this Thesis), S20, G17, and S17. In addition, the accumulation values contained in Scarchilli et al. (2020) and calculated using S20 and the other MRR installed at MZS are also included as a further benchmark.

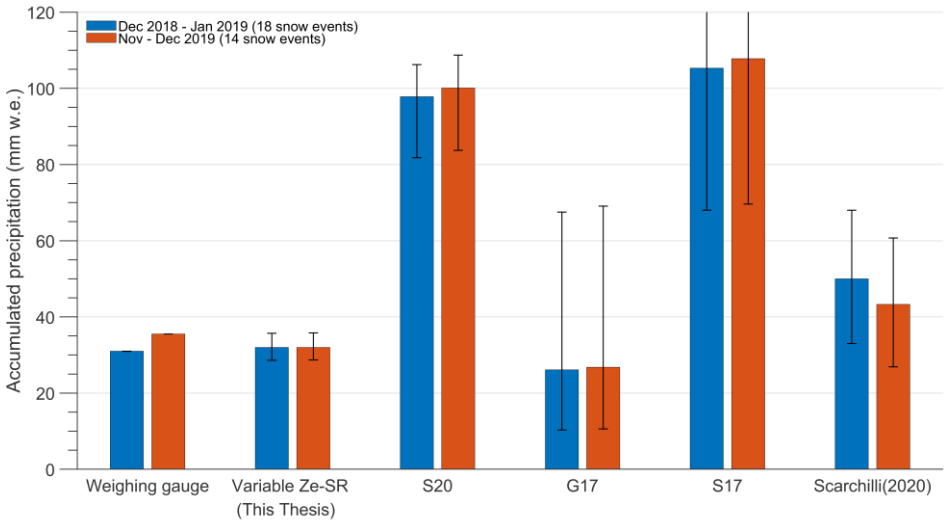

Figure 21 - Comparison in precipitation accumulation for the considered periods between the measurements of the TRwS weighing gauge and the estimates using different Ze-SR relationships. Variable Ze-SR refers to this Thesis, S20 to the Ze-SR relationship in Scarchilli et al. (2020)*; G17 to the Ze-SR relationship in* Grazioli et al. (2017a)*; S17 to the Ze-SR relationship in* Souverijns et al. (2017)*. Bars labelled with Scarchilli(2020) refer to precipitation estimates in* Scarchilli et al. (2020) *and calculated using S20 and the other MRR installed at MZS. Error bars are computed using confidence intervals of each Ze-SR relationship.*

The weighing gauge collected 31 mm w.e. in 18 snow episodes during the Antarctic summer campaign 2018–2019 and 35.5 mm w.e. during November and December 2019. The snowfall amount using variable *Ze-SR* relationship performs better than applying a fixed *Ze-SR* taken from the literature as resulting from the values closest to the reference ones in both the first and second observation period. Estimates using the G17 relationship are in line with our results, although with a slight underestimation for both periods and considerable uncertainty, while applying S20 and S17 leads to a significant overestimate. Accumulated values for the same periods, reported in Scarchilli et al. (2020), are slightly larger than our estimates using variable *Ze-SR* and TRwS measurements, whereas they are in line considering the uncertainty. Finally, it is worth noting that the estimates using S20 and our MRR measurements are significantly larger than those in Scarchilli et al. (2020), in which

the S20 relationship was applied to measurements by the other MRR at MZS set with a different vertical resolution.

Although carried out in different climatic regions, several studies support the advantage of using variable *Ze-SR* relationships. Rasmussen et al. (2003) developed an algorithm for snowfall nowcasting correlating real-time radar reflectivity and snow gauge data in the United States, deriving adaptive *Ze-SR* relationships. The improvement of the QPE is demonstrated because the variable *Ze-SR* relationship takes into account the natural variations of snow microphysics. The same conclusions can be found in von Lerber et al. (2017), where the link between radar and snow properties was examined thoroughly using measurements by video-disdrometer, pluviometer, and radar in southern Finland. It was shown that the *Ze-SR* relationship varies rapidly during a snowstorm, emphasizing the primary role of the prefactor value in the QPE, as also highlighted by the results of this Thesis. Schoger et al. (2021) faced a large spread in the QPE using different *Ze-SR* relationships from the literature, similarly to what is shown in Table 5. Applying *Ze-SR* relationships suited for different sites, including Antarctica, to the MRR data from Ny-Ålesund (Svalbard, Norway), they observed significant differences in snowfall rate and snowfall accumulation with respect to the reference measurements of a weighing pluviometer, ascribed to the different microphysical properties of the snow.

4.5 Vertical Profile of snowfall and sublimation

Exploring the vertical structure of precipitation is fundamental to understanding the dynamic and microphysical processes that guide hydrometeor formation and evolution. MRR observations at MZS have made it possible to investigate the vertical precipitation profile and obtain precious information on the vertical variation of snowfall.

In Figure 22, all the MRR precipitation profiles (from 105m up to 1050m) were depicted after applying a 6-hours moving average in order to make the graphical representation more informative. The figure points out the peculiar precipitation regime of Antarctica, which consists of few significant snowfall events often associated with atmospheric rivers (Souverijns et al., 2017) transporting moist air from the mid-latitudes to the higher ones (Gorodetskaya et al., 2014).

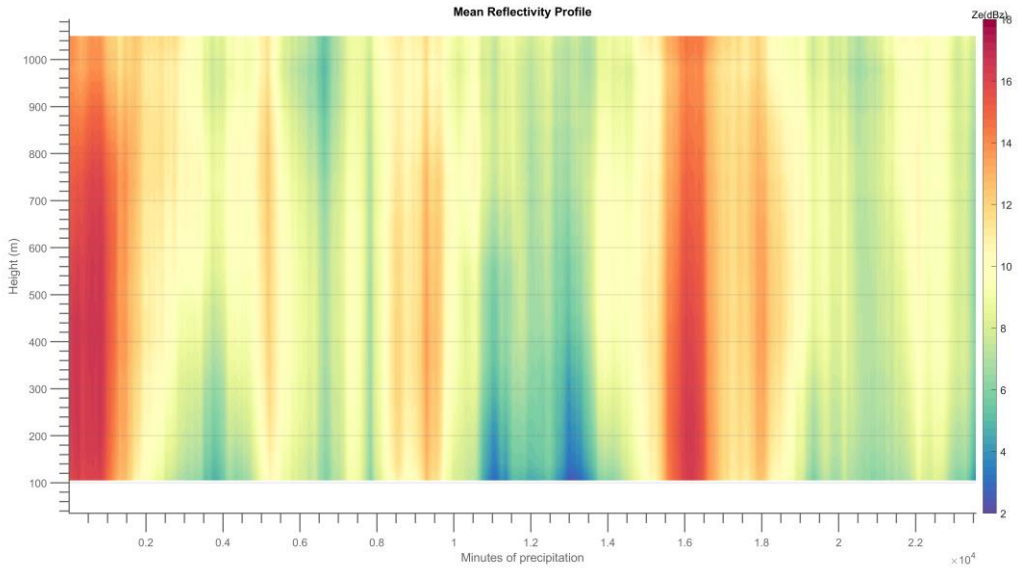

Figure 22 – Reflectivity profiles at MZS of the whole precipitation dataset (23.566 minutes of precipitation). A 6-hours moving average was applied to smooth the plot.

High *Ze* values along the entire profile alternate with profiles with lower reflectivities that decrease further approaching the ground, primarily when weak precipitation occurs. As discussed earlier, this process can be ascribed to the well-known mechanism of precipitation sublimation in the lower atmospheric layer in case of temperature inversion and unsaturated air conditions (Grazioli et al., 2017b). This mechanism is particularly effective in the coastal region of Antarctica also because of the intrusion of drier air from the plateau by the katabatic wind. It is worth underlining that a reduction of *Ze* values is particularly evident in the lowest atmospheric layers (from 300m to 100m) in some precipitation events, as well as a maximum of reflectivity at the altitude of 600-700m. In Figure 23, in which the average and the median profiles are drawn, these aspects are highlighted. Mean profile results to be slightly higher than median profile, probably due to the influence of few high reflectivity values in the average calculation. In general, both the profiles exhibit an increase in reflectivity from 1km to 400m above the ground, while the variation in the two highest MRR range gates is probably due to the high noise in the radar signal (Maahn and Kollias, 2012). Processes such as growth by vapor deposition, riming, or aggregation of ice crystals may produce a variation in the PSD along the profile leading to the observed increase of reflectivity values (Bechini et al., 2013; Schneebeli et al., 2013; Moisseev et al., 2015; Pfitzenmaier et al., 2018). Below 400m, a steep decrease in reflectivity is noted, probably in connection with the sublimation processes, as also pointed out by the high occurrence of profiles with reflectivity between 0 and 5 dBZ in the lower atmospheric layers. These results are in line with those discussed in Grazioli et al. (2017b), Souverijns et al. (2018b), and Durán-Alarcón et al. (2019).

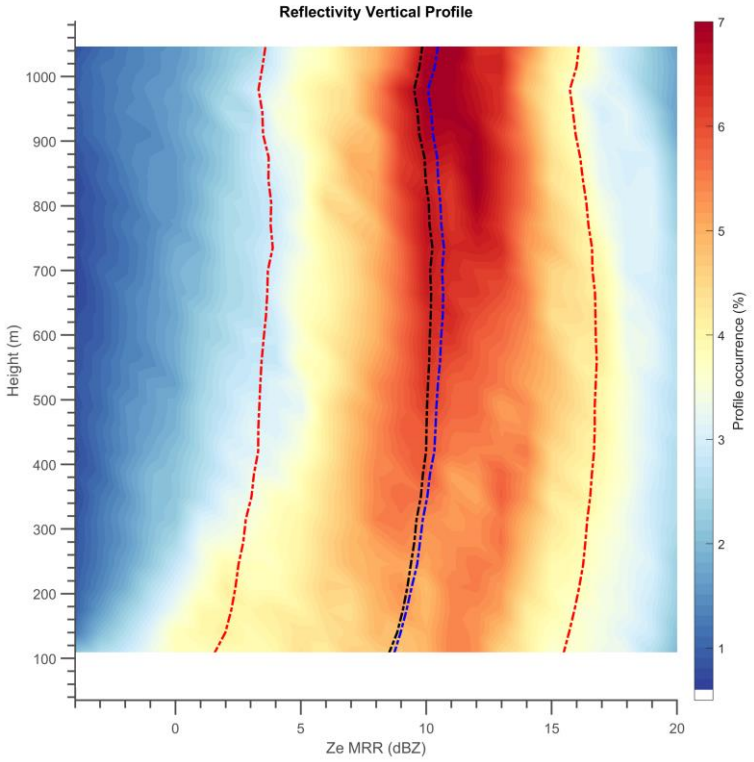

Figure 23 - Occurrence of the MRR reflectivity profiles considering the whole precipitation dataset (23566 minutes of precipitation). The dashed blue, black, and red lines represent the mean, median, and standard deviation vertical profiles, respectively.

Particularly in Durán-Alarcón et al. (2019), an extensive dataset (more than 5000 hours) of reflectivity profiles measured at DDU and PE stations by MRR has been investigated, pointing out that profiles of precipitation show significant differences between the two stations. In PE, only a general increase of reflectivity with decreasing altitude was observed, while the sublimation has a secondary role in that site, being located far from the escarpment zone and protected from katabatic winds. On the contrary, the DDU station exhibits a similar pattern to the outcomes found at MZS. The reflectivity increases as the height decreases, and a stepped decrease is observed in the layers closer to the ground. However, relevant differences were

identified when the mean reflectivity profile values were compared. The mean profile at DDU experiences a reflectivity maximum of 15.3 dBZ close to the ground followed by a decrease toward 14.7 dBZ at the height of 300m (the lowest available range bin of MRR at DDU, as mentioned earlier). The reflectivity profile at MZS is shown in Figure 24 (blue line). The reflectivity profile exhibits lower values than those at DDU, with a maximum of 10.3 dBZ at 735m height and a minimum of 8.5 dBZ at the lowest range gate (i.e., 105m). A difference of –5.1 dBZ with respect to the DDU mean profile is also observed at 300m height. The large diversity may be partly explained by the significant difference in datasets used (more than 5000 hours for DDU, about 400 hours for MZS), the different temporal integration, and the inclusion of nonsummer events in the DDU dataset. However, the difference in microphysical features of precipitation at the two Antarctic stations, both on the coastline, can have a role that deserves closer inspections.

Moreover, Figure 24 highlights the advantages of setting the MRR with a denser vertical resolution precisely because of the lower layers' decrease in *Ze* values. Reflectivity values of the lowest range gate are indeed needed in the *Ze-SR* relationships and QPE calculation, as discussed extensively in the previous sections, and having a radar measurement as close as possible to the surface is undoubtedly a plus point.

However, some height corrections can be applied to MRR data to consider the sublimation processes, as proposed in Souverijns et al. (2017). They extrapolated the trend in the lowest MRR vertical levels towards the surface to account for horizontal displacement and sublimation below the lowest measurement level at the PE station. This results, on average, in a decrease of 1.66 dBZ in reflectivity

between the lowest measurement level (i.e., 300 m) and the surface. Applying this extrapolation to the MRR mean profiles at MZS, a similar value (1.54 dBZ) is found, considering 315m as the lowest MRR level (Figure 24, yellow line). However, implementing the extrapolation in the actual lowest MRR level at MZS (i.e., 105m) results in an even lower *Ze* value at the ground because the decrease in reflectivity is enhanced in the levels closer to the ground (Figure 24, red line).

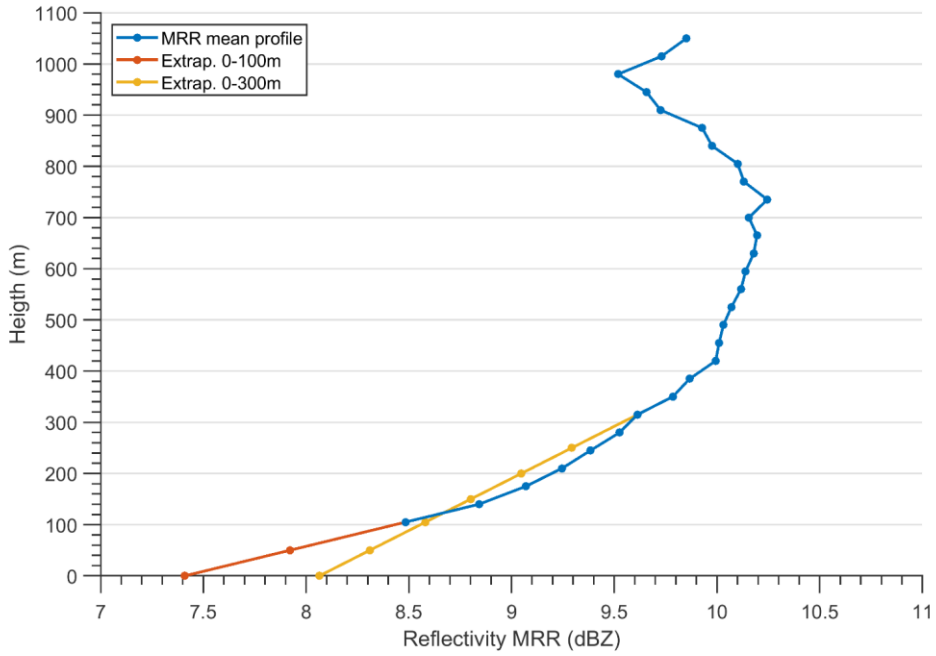

Figure 24 – Mean of the vertical reflectivity profiles (blue line) measured by the MRR considering the whole precipitation dataset (23566 minutes of precipitation). Yellow and red lines represent the extrapolations of the profile towards the surface, considering 300m and 100m as the lowest measurement level, respectively.

Last considerations strengthen the choice of using higher MRR resolution in estimating precipitation at the ground, especially in Antarctica, since MRR coarser resolutions and height correction appear not to be able to properly take into account the diminishing of reflectivity near the surface. In addition, as already mentioned,

the *Ze* reduction approaching the surface has repercussions on the QPE at the ground calculated using *Ze-SR* relationships. As a comparison, accumulated precipitation at different heights (i.e., 315m, 525m, 735m, 980m, 1050m) was calculated by using the MRR measurements, the *Ze-SR* relationships, and the hydrometeor classification described in this Thesis in order to achieve the variation of accumulated snowfall with the altitude. The results are shown in Figure 25 along with the QPE calculated using MRR reflectivity at 105m, already described in Section 4.4. Accumulated precipitation values ranging from 100.9 mm w.e. at 525m to 81 mm w.e. at the height of 980m. The best estimation for QPE at the ground (84.6 mm w.e. at 105m) appears to align with the values calculated at the highest range gates. On the contrary, it differs much from the values found for the middle layers. It is worth also underlining that considering the MRR measurement at 300m to calculate the QPE of a location leads to an overestimation of about 15% with respect to the QPE calculated through *Ze* at 105m (97.9 vs. 84.6 mm w.e. using the dataset investigated in this Thesis).

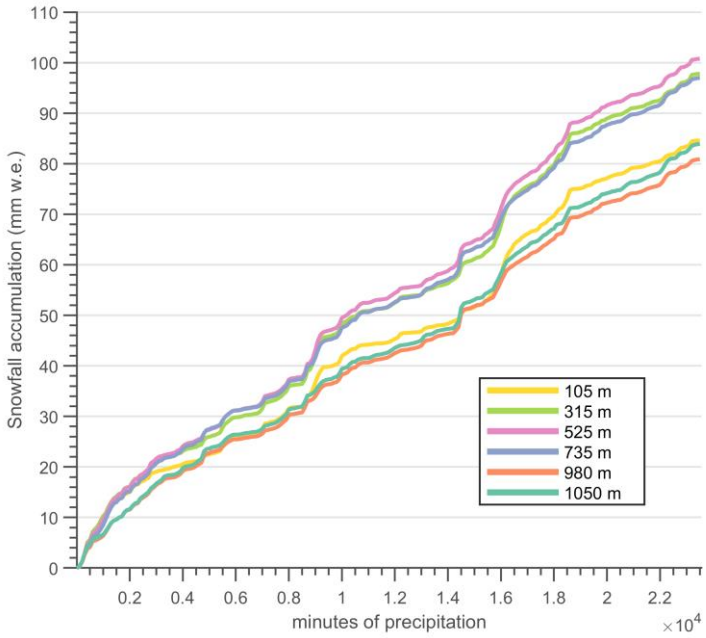

Figure 25 - Snowfall accumulated at MZS at different heights calculated by using the Ze-SR relationships found in this Thesis and listed in Table 4, and the MRR measurements at different range gates.

Finally, as defined in Section 3.4, the sublimation ratio was derived (Figure 26). Starting with the MRR reflectivity profiles shown in Figure 22, the *SR* for each MRR range gate was obtained using the methodology presented in the previous Sections. Then the *SubR* for each altitude was calculated through Equation (17), considering 105m as the reference height. Results show that a strong sublimation (*SubR* positive) acts in the lower levels with respect to the upper levels in case of weak precipitation (cf. Figure 26 and Figure 22), also in the order of magnitude of 30 - 40%. Again it is clear the differences in the layers closer to the surface comparing 300 and 100m height when lower values of *Ze* were observed. On the contrary, in the case of heavy snowfall, upper layers exhibit a negative *SubR*, highlighting the lower reflectivity values at upper altitudes compared to those of

the middle and lower levels, where processes such as growth by vapor deposition, riming, or aggregation of ice crystals may occur.

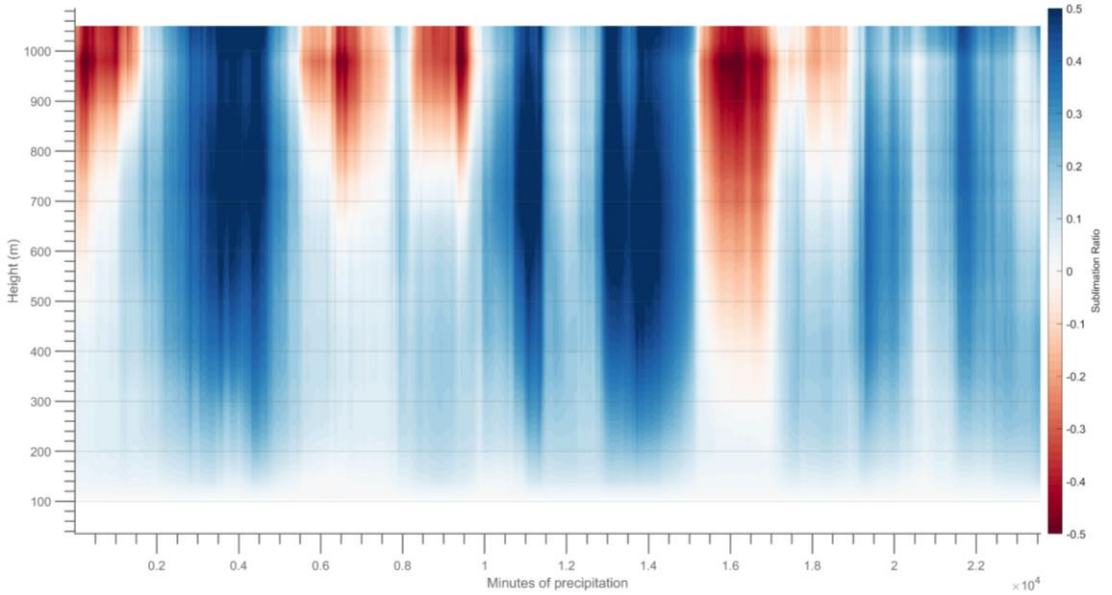

Figure 26 - Sublimation Ratio calculated for reflectivity profiles of MRR at MZS using definition described in Section 3.4

4.6 Below Cloud Scavenging

4.6.1 OPC Comparison Campaign in Bologna

The performances of OPC-N2 were evaluated by the comparison with a co-located reference instrument and other low-cost sensors under different sampling conditions as a preparatory benchmark before being sent and installed in Antarctica. This section presents and discusses the main results of this intercomparison exercise, focusing on mass.

4.6.1.1 Particle Mass Concentrations

Figure 27 and Figure 28 present the time series of hourly particle mass concentrations (PM_{10}, $PM_{2.5,}$ and PM_1) observed by the two SCKs (4E59 and

BC60), the two OPC-N2 (ABBA1 and ABBA2), the LOAC (during autumn) and the MetOne during the summer, autumn, and winter experimental campaigns carried out in Bologna, in order to study the effect of the seasonal variability. Notwithstanding the application of the Hampel filter, as detailed in Section 3.7.2, Figure 27 and Figure 28 highlight clearly that data collected from low-cost sensors in both seasons and from the LOAC during autumn are characterized by evident spikes in mass concentrations, usually not observed or at least less evident in the observations from the MetOne instrument. In addition, biases between the two types of low-cost sensors and the reference instrument are larger during the summer season (Figure 27) than during autumn (Figure 28). During both seasons, the most significant biases affect PM_1, while biases seem to be reduced for PM_{10}. Finally, Figure 27 and Figure 28 highlight that the two couples of SCKs and OPC-N2s are characterized by high correlations and very similar temporal patterns.

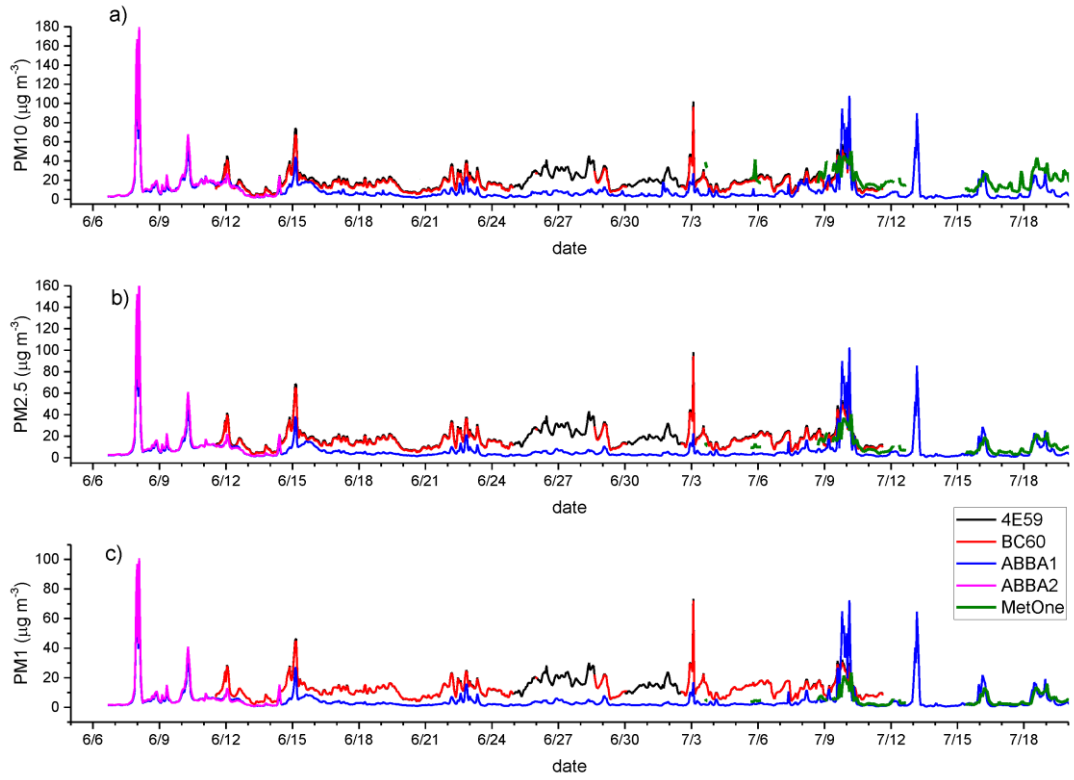

Figure 27 - Comparison of hourly PM_{10} (a), $PM_{2.5}$ (b) and PM_1 (c) (µg m^{-3}) mass concentrations from the co-located particle sensors during the summer measurement period in Bologna. 4E59 (black line) and BC60 (red line) are the two SCK (Smart Citizen Kit) sensors; ABBA1 (blue line) and ABBA2 (pink line) are the two OPC-N2 sensors from Alphasense, MetOne (thick green line) is the reference instrument.

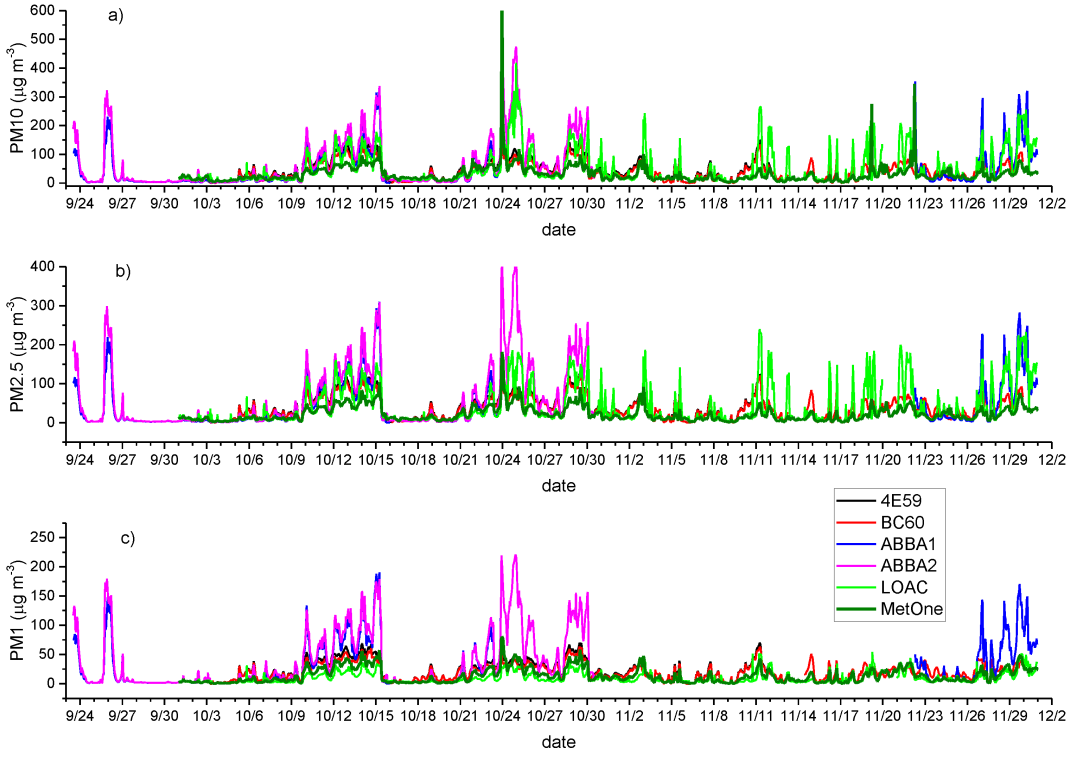

Figure 28 - Comparison of hourly PM_{10} (a), $PM_{2.5}$ (b) and PM_1 (c) (µg m^{-3}) mass concentrations from the co-located particle sensors during the autumn measurement period in Bologna. 4E59 (black line) and BC60 (red line) are the two SCK sensors; ABBA1 (blue line) and ABBA2 (pink line) are the two OPC-N2s sensors. LOAC (Light Optical Aerosols Counter) is the light green line. MetOne (thick olive green line) is the reference instrument.

A better understanding of how data collected from different particle sensors are related derives from the visual inspection of density scatter plots of 1-min observations during the two measurement campaigns carried out in Bologna (Figure 29 and Figure 30).

The comparison of summer data (Figure 29) highlights, even more, some patterns previously observed: observations of the two SCKs are very well correlated (R = 0.98, 0.99 and 0.99 respectively for PM_{10}, $PM_{2.5}$, and PM_1) and similarly distributed, while observations from the two OPC-N2s, even though similarly well correlated between each other (R = 0.91, 0.99 and 0.99 respectively for PM_{10}, $PM_{2.5}$,

and PM_1) seem to slightly deviate from a linear regression line, indicating some biases between the two sensors though of the same type.

When comparing observations from SCKs and OPC-N2s with those from the MetOne during summer (Figure 29), the density scatterplots show a better agreement for the $PM_{2.5}$ cut-off. At the same time, lower correlations are observed for PM_1 and even worse for PM_{10}. Indeed, low-cost sensors present evident tails in their populations, a feature particularly marked for the two SCKs (4E59 and BC60), in spite of their better correlation with respect to OPC-N2s (ABBA1 and ABBA2) for PM_{10} and $PM_{2.5}$. These tails are likely caused by the occurrence of instrumental spikes not removed by the Hampel filter, as observed by data clusters departing from the main data clouds in the scatter plots.

The comparison of autumn data (Figure 30) shows again that data from the two couples of low-cost sensors are reciprocally well correlated. The comparison with observations from the MetOne highlights higher correlations with respect to the summer season for PM_1 and $PM_{2.5}$ for both kinds of low-cost sensors and especially for the OPC-N2s, while for $PM_{10,}$ autumn correlations are higher than the summer ones only for OPC-N2s. Biases and tails are evidenced in the histograms and scatterplots for both types of low-cost sensors, even though clear clusters emerge in the case of the two SCKs. Moreover, all the data are mostly positioned above the bisector, suggesting that owing to the generally higher relative humidity of the autumn season in Bologna and the heating inlet of the MetOne, particle size measured by the sensors is different; the MetOne does not show the effect of the hygroscopic growth, as seen in detail later on. The observations from LOAC,

instead, show a different behavior, showing a general tendency to underestimate aerosol mass concentration with respect to the MetOne.

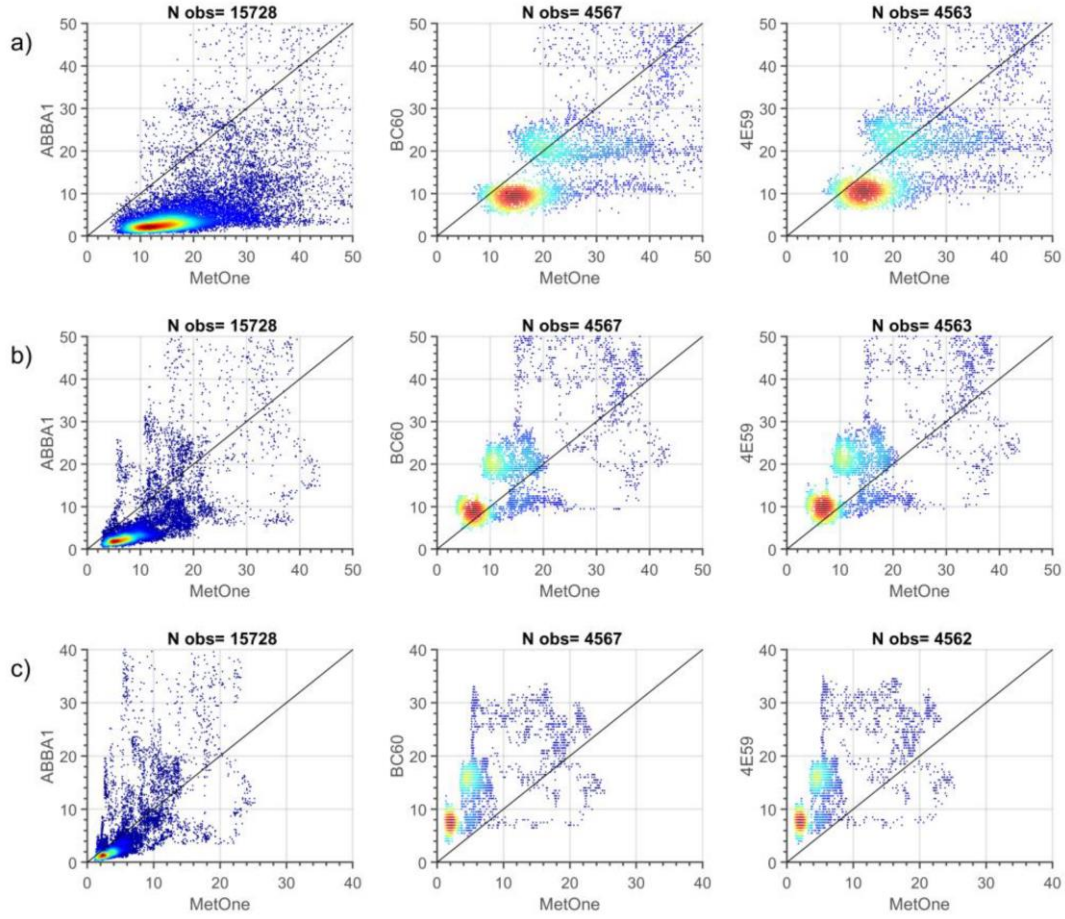

Figure 29 - Density scatter plot for of 1-min PM_{10} (a), $PM_{2.5}$ (b) and PM_1 (c) ($\mu g\ m^{-3}$) mass concentrations from the co-located particle sensors during the summer measurement period in Bologna. Points are colored based on data density ranging from dark red (high density) to dark blue (low density). N obs is the number of measurements for each pair of sensors.

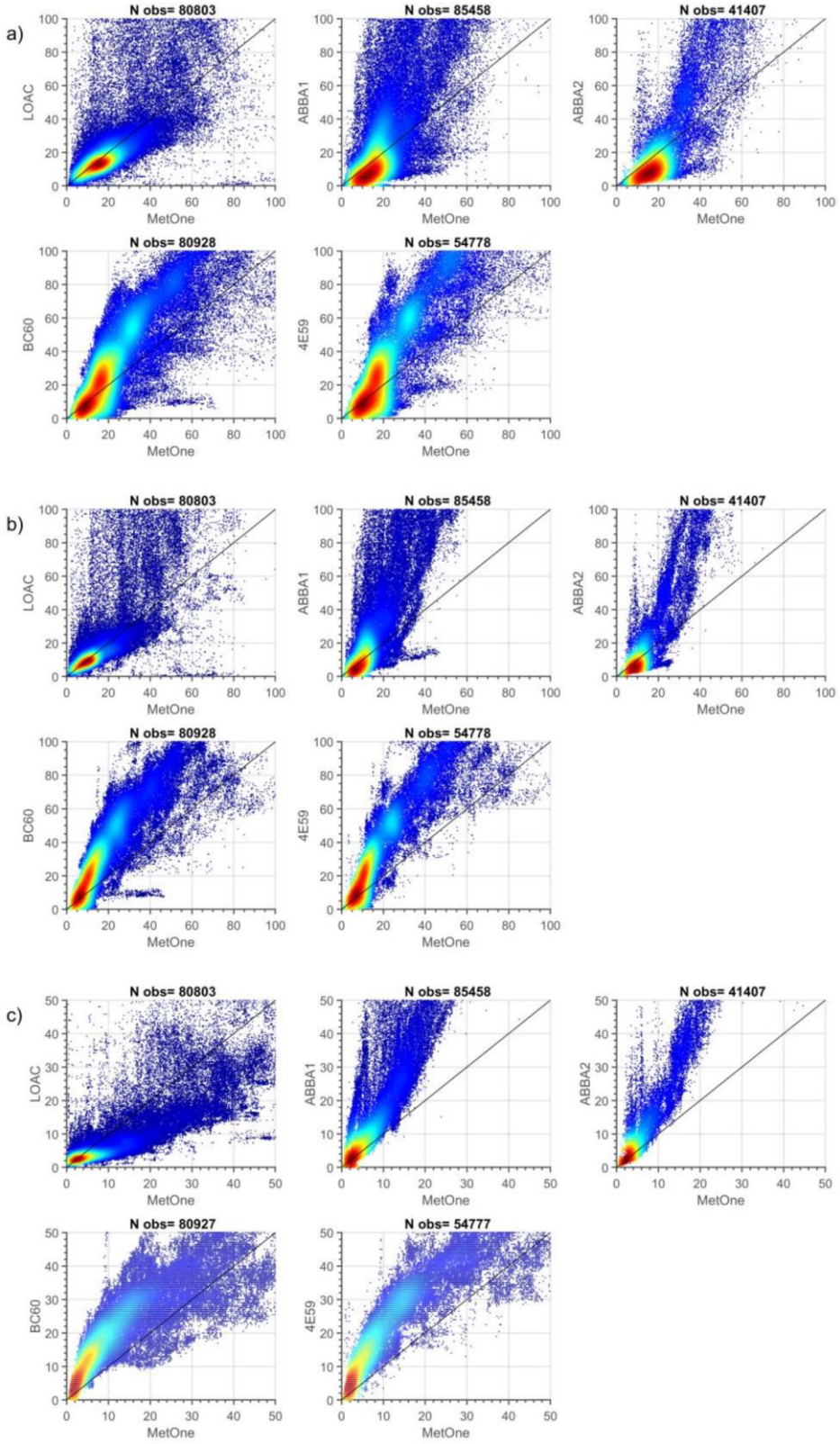

Figure 30 - Density scatter plot for of 1-min PM_{10} (a), $PM_{2.5}$ (b) and PM_1 (c) (µg m−3) mass concentrations from the co-located particle sensors during the autumn measurement period in Bologna. Points are colored based on data density ranging from dark red (high density) to dark blue (low density). N obs is the number of measurements for each pair of sensors.

In order to investigate the effects of time resolution on sensor performance, Figure 31 presents the evaluation of the performances of the sensors through the RMSE and the correlation coefficient at different time resolutions (from 1 min to 1 day) during the two measurement periods.

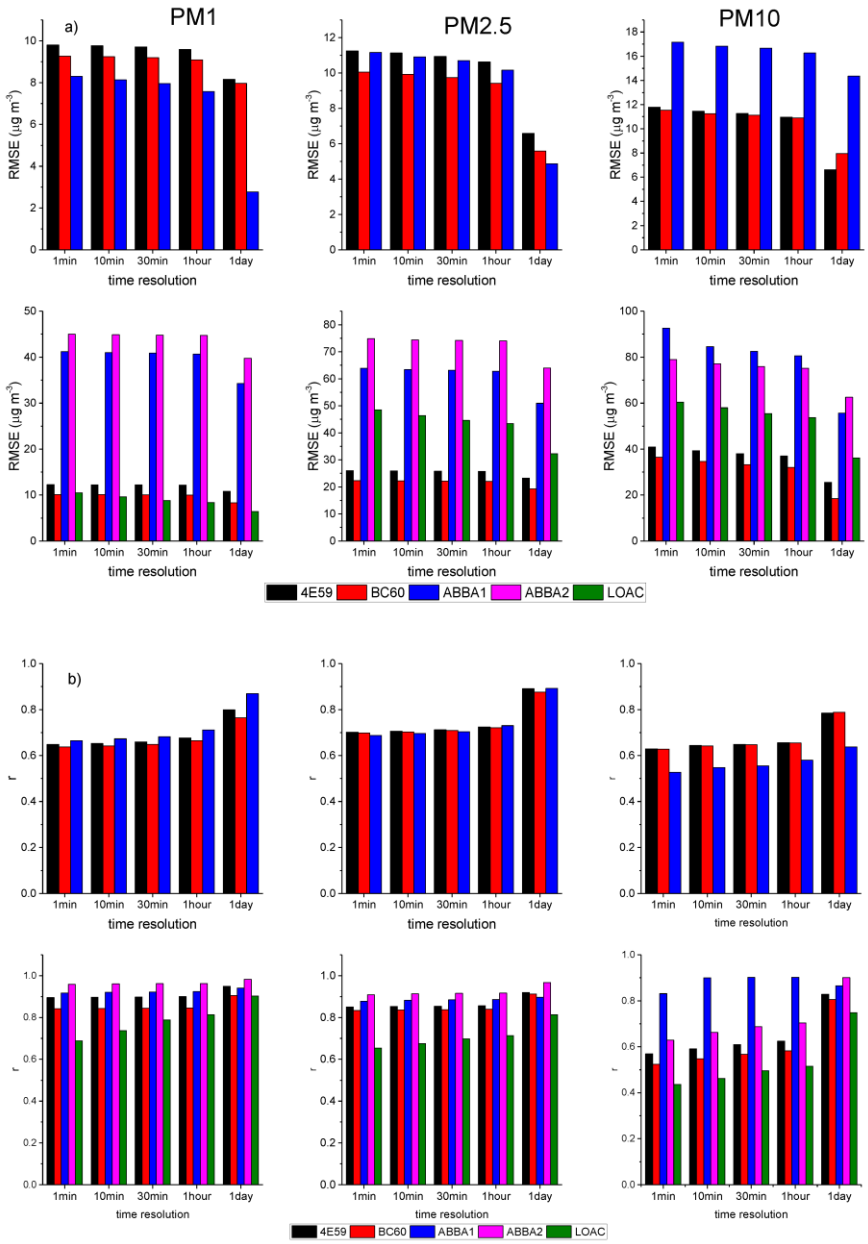

Figure 31 - RMSE (root mean square error) (a) and r Pearson correlation coefficient (b) of the optical sensors in measuring PM_1, $PM_{2.5}$ and PM_{10} mass concentrations under varying time resolution (1 min, 10 min, 30 min, 1 h and 1 day) using the MetOne as the reference sensor and

during the two-measurement periods in Bologna (summer in the upper panel, autumn in the lower panel).

During both measurement periods, the values highlight a tendency for the performance of the low-cost sensors to improve with lower time resolutions, as evidenced by the increasingly higher correlation coefficients. The comparison of the summer and autumn values shows that, as previously observed, the agreement of the sensors is higher during autumn, though also accompanied by higher biases in this season. The performances of the two couples of low-cost sensors within the brand type are very similar. In general, during both measurement periods, the SCKs are more consistent with MetOne than the OPC-N2s in the case of PM_{10} concentrations, while OPC-N2s reveal lower biases for $PM_{2.5}$ and PM_1.

The measurement period included different meteorological conditions typical of the warm and cold seasons in the measurement site. Specifically, with the aim of understanding the effects of different weather conditions on the performances of the optical sensors, the effects of the prevailing weather conditions were investigated based on the meteorological variables observed in situ from the co-located meteorological station and a WMO (World Meteorological Organization) synoptic meteorological station located at the Bologna airport, synoptic weather charts, atmospheric vertical soundings at a nearby meteorological station and maps of dust transport over the Mediterranean region, as simulated by the BSC-DREAM 8b model from the Barcelona Supercomputing Center (https://ess.bsc.es/bsc-dust-daily-forecast). The weather conditions observed were the following: thunderstorm, Saharan dust transport, rainfall, mist, fair weather, cloudy conditions, fog, and drizzle. Figure 32 and Figure 33 present the performances of the optical sensors during these different weather conditions as evaluated from the calculations of

MAE, MBE and RMSE indexes, and correlation coefficients using the MetOne sensor as a reference instrument.

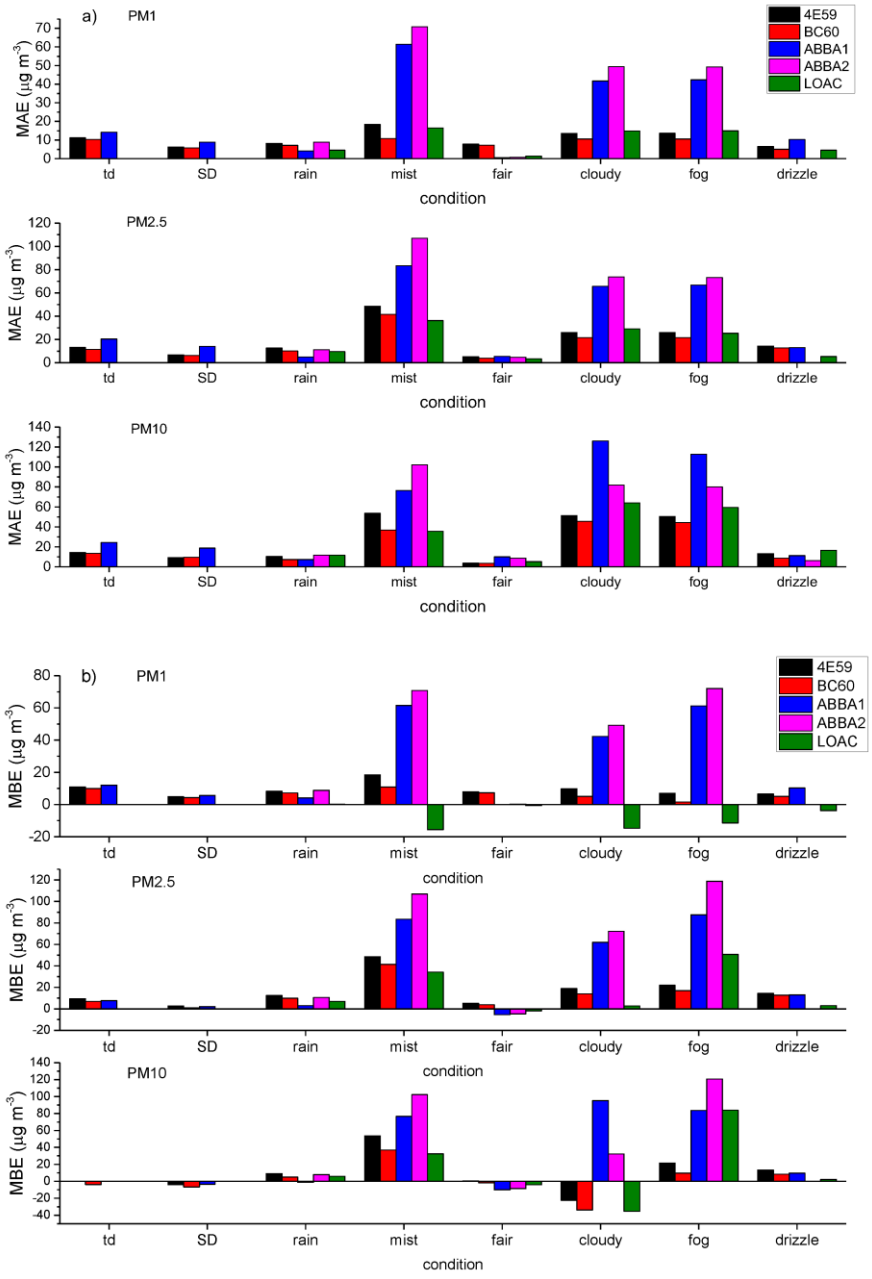

Figure 32 - Evaluation of the performances of the different optical sensors in measuring PM_1, $PM_{2.5}$ and PM_{10} mass concentrations under varying weather conditions (thunderstorm = td, Saharan dust transport = SD, rain, mist, fair weather, cloudy, fog, drizzle) using the MetOne as the reference sensor by calculating the following indexes: (a) MAE (mean absolute error); (b) MBE (mean bias error).

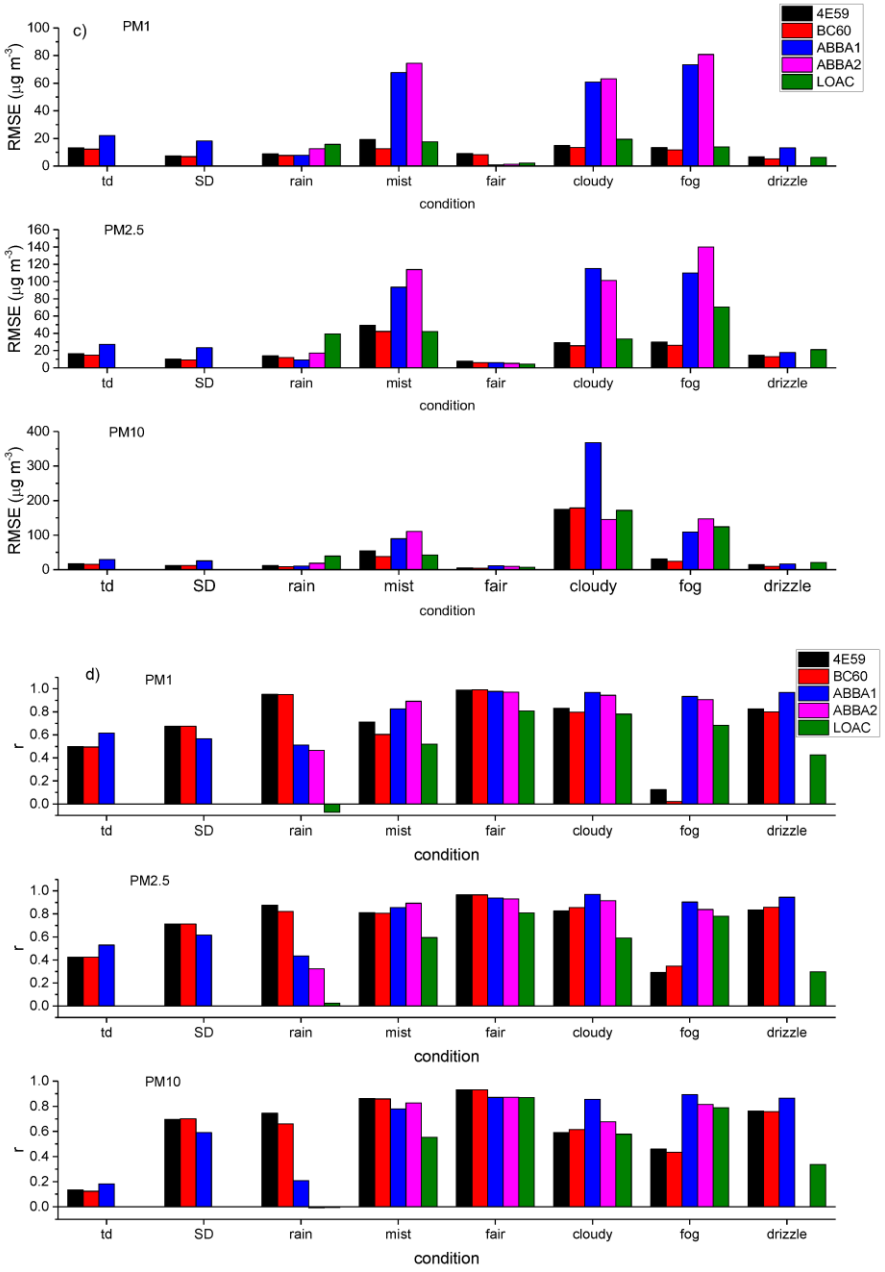

Figure 33 – Same as Figure 32 but for (c) RMSE (root mean square error) and (d) r (Pearson correlation coefficient).

As seen in Figure 32 and Figure 33, the performances of all the sensors are the highest during fair weather conditions, when the lowest values of the MAE, MBE, and RMSE are reported, associated with high correlation coefficients (>0.80) for all size fractions. Conversely, the performances of the sensors sensibly worsen

under mist, cloudy, and fog conditions, as expected given the hygroscopic behavior of aerosols. The comparison among the different sensors shows the higher performance of the OPC-N2s and the LOAC in capturing PM_1 concentrations under fair weather, while the SCKs perform better for $PM_{2.5}$ and particularly for PM_{10} concentrations. Figure 32 and Figure 33 show how the SCKs present a satisfactory, though never exceptional, performance under all weather conditions. The OPC-N2s and the LOAC reveal variable behaviors ranging from excellent performance with fair weather down to fairly biased and poorly correlated under cloudy and fog conditions. The OPC-N2s present high average correlations (>0.6) for most weather conditions except for the Saharan dust transport and rain events. The differentiated behavior of the other sensors may stem from several factors differently affecting particle counts in the various size bins and how they are used in PM assessment. One of the primary factors is basically the different particle size bins and the overall size intervals of each model, leading to an approximation in the instrumental comparison. Secondly, optical sensors are characterized by distinct particle size-selectivity (Kuula et al., 2020). Thirdly, the use of a constant density factor across the various size ranges to convert number densities to mass concentrations is likely an oversimplification, owing to the intrinsic complexity of PM composition (highly inhomogeneous across the size distribution) and to the direct and indirect influence of meteorology on particle size and composition (Johnson et al., 2018). In fact, the enhanced bias among the various sensors observed during the Saharan dust transport should be ascribed to the use of a density factor unsuitable for capturing the prevailing mineral component of the particles associated with this kind of transport. All the other biases instead are attributable mainly to the influence of

relative humidity on particle size as a result of variable hygroscopic growth leading to an overestimation of particle mass by the optical sensors with respect to the MetOne sensor endowed with the inlet heater.

In summary, the intensive long-term experimental field campaign indicated that the low-cost OPCs could be impacted by biases and low correlation, especially in high relative humidity conditions. However, the performance improves when lowering the time resolution to hourly or daily averages. Focusing on OPC-N2, it had proved to have an excellent performance in case of fair weather and to be effective in measuring PM_1 concentrations. Nevertheless, some shortcomings arose in conditions of high relative humidity. Therefore, with the view of employing OPC-N2 in the Antarctic context, some precautions have been taken. Firstly, only the first five size bins have been considered (from 0.38 up to 1.6 μm) because OPC-N2 has proven to be reliable in that size range and also considering the characteristic of aerosol dimensions at MZS (as described in Section 3.6). Secondly, according to the results of the OPC comparison, 6-hours averaged values of the OPC concentration measurements were used, therefore limiting the impact of the high relative humidity level on aerosol observations.

4.6.2 Snowfall scavenging at MZS

Figure 34 and Figure 35 show the two investigated snowfall events occurring at MZS during the XXXVI Italian Antarctic expedition. For each episode, the time series of Parsivel (in terms of detected particle min^{-1}) and OPC-N2 (in particle counts min^{-1}) for five size bins are reported to highlight the interaction between precipitation and aerosol concentration.

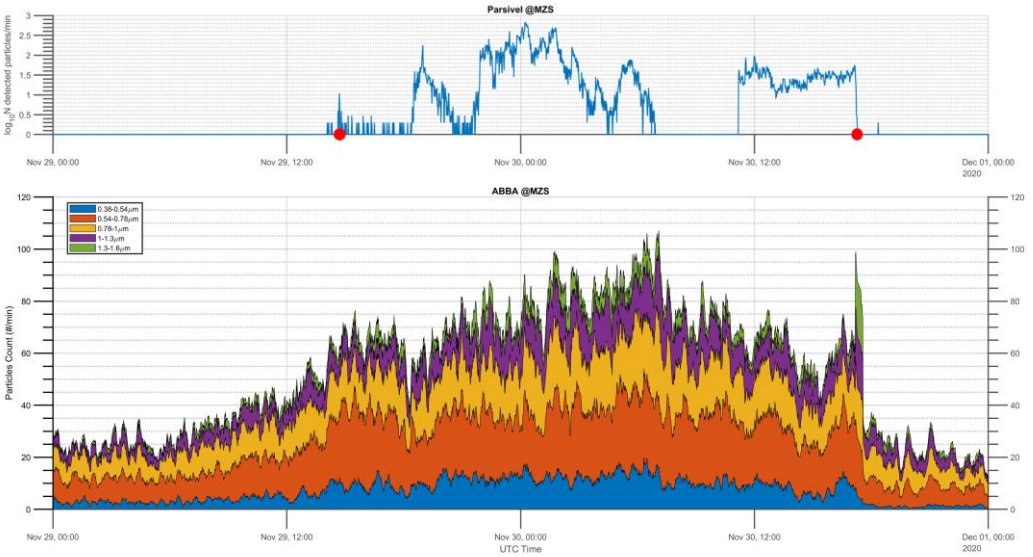

Figure 34 - 29-30 November 2020: Time series (at 1-min temporal resolution) of the hydrometeors detected by Parsivel disdrometer (upper panel) and of the aerosol particles by the OPC-N2 (lower panel) divided in the different size bins. Red markers represent the beginning and end of the precipitation event as defined in Section 3.6.

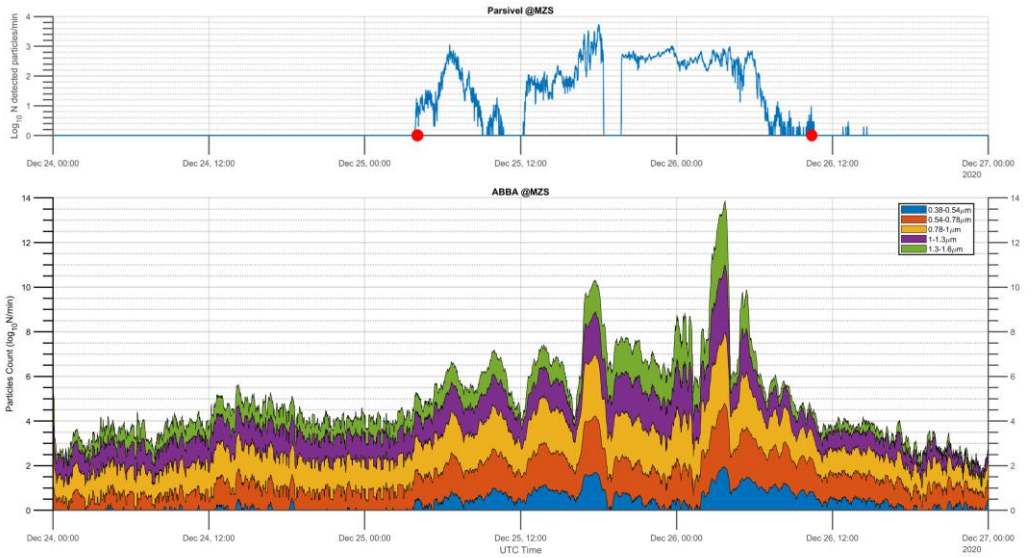

Figure 35 - 25-26 December 2020: Time series (at 1-min temporal resolution) of the hydrometeors detected by Parsivel disdrometer (upper panel) and of the aerosol particles by the OPC-N2 (lower panel) divided in the different size bins. Red markers represent the beginning and end of the precipitation event as defined in Section 3.6.

The first considered snowfall occurred on 29-30 November 2020 and lasted 30 hours. Qualitative analysis of the time series indicates an increase in aerosol

concentration right after the beginning of precipitation in all the dimensional ranges followed by a stepped decrease at the end of snowfall. The increase in particle counts is probably related to instrumental interaction with tiny hydrometeors and hygroscopic growth of aerosols. A similar pattern was followed in the snowfall event on 25-26 December 2020 (27 hours duration). However, the increase and decrease of aerosol concentrations were less pronounced. Furthermore, in contrast to the first event, particles of the lowest size bin of the OPC exhibit different behavior, as they were detected only in association with the beginning of the precipitation event.

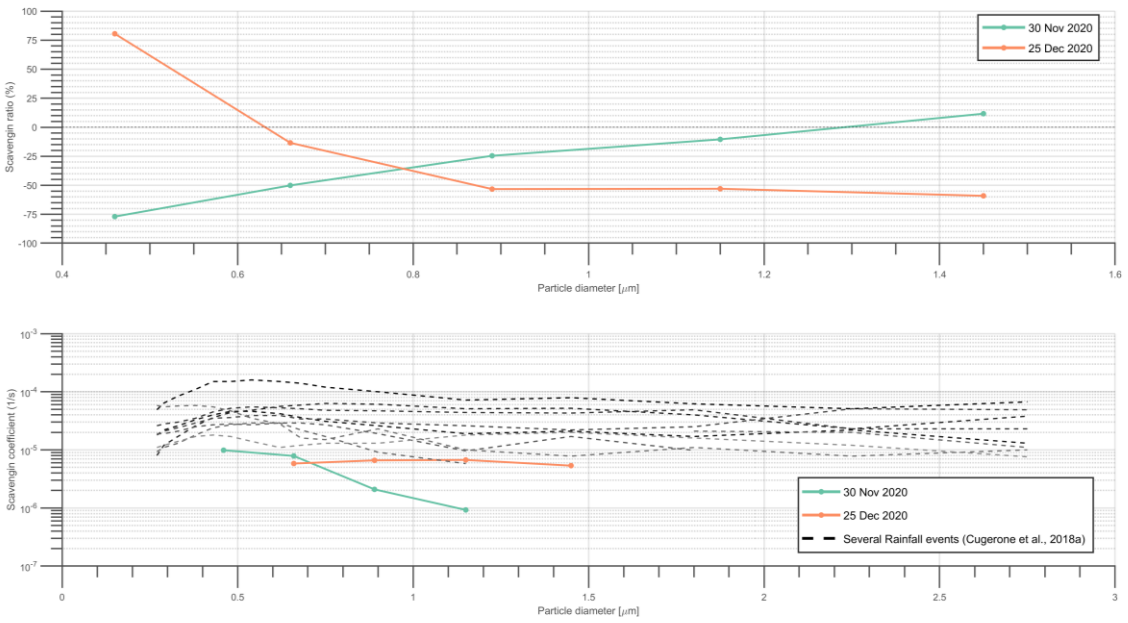

Figure 36 – Scavenging ratios (upper panel) and scavenging coefficients (lower panel) for the two snowfalls investigated at MZS. As comparing parameters, the dashed black lines in the lower panel represent scavenging coefficients calculated for rainfall (Cugerone et al., 2018a).

In order to quantify the scavenging effects of snowfall on aerosol at MZS, the scavenging ratio and scavenging coefficient were calculated and are shown in

Figure 36, upper and lower panel, respectively. Scavenging processes turned out to be most effective in the middle size bins (0.54 -1.3 μm), with ΔC values between -15 and -55% depending on aerosol size. Opposite behavior was found for particles ranging from 0.38 to 0.54 μm, which shows an apparent reduction in the first snowfall, while ΔC reached 80% in the second event. Different trends were also observed for larger aerosol particles, a reduction on 29-30 November an increase for 25-26 December episode.

Positive scavenging coefficients for the two events are shown in the lower panel of Figure 36, using Equation (12), in which also scavenging coefficients referred to several rainfall events in an urban context (Cugerone et al., 2018a) were added as a basis for comparison. Snowfall coefficients found at MZS, ranging between 9.2×10^{-7} s^{-1} and 9.9×10^{-6} s^{-1}. Scavenging was particularly effective during the first snowfall for the lowest OPC bins, while in the second event, scavenging coefficients appeared to be constant for all size bins.

The achievement of scavenging coefficients also made it possible to compare MZS results with theoretical and experimental studies carried out in other locations, bearing however in mind the scarcity of BCS dataset at MZS. Results found in Antarctica are consistent with several theoretical parametrizations for the size-resolved scavenging coefficients (e.g., Zhang et al., 2013; Wang et al., 2014) and also for those found in Feng (2009) focused on planar ice crystals. However, a clear Greenfield gap was not observed, as instead indicated in those studies, probably because of the short size range of the aerosol particles detected. Compared with other experimental campaigns, outcomes at MZS are lower than scavenging coefficients calculated for sites out of Antarctica. As shown in Figure 36, rain

scavenging, obtained for 10 rain events in an Italian urban site (Cugerone et al., 2018a), appears to be more effective than that calculated at MZS, as expected for rainfall. However, the results at MZS are even lower than those of some snow-scavenging works on literature. For example, in Finland, Paramonov et al. (2011) found λ values ranging between 1.8×10^{-6} and 4.2×10^{-5} s^{-1} in an urban environment for aerosol particles with sizes overlapping to those investigated at MZS, while coefficient values ranging from 8.7×10^{-6} and 5.2×10^{-5} s^{-1} were shown in Kyrö et al. (2009) at a rural background location. Even higher values were found for snow scavenging in a site in the Czech Republic ($1.4 \times 10^{-5} – 9.6 \times 10^{-5}$ s^{-1}). In conclusion, the Antarctic's pristine atmosphere and scarcity in aerosol probably lead to less effective snow scavenging. Nevertheless, firm conclusions require much more evidence and case studies to allow the analysis to go deeper.

Chapter 5

5 Summary and Conclusions

In this Thesis, the Antarctic precipitation at the Mario Zucchelli coastal site has been thoroughly investigated under different points of view: microphysical features, QPE, vertical structure, and scavenging properties.

A new approach to quantitative snowfall estimation using a variable *Ze-SR* relationship based on the microphysical classification of hydrometeors was presented. This is obtained by comparing co-located Micro Rain Radar and Parsivel disdrometer observations coupled by means of a DDA backscattering model in terms of radar reflectivity. To this end, data from 52 precipitation days at the Mario Zucchelli Italian Antarctic station collected during the 2018–2019 and 2019–2020 summer periods were analyzed and processed for a total of 23566 observed snowfall minutes. Before proceeding with the analysis, disdrometer data were corrected from the wind influence by a new approach that assigns a reliability weight to each Parsivel bin based on simultaneous disdrometer and wind measurements. This novelty tends to progress beyond the more used censoring method which cuts hydrometeors deviating from reference size and diameter intervals or outright eliminating precipitation data when the wind exceeds a predefined threshold that could result in heavily decimating data. Based on these observations, the consistency of Parsivel and MRR measurements classified on six different snow categories was tested and then the corresponding six *Ze-SR*

relationships were derived. The method developed can also determine the predominant snow category in each 10-min time frame for all the precipitation events. Furthermore, we applied the *Ze-SR* relationship of the predominant snow category to calculate the cumulated snowfall amount in the analyzed periods based on such classification. Then the findings were compared against estimates derived using *m(D)*, *v(D)*, and the *Ze-SR* relationships available in the literature and against co-located measurements by a weighing gauge.

The vertical profiles of snowfall were also examined to investigate the dynamic and microphysical precipitation processes. A 6-hours moving average was applied to the MRR vertical data in terms of radar reflectivity to point out vertical precipitation features as enhancement of *Ze* related to ice particles aggregation or *Ze* reduction due to sublimation. In addition, the mean and median vertical profiles using the 23566 minutes were obtained to quantify the reflectivity decrease in the layers closer to the ground and compare the MZS profile with those of other Antarctic sites. Moreover, the MRR vertical profiles were exploited, along with snow classification and *Ze-SR* relationships, to obtain the variation of the accumulated snowfall with the altitude. Then, *SR* rates at different heights were also used to calculate a modified sublimation ratio for the precipitation at MZS with the view of highlight sublimation layers.

Measurements of aerosol particle concentrations at MZS were performed through a low-cost OPC to investigate the correlation between snowfall and aerosol in terms of scavenging ratio and scavenging coefficient. An air quality monitoring system

(ABBA) was assembled with an Alphasense OPC-N2 and meteorological and gaseous pollutant sensors. The OPC-N2 was tested using a co-located reference instrument and other low-cost sensors in two distinct experimental field campaigns carried out in Bologna. After the comparison, the OPC-N2 was installed at MZS during the XXXVI Italian Antarctic expedition. The only two snowfall episodes of that summer season were analyzed by means of Parsivel and OPC-N2 observations. Based on these measurements, the scavenging processes at MZS were assessed and compared against others snow scavenging values available in the literature.

The main results of the whole Thesis work are summarized as follows:

a) Comparisons of *Ze* derived from disdrometer and MRR at the 105 m height show good agreement, even for nonwind-corrected Parsivel data (Figure 14 and Figure 15, upper rows), indicating the potential of the synergic use of such instrument set, despite comparing volume and point measurements but minimizing the vertical distance between the instruments;

b) The correspondence significantly improves using wind-corrected PSD, especially for higher reflectivity values (Figure 14 and Figure 15, lower rows). Wind creates artifacts consisting mainly of a large and unusual number of tiny solid hydrometeors that corrupt PSD retrievals, leading to overestimating *Ze*-derived values. As strong winds usually accompany significant snow events, correction of raw disdrometric data appears mandatory in snowfall estimations, and the use of snow-reliability weight

on disdrometer bins represents a valid alternative to the threshold approach in disdrometer data filtering (Figure 13);

c) 75% of the precipitation minutes investigated at MZS were classified as aggregate with a significant percentage of dendrites (Figure 19). Only 5830 min out of 23566 falling particles showed pristine characteristics. These results differ from those found at DDU (40% aggregate type). Only one snow episode is found consisting almost entirely of pristine hydrometeors and definitely deserves a closer inspection;

d) After hydrometeors classification, 84.6 mm w.e. of accumulated snowfall were estimated for the events observed during the summer seasons 2018–2019 and 2019–2020, using the variable *Ze-SR* method and benchmarked this outcome with other approaches (Table 5). It was found that calculating snow amount using disdrometer data alone heavily depends on the mass and velocity parametrizations applied, resulting in a spread of precipitation accumulations ranging from 88.5 to 253.1 mm w.e. Similarly, using only MRR data and *Ze-SR* relationships from the literature, accumulated snowfall values lie between 74.6 and 629.2 mm w.e.;

e) Results were assessed by referencing the measures by a weighing pluviometer installed at MZS during 32 out of the 52 considered days (Figure 21). The accumulated snow estimation from the variable *Ze-SR* relationship results in the best agreement (64 mm w.e. vs. 66.5 mm w.e. by

the pluviometer) regarding estimates obtained with fixed *Ze-SR* relationships;

f) Analyzing MRR vertical profiles, a reduction of *Ze* values is evident in the lowest layers (100 – 300m), as well as a *Ze* maximum at the altitude of 600-700m (Figure 22 and Figure 23). The latter is probably connected with riming or aggregation of ice particles, the former to sublimation processes. Such vertical profile deeply affects QPE if higher reflectivity measurements are considered (Figure 24);

g) Mean reflectivity profile (Figure 24) proves to be about 5 dBZ lower than the *Ze* profile at DDU. The large discrepancy could be partly explained by the significant difference in the amount of data used and different temporal integration. However, both different MRR vertical resolution and different microphysical snow properties can take part in;

h) The results of comparative OPC campaigns indicate that low-cost sensors, and all OPCs, are affected by biases and low correlations when working at elevated time resolution, while the performance improves when lowering the time resolution to hourly or daily averages (Figure 31);

i) Performance of a sensor is highly impacted by the prevailing weather conditions, suggesting particular caution in their use for estimating PM concentrations at high relative humidity conditions, such as rain and fog

events. Conversely, their performances under conditions of weak synoptic forcing and prevailing anticyclonic conditions were in general characterized by low biases and elevated correlation coefficients (Figure 32 and Figure 33);

j) OPC and Parsivel observations at MZS have shown the intrinsic connection between aerosol particles and snowflakes, in which precipitation drives enhancement and decrease of aerosols concentrations (Figure 34 and Figure 35), although the interaction is not always straightforward;

k) Scavenging coefficients were calculated for Antarctic aerosol with diameters from 0.38 to 1.6 μm and ranging between 9.2×10^{-7} and 9.9×10^{-6} s^{-1} (Figure 36). These values are sensibly lower than those in literature for rainfall scavenging, but even lower than those contained in works dealing with snow scavenging in urban and rural contexts.

Because of the first considerations, the combination of MRR and a disdrometer is undoubtedly valuable and workable in snowfall estimations. In contrast, disdrometer or radar data alone rely on relationships (mass-diameter and velocity-diameter for the former, *Ze-SR* for the latter) whose selection is not straightforward in the absence of other observations and can lead to very different results. Their synergic use makes it possible to constrain such relationships, thanks to the precious information which can be obtained on snow microphysical features.

Moreover, the extreme variability of snow microphysical features results in significant uncertainties in snowfall estimations. Instead of a static one, the use of variable *Ze-SR* relationship makes it possible to mitigate the impact of such variability, as has been effectively demonstrated by the improvement in snowfall quantitative estimations.

Furthermore, the findings in this Thesis also warn against the simplistic (although common) use of *Ze-SR* relationships reported in the literature for snowfall amount computation. Since relationships are calculated with specific microphysical assumptions and are deeply tied to the instrument setting used and the methodology followed, it could be tricky to apply them to different sites and similar instrumentation with different settings. Indeed, even relationships tailored for the same site, namely MZS, can lead to different accumulated snowfall estimates.

In addition, the inspection of the peculiar Antarctic vertical profiles of precipitation stresses the importance of the radar height measurements in quantitative precipitation estimates, as the results may significantly differ.

Regarding the OPC comparison, results have shown that whatever the application of OPCs is, and in particular for that of low-cost sensors, the intelligent use of the data is advised based on the following recommendations:

a) Data from these devices are precious and extremely informative;
b) They can be used reasonably confidently in fair weather conditions and with low time resolution;

c) Careful data treatment and evaluation are required in two main cases: airsheds affected by mineral dust, and more generally, during relatively high humidity conditions, rain and fog are observed.

In conclusion, this Thesis intends to provide an in-depth broadband analysis of Antarctic precipitation at the MZS site, proposing new methodologies for the correction of disdrometer data and QPE by means of microphysical information, investigating the vertical precipitation profile, and obtaining, to the best of my knowledge, the first quantification of the scavenging coefficients in Antarctica.

The presented results, achieved through an affordable set of instruments, give rise to advances in knowledge of the characteristics of snowfall in the Antarctic continent, contributing to a better assessment of the SMB of the Antarctic ice sheet, the major player in the global sea-level rise.

Although this Thesis presents a consistent database of 52 days of precipitation, future works are required to validate further the microphysical classification of hydrometeors employing different ground instrumentation, such as imaging disdrometers, to calculate accumulated snow. Similarly, the dataset for BCS must be expanded to make findings on scavenging processes more robust and adding other atmospheric measurements as wind and humidity would be helpful.

Finally, the natural follow-on of this Thesis could develop by applying the frame of the analysis reported here to the wintertime Antarctic snowfalls and to different sites and climatic conditions.

References

Adirosi, E., Baldini, L., Tokay, A., 2020. Rainfall and DSD Parameters Comparison between Micro Rain Radar, Two-Dimensional Video and Parsivel2 Disdrometers, and S-Band Dual-Polarization Radar. *J. Atmos. Ocean. Technol.*, **37**, 621–640. https://doi.org/10.1175/JTECH-D-19-0085.1

Andronache, C., 2003. Estimated variability of below-cloud aerosol removal by rainfall for observed aerosol size distributions. *Atmos. Chem. Phys.*, **3**, 131–143. https://doi.org/10.5194/acp-3-131-2003

Ardon-Dryer, K., Levin, Z., Lawson, R.P., 2011. Characteristics of immersion freezing nuclei at the South Pole station in Antarctica. *Atmos. Chem. Phys.*, **11**, 4015–4024. https://doi.org/10.5194/acp-11-4015-2011

Argentini, S., Mastrantonio, G., 1994. Barrier winds recorded during two summer antarctic campaigns and their interaction with the katabatic flows as observed by a tri-axial doppler sodar. *Int. J. Remote Sens.*, **15**, 455–466. https://doi.org/10.1080/01431169408954086

Argentini, S., Del Buono, P., Della Vedova, A.M., Mastrantonio, G., 1995. A statistical analysis of wind in Terra Nova Bay, Antarctica, for the austral summers 1988 and 1989. *Atmos. Res.*, **39**, 145–156. https://doi.org/10.1016/0169-8095(95)00009-G

Auger, M., Morrow, R., Kestenare, E., Sallée, J.B., Cowley, R., 2021. Southern Ocean in-situ temperature trends over 25 years emerge from interannual variability. *Nat. Commun.*, **12**, 1–9. https://doi.org/10.1038/s41467-020-20781-1

Badura, M., Batog, P., Drzeniecka-Osiadacz, A., Modzel, P., 2018. Evaluation of low-cost sensors for ambient PM2.5 monitoring. *J. Sensors*, **2018**. https://doi.org/10.1155/2018/5096540

Bae, S.Y., Park, R.J., Kim, Y.P., Woo, J.H., 2012. Effects of below-cloud

scavenging on the regional aerosol budget in East Asia. *Atmos. Environ.*, **58**, 14–22. https://doi.org/10.1016/j.atmosenv.2011.08.065

Bailey, M.P., Hallett, J., 2009. A comprehensive habit diagram for atmospheric ice crystals: Confirmation from the laboratory, AIRS II, and other field studies. *J. Atmos. Sci.*, **66**, 2888–2899. https://doi.org/10.1175/2009JAS2883.1

Battaglia, A., Rustemeier, E., Tokay, A., Blahak, U., Simmer, C., 2010. PARSIVEL snow observations: A critical assessment. *J. Atmos. Ocean. Technol.*, **27**, 333–344. https://doi.org/10.1175/2009JTECHA1332.1

Bauerová, P., Šindelářová, A., Rychlík, Š., Novák, Z., Keder, J., 2020. Low-cost air quality sensors: One-year field comparative measurement of different gas sensors and particle counters with reference monitors at tusimice observatory. *Atmosphere (Basel).*, **11**, 492. https://doi.org/10.3390/ATMOS11050492

Bechini, R., Baldini, L., Chandrasekar, V., 2013. Polarimetric radar observations in the ice region of precipitating clouds at C-Band and X-Band radar frequencies. *J. Appl. Meteorol. Climatol.*, **52**, 1147–1169. https://doi.org/10.1175/JAMC-D-12-055.1

Belosi, F., Contini, D., Donateo, A., Santachiara, G., Prodi, F., 2012. Aerosol size distribution at Nansen Ice Sheet Antarctica. *Atmos. Res.*, **107**, 42–50. https://doi.org/10.1016/j.atmosres.2011.12.007

Belosi, F., Santachiara, G., Prodi, F., 2014. Ice-forming nuclei in Antarctica: New and past measurements. *Atmos. Res.*, **145**, 105–111. https://doi.org/10.1016/j.atmosres.2014.03.030

Bezantakos, S., Schmidt-Ott, F., Biskos, G., 2018. Performance evaluation of the cost-effective and lightweight Alphasense optical particle counter for use onboard unmanned aerial vehicles. *Aerosol Sci. Technol.*, **52**, 385–392. https://doi.org/10.1080/02786826.2017.1412394

Blanco-Alegre, C., Castro, A., Calvo, A.I., Oduber, F., Alonso-Blanco, E., Fernández-González, D., Valencia-Barrera, R.M., Vega-Maray, A.M., Fraile, R., 2018. Below-cloud scavenging of fine and coarse aerosol particles by rain:

The role of raindrop size. *Q. J. R. Meteorol. Soc.*, **144**, 2715–2726. https://doi.org/10.1002/qj.3399

Blanco-Alegre, C., Calvo, A.I., Coz, E., Castro, A., Oduber, F., Prévôt, A.S.H., Močnik, G., Fraile, R., 2019. Quantification of source specific black carbon scavenging using an aethalometer and a disdrometer. *Environ. Pollut.*, **246**, 336–345. https://doi.org/10.1016/j.envpol.2018.11.102

Botta, G., Aydin, K., Verlinde, J., Avramov, A.E., Ackerman, A.S., Fridlind, A.M., McFarquhar, G.M., Wolde, M., 2011. Millimeter wave scattering from ice crystals and their aggregates: Comparing cloud model simulations with X- and Ka-band radar measurements. *J. Geophys. Res. Atmos.*, **116**, 1–13. https://doi.org/10.1029/2011JD015909

Botta, G., Aydin, K., Verlinde, J., 2013. Variability in millimeter wave scattering properties of dendritic ice crystals. *J. Quant. Spectrosc. Radiat. Transf.*, **131**, 105–114. https://doi.org/10.1016/j.jqsrt.2013.05.009

Brandes, E.A., Ikeda, K., Zhang, G., Schönhuber, M., Rasmussen, R.M., 2007. A statistical and physical description of hydrometeor distributions in Colorado snowstorms using a video disdrometer. *J. Appl. Meteorol. Climatol.*, **46**, 634–650. https://doi.org/10.1175/JAM2489.1

Brandes, E.A., Ikeda, K., Thompson, G., Schönhuber, M., 2008. Aggregate terminal velocity/temperature relations. *J. Appl. Meteorol. Climatol.*, **47**, 2729–2736. https://doi.org/10.1175/2008JAMC1869.1

Brattich, E., Bracci, A., Zappi, A., Morozzi, P., Di Sabatino, S., Porcù, F., Di Nicola, F., Tositti, L., 2020. How to Get the Best from Low-Cost Particulate Matter Sensors: Guidelines and Practical Recommendations. *Sensors*, **20**, 3073. https://doi.org/10.3390/s20113073

Broadley, S.L., Murray, B.J., Herbert, R.J., Atkinson, J.D., Dobbie, S., Malkin, T.L., Condliffe, E., Neve, L., 2012. Immersion mode heterogeneous ice nucleation by an illite rich powder representative of atmospheric mineral dust. *Atmos. Chem. Phys.*, **12**, 287–307. https://doi.org/10.5194/acp-12-287-2012

Bromwich, D.H., 1988. Snowfall in high southern latitudes. *Rev. Geophys.*, **26**, 149. https://doi.org/10.1029/RG026i001p00149

Bromwich, D.H., Guo, Z., Bai, L., Chen, Q.S., 2004. Modeled Antarctic precipitation. Part I: Spatial and temporal variability. *J. Clim.*, **17**, 427–447. https://doi.org/10.1175/1520-0442(2004)017<0427:MAPPIS>2.0.CO;2

Calvo, A.I., Alves, C., Castro, A., Pont, V., Vicente, A.M., Fraile, R., 2013. Research on aerosol sources and chemical composition: Past, current and emerging issues. *Atmos. Res.*, **120**, 1–28. https://doi.org/10.1016/j.atmosres.2012.09.021

Capozzi, V., Montopoli, M., Bracci, A., Adirosi, E., Baldini, L., Vulpiani, G., Budillon, G., 2020. Retrieval of snow precipitation rate from polarimetric X-band radar measurements in Southern Italy Apennine mountains. *Atmos. Res.*, **236**, 104796. https://doi.org/10.1016/j.atmosres.2019.104796

Capozzi, V., Annella, C., Montopoli, M., Adirosi, E., Fusco, G., Budillon, G., 2021. Influence of wind-induced effects on laser disdrometer measurements: Analysis and compensation strategies. *Remote Sens.*, **13**. https://doi.org/10.3390/rs13153028

Castro, A., Alonso-Blanco, E., González-Colino, M., Calvo, A.I., Fernández-Raga, M., Fraile, R., 2010. Aerosol size distribution in precipitation events in León, Spain. *Atmos. Res.*, **96**, 421–435. https://doi.org/10.1016/j.atmosres.2010.01.014

Cavanagh, R.D., Melbourne-Thomas, J., Grant, S.M., Barnes, D.K.A., Hughes, K.A., Halfter, S., Meredith, M.P., Murphy, E.J., Trebilco, R., Hill, S.L., 2021. Future Risk for Southern Ocean Ecosystem Services Under Climate Change. *Front. Mar. Sci.*, **7**, 1224. https://doi.org/10.3389/fmars.2020.615214

Chandrasekar, V., Keränen, R., Lim, S., Moisseev, D., 2013. Recent advances in classification of observations from dual polarization weather radars. *Atmos. Res.*, **119**, 97–111. https://doi.org/10.1016/j.atmosres.2011.08.014

Chate, D.M., 2011. Below-thunderstorm rain scavenging of urban aerosols in the

health hazardous modes. *Nat. Hazards*, **56**, 81–91. https://doi.org/10.1007/s11069-010-9550-5

Chate, D.M., Murugavel, P., Ali, K., Tiwari, S., Beig, G., 2011. Below-cloud rain scavenging of atmospheric aerosols for aerosol deposition models. *Atmos. Res.*, **99**, 528–536. https://doi.org/10.1016/j.atmosres.2010.12.010

Chen, B., Yang, J., Pu, J., 2013. Statistical Characteristics of Raindrop Size Distribution in the Meiyu Season Observed in Eastern China. *J. Meteorol. Soc. Japan. Ser. II*, **91**, 215–227. https://doi.org/10.2151/jmsj.2013-208

Choudhary, S., Khare, N., 2022. Climate Change Over the Antarctic and the Southern Ocean and Its Impact and Bearing on the Global Climate System, in: *Assessing the Antarctic Environment from a Climate Change Perspective*. Springer, pp. 37–46.

Cogley, J.G., Arendt, A.A., Bauder, A., Braithwaite, R.J., Hock, R., Jansson, P., Kaser, G., Moller, M., Nicholson, L., Rasmussen, L.A., 2010. Glossary of glacier mass balance and related terms. UNESCO-IHP, Paris.

Crilley, L.R., Shaw, M., Pound, R., Kramer, L.J., Price, R., Young, S., Lewis, A.C., Pope, F.D., 2018. Evaluation of a low-cost optical particle counter (Alphasense OPC-N2) for ambient air monitoring. *Atmos. Meas. Tech.*, **11**, 709–720. https://doi.org/10.5194/amt-11-709-2018

Crilley, L.R., Singh, A., Kramer, L.J., Shaw, M.D., Alam, M.S., Apte, J.S., Bloss, W.J., Hildebrandt Ruiz, L., Fu, P., Fu, W., Gani, S., Gatari, M., Ilyinskaya, E., Lewis, A.C., Ng'ang'a, D., Sun, Y., Whitty, R.C.W., Yue, S., Young, S., Pope, F.D., 2020. Effect of aerosol composition on the performance of low-cost optical particle counter correction factors. *Atmos. Meas. Tech.*, **13**, 1181–1193. https://doi.org/10.5194/amt-13-1181-2020

Cristofanelli, P., Calzolari, F., Bonafè, U., Lanconelli, C., Lupi, A., Busetto, M., Vitale, V., Colombo, T., Bonasoni, P., 2011. Five-year analysis of background carbon dioxide and ozone variations during summer seasons at the Mario Zucchelli station (Antarctica). *Tellus, Ser. B Chem. Phys. Meteorol.*, **63**, 831–

842. https://doi.org/10.1111/j.1600-0889.2011.00576.x

Croce, P., Formichi, P., Landi, F., Mercogliano, P., Bucchignani, E., Dosio, A., Dimova, S., 2018. The snow load in Europe and the climate change. *Clim. Risk Manag.*, **20**, 138–154. https://doi.org/10.1016/j.crm.2018.03.001

Cugerone, K., De Michele, C., Ghezzi, A., Gianelle, V., 2018a. Aerosol removal due to precipitation and wind forcings in Milan urban area. *J. Hydrol.*, **556**, 1256–1262. https://doi.org/10.1016/j.jhydrol.2017.06.033

Cugerone, K., De Michele, C., Ghezzi, A., Gianelle, V., Gilardoni, S., 2018b. On the functional form of particle number size distributions: Influence of particle source and meteorological variables. *Atmos. Chem. Phys.*, **18**, 4831–4842. https://doi.org/10.5194/acp-18-4831-2018

DeConto, R.M., Pollard, D., 2016. Contribution of Antarctica to past and future sea-level rise. *Nature*, **531**, 591–597. https://doi.org/10.1038/nature17145

DeMott, P.J., Prenni, A.J., Liu, X., Kreidenweis, S.M., Petters, M.D., Twohy, C.H., Richardson, M.S., Eidhammer, T., Rogers, D.C., 2010. Predicting global atmospheric ice nuclei distributions and their impacts on climate. *Proc. Natl. Acad. Sci. U. S. A.*, **107**, 11217–11222. https://doi.org/10.1073/pnas.0910818107

Di Antonio, A., Popoola, O., Ouyang, B., Saffell, J., Jones, R., 2018. Developing a Relative Humidity Correction for Low-Cost Sensors Measuring Ambient Particulate Matter. *Sensors*, **18**, 2790. https://doi.org/10.3390/s18092790

Didenko, N.I., Cherenkov, V.I., 2018. Economic and geopolitical aspects of developing the Northern Sea Route, in: *IOP Conference Series: Earth and Environmental Science*. IOP Publishing, p. 12012.

Diémoz, H., Barnaba, F., Magri, T., Pession, G., Dionisi, D., Pittavino, S., Tombolato, I.K.F., Campanelli, M., Ceca, L.S. Della, Hervo, M., Di Liberto, L., Ferrero, L., Gobbi, G.P., 2019. Transport of Po Valley aerosol pollution to the northwestern Alps-Part 1: Phenomenology. *Atmos. Chem. Phys.*, **19**, 3065–3095. https://doi.org/10.5194/acp-19-3065-2019

Draine, B.T., Flatau, P.J., 1994. Discrete-Dipole Approximation For Scattering Calculations. *J. Opt. Soc. Am. A,* **11**, 1491. https://doi.org/10.1364/josaa.11.001491

Duhanyan, N., Roustan, Y., 2011. Below-cloud scavenging by rain of atmospheric gases and particulates. *Atmos. Environ.*, **45**, 7201–7217. https://doi.org/10.1016/j.atmosenv.2011.09.002

Durán-Alarcón, C., Boudevillain, B., Genthon, C., Grazioli, J., Souverijns, N., Van Lipzig, N.P.M., Gorodetskaya, I. V., Berne, A., 2019. The vertical structure of precipitation at two stations in East Antarctica derived from micro rain radars. *Cryosphere*, **13**, 247–264. https://doi.org/10.5194/tc-13-247-2019

Earle, M.E., Wong, K., Buisán, S., Nitu, R., Reverdin, A., Rasmussen, R., Roulet, Y.-A., Kontu, A., Landolt, S., 2016. Measuring solid precipitation using heated tipping bucket gauges: an overview of performance and recommendations from WMO-SPICE, in: *Proceedings Technical Conference (TECO) on Meteorological and Environmental Methods of Observation, TECO-2016–WMO, Madrid, Spain*. Agencia Estatal de Meteorología, Madrid, Spain, p. 8 pp.

Falconi, M.T., Von Lerber, A., Ori, D., Silvio Marzano, F., Moisseev, D., 2018. Snowfall retrieval at X, Ka and W bands: Consistency of backscattering and microphysical properties using BAECC ground-based measurements. *Atmos. Meas. Tech.*, **11**, 3059–3079. https://doi.org/10.5194/amt-11-3059-2018

Feng, J., 2009. A size-resolved model for below-cloud scavenging of aerosols by snowfall. *J. Geophys. Res.*, **114**, D08203. https://doi.org/10.1029/2008JD011012

Field, P.R., Heymsfield, A.J., 2015. Importance of snow to global precipitation. *Geophys. Res. Lett.*, **42**, 9512–9520. https://doi.org/10.1002/2015GL065497

Field, P.R., Lawson, R.P., Brown, P.R.A., Lloyd, G., Westbrook, C., Moisseev, D., Miltenberger, A., Nenes, A., Blyth, A., Choularton, T., Connolly, P., Buehl, J., Crosier, J., Cui, Z., Dearden, C., DeMott, P., Flossmann, A., Heymsfield,

A., Huang, Y., Kalesse, H., Kanji, Z.A., Korolev, A., Kirchgaessner, A., Lasher-Trapp, S., Leisner, T., McFarquhar, G., Phillips, V., Stith, J., Sullivan, S., 2016. Chapter 7. Secondary Ice Production - current state of the science and recommendations for the future. *Meteorol. Monogr.*, **58**, 1–7. https://doi.org/10.1175/amsmonographs-d-16-0014.1

French, H.M., Guglielmin, M., 2000. Frozen Ground Phenomena in the Vicinity of Terra Nova Bay, Northern Victoria land, Antarctica: A Preliminary Report. *Geogr. Ann. Ser. A Phys. Geogr.*, **82**, 513–526. https://doi.org/10.1111/j.0435-3676.2000.00138.x

Fretwell, P., Pritchard, H.D., Vaughan, D.G., Bamber, J.L., Barrand, N.E., Bell, R., Bianchi, C., Bingham, R.G., Blankenship, D.D., Casassa, G., Catania, G., Callens, D., Conway, H., Cook, A.J., Corr, H.F.J., Damaske, D., Damm, V., Ferraccioli, F., Forsberg, R., Fujita, S., Gim, Y., Gogineni, P., Griggs, J.A., Hindmarsh, R.C.A., Holmlund, P., Holt, J.W., Jacobel, R.W., Jenkins, A., Jokat, W., Jordan, T., King, E.C., Kohler, J., Krabill, W., Riger-Kusk, M., Langley, K.A., Leitchenkov, G., Leuschen, C., Luyendyk, B.P., Matsuoka, K., Mouginot, J., Nitsche, F.O., Nogi, Y., Nost, O.A., Popov, S. V., Rignot, E., Rippin, D.M., Rivera, A., Roberts, J., Ross, N., Siegert, M.J., Smith, A.M., Steinhage, D., Studinger, M., Sun, B., Tinto, B.K., Welch, B.C., Wilson, D., Young, D.A., Xiangbin, C., Zirizzotti, A., 2013. Bedmap2: Improved ice bed, surface and thickness datasets for Antarctica. *Cryosphere*, **7**, 375–393. https://doi.org/10.5194/tc-7-375-2013

Friedrich, K., Higgins, S., Masters, F.J., Lopez, C.R., 2013a. Articulating and stationary PARSIVEL disdrometer measurements in conditions with strong winds and heavy rainfall. *J. Atmos. Ocean. Technol.*, **30**, 2063–2080. https://doi.org/10.1175/JTECH-D-12-00254.1

Friedrich, K., Kalina, E.A., Masters, F.J., Lopez, C.R., 2013b. Drop-size distributions in thunderstorms measured by optical disdrometers during VORTEX2. *Mon. Weather Rev.*, **141**, 1182–1203. https://doi.org/10.1175/MWR-D-12-00116.1

Frölicher, T.L., Sarmiento, J.L., Paynter, D.J., Dunne, J.P., Krasting, J.P., Winton, M., 2015. Dominance of the Southern Ocean in Anthropogenic Carbon and Heat Uptake in CMIP5 Models. *J. Clim.*, **28**, 862–886. https://doi.org/10.1175/JCLI-D-14-00117.1

Fukuta, N., 1969. Experimental Studies on the Growth of Small Ice Crystals. *J. Atmos. Sci.*, **26**, 522–531. https://doi.org/10.1175/1520-0469(1969)026<0522:ESOTGO>2.0.CO;2

Genthon, C., Berne, A., Grazioli, J., Durán Alarcón, C., Praz, C., Boudevillain, B., 2018. Precipitation at Dumont d'Urville, Adélie Land, East Antarctica: The APRES3 field campaigns dataset. *Earth Syst. Sci. Data*, **10**, 1605–1612. https://doi.org/10.5194/essd-10-1605-2018

Gilbert, E., Kittel, C., 2021. Surface Melt and Runoff on Antarctic Ice Shelves at 1.5°C, 2°C, and 4°C of Future Warming. *Geophys. Res. Lett.*, **48**, e2020GL091733. https://doi.org/10.1029/2020GL091733

Gjermundsen, A., Nummelin, A., Olivié, D., Bentsen, M., Seland, Ø., Schulz, M., 2021. Shutdown of Southern Ocean convection controls long-term greenhouse gas-induced warming. *Nat. Geosci.*, **14**, 724–731. https://doi.org/10.1038/s41561-021-00825-x

Glickman, T.S., Zenk, W., 2000. Glossary of meteorology. AMS (American Meteorological Society).

Gorgucci, E., Baldini, L., 2015. Influence of Beam Broadening on the Accuracy of Radar Polarimetric Rainfall Estimation. *J. Hydrometeorol.*, **16**, 1356–1371. https://doi.org/10.1175/JHM-D-14-0084.1

Gorodetskaya, I. V., Tsukernik, M., Claes, K., Ralph, M.F., Neff, W.D., Van Lipzig, N.P.M., 2014. The role of atmospheric rivers in anomalous snow accumulation in East Antarctica. *Geophys. Res. Lett.*, **41**, 6199–6206. https://doi.org/10.1002/2014GL060881

Gorodetskaya, I. V., Kneifel, S., Maahn, M., Thiery, W., Schween, J.H., Mangold, A., Crewell, S., Van Lipzig, N.P.M., 2015. Cloud and precipitation properties

from ground-based remote-sensing instruments in East Antarctica. *Cryosphere*, **9**, 285–304. https://doi.org/10.5194/tc-9-285-2015

Grazioli, J., Genthon, C., Boudevillain, B., Duran-Alarcon, C., Del Guasta, M., Madeleine, J.B., Berne, A., 2017a. Measurements of precipitation in Dumont d'Urville, Adélie Land, East Antarctica. *Cryosphere*, **11**, 1797–1811. https://doi.org/10.5194/tc-11-1797-2017

Grazioli, J., Madeleine, J.B., Gallée, H., Forbes, R.M., Genthon, C., Krinner, G., Berne, A., 2017b. Katabatic winds diminish precipitation contribution to the Antarctic ice mass balance. *Proc. Natl. Acad. Sci. U. S. A.*, **114**, 10858–10863. https://doi.org/10.1073/pnas.1707633114

Gultepe, I., Heymsfield, A.J., Field, P.R., Axisa, D., 2017. Ice-Phase Precipitation. *Meteorol. Monogr.*, **58**, 6.1-6.36. https://doi.org/10.1175/AMSMONOGRAPHS-D-16-0013.1

Gunn, K.L.S., Marshall, J.S., 1958. the Distribution With Size of Aggregate Snowflakes. *J. Meteorol.*, **15**, 452–461. https://doi.org/10.1175/1520-0469(1958)015<0452:tdwsoa>2.0.co;2

Hampel, F.R., 1974. The Influence Curve and its Role in Robust Estimation. *J. Am. Stat. Assoc.*, **69**, 383–393. https://doi.org/10.1080/01621459.1974.10482962

Hansen, N., Langen, P.L., Boberg, F., Forsberg, R., Simonsen, S.B., Thejll, P., Vandecrux, B., Mottram, R., 2021. Downscaled surface mass balance in Antarctica: impacts of subsurface processes and large-scale atmospheric circulation. *Cryosphere*, **15**, 4315–4333. https://doi.org/10.5194/tc-15-4315-2021

Heymsfield, A., DeMott, P., 2010. The Ice in Clouds Experiment-Tropical Field Campaign-(ICE-T)-Research Plan-Feb, 2010 [WWW Document]. URL https://www.eol.ucar.edu/system/files/SOD_ICE-T_march2.pdf

Heymsfield, A.J., Lewis, S., Bansemer, A., Iaquinta, J., Miloshevich, L.M., Kajikawa, M., Twohy, C., Poellot, M.R., 2002. A general approach for deriving the properties of cirrus and stratiform ice cloud particles. *J. Atmos.*

Sci., **59**, 3–29. https://doi.org/10.1175/1520-0469(2002)059<0003:AGAFDT>2.0.CO;2

Heymsfield, A.J., Bansemer, A., Schmitt, C., Twohy, C., Poellot, M.R., 2004. Effective Ice Particle Densities Derived from Aircraft Data. *J. Atmos. Sci.*, **61**, 982–1003. https://doi.org/10.1175/1520-0469(2004)061<0982:EIPDDF>2.0.CO;2

Heymsfield, A.J., Schmitt, C., Chen, C.-C.-J., Bansemer, A., Gettelman, A., Field, P.R., Liu, C., 2020. Contributions of the Liquid and Ice Phases to Global Surface Precipitation: Observations and Global Climate Modeling. *J. Atmos. Sci.*, **77**, 2629–2648. https://doi.org/10.1175/JAS-D-19-0352.1

Hillamo, R., Allegrini, I., Sparapani, R., Kerminen, V.M., 1998. Mass size distributions and precursor gas concentrations of major inorganic ions in Antarctic aerosol. *Int. J. Environ. Anal. Chem.*, **71**, 353–372. https://doi.org/10.1080/03067319808032638

Hobbs, P.V., 2000. Introduction to atmospheric chemistry. Cambridge University Press.

Holroyd, E.W., 1971. The meso- and microscale structure of Great Lakes snowstorm bands: a synthesis of ground measurements, radar data, and satellite observations. State University of New York at Albany, Department of Atmospheric Science: Albany, NY, USA.

Honeyager, R., Liu, G., Nowell, H., 2016. Voronoi diagram-based spheroid model for microwave scattering of complex snow aggregates. *J. Quant. Spectrosc. Radiat. Transf.*, **170**, 28–44. https://doi.org/10.1016/j.jqsrt.2015.10.025

Hong, Y., Du, Y., Xia, X., Xu, L., Zhang, Y., Xie, S.P., 2021. Subantarctic mode water and its long-Term change in cmip6 models. *J. Clim.*, **34**, 9385–9400. https://doi.org/10.1175/JCLI-D-21-0133.1

Huang, G., Bringi, V.N., Moisseev, D., Petersen, W.A., Bliven, L., Hudak, D., 2015. Use of 2D-video disdrometer to derive mean density – size and Ze – SR relations : Four snow cases from the light precipitation validation experiment.

Atmos. Res., **153**, 34–48. https://doi.org/10.1016/j.atmosres.2014.07.013

Huang, G.J., Bringi, V.N., Cifelli, R., Hudak, D., Petersen, W.A., 2010. A methodology to derive radar reflectivity-liquid equivalent snow rate relations using C-band radar and a 2D video disdrometer. *J. Atmos. Ocean. Technol.*, **27**, 637–651. https://doi.org/10.1175/2009JTECHA1284.1

Illuminati, S., Bau, S., Annibaldi, A., Mantini, C., Libani, G., Truzzi, C., Scarponi, G., 2016. Evolution of size-segregated aerosol mass concentration during the Antarctic summer at Northern Foothills , Victoria Land. *Atmos. Environ.*, **125**, 212–221. https://doi.org/10.1016/j.atmosenv.2015.11.015

Illuminati, S., Annibaldi, A., Bau, S., Scarchilli, C., Ciardini, V., Grigioni, P., Girolametti, F., Vagnoni, F., Scarponi, G., Truzzi, C., 2020. Seasonal Evolution of Size-Segregated Particulate Mercury in the Atmospheric Aerosol over Terra Nova Bay, Antarctica. *Molecules*, **25**. https://doi.org/10.3390/molecules25173971

IPCC, 2007. Climate Change 2007 Synthesis Report, Intergovernmental Panel on Climate Change Core Writing Team IPCC. Geneva, Switzerland.

IPCC, 2021. Climate Change 2021: The Physical Science Basis. Contribution of Working Group I to the Sixth Assessment Report of the Intergovernmental Panel on Climate Change. Geneva, Switzerland.

Jaenicke, R., 1972. The optical particle counter: Cross-sensitivity and coincidence. *J. Aerosol Sci.*, **3**, 95–111. https://doi.org/10.1016/0021-8502(72)90147-4

Jia, R., Chen, M., Pan, H., Zeng, J., Zhu, J., Liu, X., Zheng, M., Qiu, Y., 2022. Freshwater components track the export of dense shelf water from Prydz Bay, Antarctica. *Deep Sea Res. Part II Top. Stud. Oceanogr.*, 105023. https://doi.org/10.1016/j.dsr2.2022.105023

Jiang, H., Yin, Y., Yang, L., Yang, S., Su, H., Chen, K., 2014. The characteristics of atmospheric ice nuclei measured at different altitudes in the Huangshan Mountains in Southeast China. *Adv. Atmos. Sci.*, **31**, 396–406. https://doi.org/10.1007/s00376-013-3048-5

Johnson, K.K., Bergin, M.H., Russell, A.G., Hagler, G.S.W., 2018. Field test of several low-cost particulate matter sensors in high and low concentration urban environments. *Aerosol Air Qual. Res.*, **18**, 565–578. https://doi.org/10.4209/aaqr.2017.10.0418

Johnston, S., 2009. Climate change policies in the polar regions: Trade offs from an international policy laboratory, in: *IOP Conference Series. Earth and Environmental Science*. IOP Publishing.

Joy-Warren, H.L., 2021. Phytoplankton Photoacclimation in the Southern Ocean and Arctic Ocean. Stanford University.

Jung, C.H., Um, J., Shin, Y.H., Lee, S.S., Lee, Y.G., Bae, S.Y., Kim, Y.P., 2015. Minimum collection efficiency diameter during snow scavenging process. *Part. Sci. Technol.*, **33**, 321–330. https://doi.org/10.1080/02726351.2014.970311

Karagulian, F., Barbiere, M., Kotsev, A., Spinelle, L., Gerboles, M., Lagler, F., Redon, N., Crunaire, S., Borowiak, A., 2019. Review of the performance of low-cost sensors for air quality monitoring. *Atmosphere (Basel).*, **10**, 506. https://doi.org/10.3390/atmos10090506

Keat, W.J., Westbrook, C.D., 2017. Revealing Layers of Pristine Oriented Crystals Embedded Within Deep Ice Clouds Using Differential Reflectivity and the Copolar Correlation Coefficient. *J. Geophys. Res. Atmos.*, **122**, 11,737-11,759. https://doi.org/10.1002/2017JD026754

Khatiwala, S., Primeau, F., Hall, T., 2009. Reconstruction of the history of anthropogenic CO2 concentrations in the ocean. *Nature*, **462**, 346–349. https://doi.org/10.1038/nature08526

Kim, B.H., Seo, K.W., Eom, J., Chen, J., Wilson, C.R., 2020. Antarctic ice mass variations from 1979 to 2017 driven by anomalous precipitation accumulation. *Sci. Rep.*, **10**, 1–9. https://doi.org/10.1038/s41598-020-77403-5

Kittel, C., Amory, C., Agosta, C., Delhasse, A., Doutreloup, S., Huot, P.V., Wyard, C., Fichefet, T., Fettweis, X., 2018. Sensitivity of the current Antarctic surface

mass balance to sea surface conditions using MAR. *Cryosphere*, **12**, 3827–3839. https://doi.org/10.5194/tc-12-3827-2018

Kittel, C., Amory, C., Agosta, C., Jourdain, N.C., Hofer, S., Delhasse, A., Doutreloup, S., Huot, P.V., Lang, C., Fichefet, T., Fettweis, X., 2021. Diverging future surface mass balance between the Antarctic ice shelves and grounded ice sheet. *Cryosphere*, **15**, 1215–1236. https://doi.org/10.5194/tc-15-1215-2021

Knuth, S.L., Tripoli, G.J., Thom, J.E., Weidner, G.A., 2010. The Influence of Blowing Snow and Precipitation on Snow Depth Change across the Ross Ice Shelf and Ross Sea Regions of Antarctica. *J. Appl. Meteorol. Climatol.*, **49**, 1306–1321. https://doi.org/10.1175/2010JAMC2245.1

Kochendorfer, J., Earle, M.E., Hodyss, D., Reverdin, A., Roulet, Y.-A., Nitu, R., Rasmussen, R., Landolt, S., Buisán, S., Laine, T., 2020. Undercatch Adjustments for Tipping-Bucket Gauge Measurements of Solid Precipitation. *J. Hydrometeorol.*, **21**, 1193–1205. https://doi.org/10.1175/JHM-D-19-0256.1

Kuo, K. Sen, Olson, W.S., Johnson, B.T., Grecu, M., Tian, L., Clune, T.L., Van Aartsen, B.H., Heymsfield, A.J., Liao, L., Meneghini, R., 2016. Full access the microwave radiative properties of falling snow derived from nonspherical ice particle models. Part I: An extensive database of simulated pristine crystals and aggregate particles, and their scattering properties. *J. Appl. Meteorol. Climatol.*, **55**, 691–708. https://doi.org/10.1175/JAMC-D-15-0130.1

Kuula, J., Mäkelä, T., Aurela, M., Teinilä, K., Varjonen, S., González, Ó., Timonen, H., 2020. Laboratory evaluation of particle-size selectivity of optical low-cost particulate matter sensors. *Atmos. Meas. Tech.*, **13**, 2413–2423. https://doi.org/10.5194/amt-13-2413-2020

Kyrö, E.M., Grönholm, T., Vuollekoski, H., Virkkula, A., Kulmala, M., Laakso, L., 2009. Snow scavenging of ultrafine particles: Field measurements and parameterization. *Boreal Environ. Res.*, **14**, 527–538.

Laakso, L., Grönholm, T., Rannik, Ü., Kosmale, M., Fiedler, V., Vehkamäki, H.,

Kulmala, M., 2003. Ultrafine particle scavenging coefficients calculated from 6 years field measurements. *Atmos. Environ.*, **37**, 3605–3613. https://doi.org/10.1016/S1352-2310(03)00326-1

Lachlan-Cope, T., 2010. Antarctic clouds. *Polar Res.*, **29**, 150–158. https://doi.org/10.1111/j.1751-8369.2010.00148.x

Lanza, L.G., Vuerich, E., 2009. The WMO Field Intercomparison of Rain Intensity Gauges. *Atmos. Res.*, **94**, 534–543. https://doi.org/10.1016/j.atmosres.2009.06.012

Lau, K.M., Wu, H.T., 2003. Warm rain processes over tropical oceans and climate implications. *Geophys. Res. Lett.*, **30**. https://doi.org/10.1029/2003GL018567

Lawson, R.P., Baker, B.A., Zmarzly, P., O'Connor, D., Mo, Q., Gayet, J.F., Shcherbakov, V., 2006. Microphysical and optical properties of atmospheric ice crystals at South Pole station. *J. Appl. Meteorol. Climatol.*, **45**, 1505–1524. https://doi.org/10.1175/JAM2421.1

Legrand, M., Wolff, E., Wagenbach, D., 1999. Antarctic aerosol and snowfall chemistry: Implications for deep Antarctic ice-core chemistry. *Ann. Glaciol.*, **29**, 66–72. https://doi.org/10.3189/172756499781821094

Leinonen, J., Szyrmer, W., 2015. Radar signatures of snowflake riming: A modeling study. *Earth Sp. Sci.*, **2**, 346–358. https://doi.org/10.1002/2015EA000102

Levizzani, V., Kidd, C., Kirschbaum, D.B., Kummerow, C.D., Nakamura, K., Turk, F.J. (Eds), 2020. Satellite Precipitation Measurement, Advances in Global Change Research. Springer International Publishing, Cham, Switzerland. https://doi.org/10.1007/978-3-030-24568-9

Li, H., Tiira, J., von Lerber, A., Moisseev, D., 2020. Towards the connection between snow microphysics and melting layer: insights from multifrequency and dual-polarization radar observations during BAECC. *Atmos. Chem. Phys.*. **20**, 9547–9562. https://doi.org/10.5194/acp-20-9547-2020

Li, X., Dong, Y., Dong, Z., Du, C., Chen, C., 2016. Observed changes in aerosol

physical and optical properties before and after precipitation events. *Adv. Atmos. Sci.*, **33**, 931–944. https://doi.org/10.1007/s00376-016-5178-z

Li, X., Cai, W., Meehl, G.A., Chen, D., Yuan, X., Raphael, M., Holland, D.M., Ding, Q., Fogt, R.L., Markle, B.R., Wang, G., Bromwich, D.H., Turner, J., Xie, S.P., Steig, E.J., Gille, S.T., Xiao, C., Wu, B., Lazzara, M.A., Chen, X., Stammerjohn, S., Holland, P.R., Holland, M.M., Cheng, X., Price, S.F., Wang, Z., Bitz, C.M., Shi, J., Gerber, E.P., Liang, X., Goosse, H., Yoo, C., Ding, M., Geng, L., Xin, M., Li, C., Dou, T., Liu, C., Sun, W., Wang, X., Song, C., 2021. Tropical teleconnection impacts on Antarctic climate changes. *Nat. Rev. Earth Environ.*, **2**, 680–698. https://doi.org/10.1038/s43017-021-00204-5

Libbrecht, K.G., 2005. The physics of snow crystals. *Reports Prog. Phys.*, **68**, 855–895. https://doi.org/10.1088/0034-4885/68/4/R03

Libbrecht, K.G., 2011. Snow crystal structure, in: Singh, V.P., Singh, P., Haritashya, U.K. (Eds.), *Encyclopedia of Earth Sciences Series*. Springer Netherlands, Dordrecht, pp. 1038–1041. https://doi.org/10.1007/978-90-481-2642-2_662

Liou, K.-N., Yang, P., 2016. Light Scattering by Ice Crystals. Cambridge University Press, Cambridge, UK. https://doi.org/10.1017/CBO9781139030052

Liu, B.Y.H., Berglund, R.N., Agarwal, J.K., 1974. Experimental studies of optical particle counters. *Atmos. Environ.*, **8**, 717–732.

Liu, G., 2008. A database of microwave single-scattering properties for nonspherical ice particles. *Bull. Am. Meteorol. Soc.*, **89**, 1563–1570. https://doi.org/10.1175/2008BAMS2486.1

Liu, H., Shah, S., Jiang, W., 2004. On-line outlier detection and data cleaning. *Comput. Chem. Eng.*, **28**, 1635–1647. https://doi.org/10.1016/j.compchemeng.2004.01.009

Locatelli, J.D., Hobbs, P. V., 1974. Fall speeds and masses of solid precipitation particles. *J. Geophys. Res.*, **79**, 2185–2197.

https://doi.org/10.1029/JC079i015p02185

Loeb, N.G., Su, W., 2010. Direct aerosol radiative forcing uncertainty based on a radiative perturbation analysis. *J. Clim.*, **23**, 5288–5293. https://doi.org/10.1175/2010JCLI3543.1

Löffler-Mang, M., Joss, J., 2000. An optical disdrometer for measuring size and velocity of hydrometeors. *J. Atmos. Ocean. Technol.*, **17**, 130–139. https://doi.org/10.1175/1520-0426(2000)017<0130:AODFMS>2.0.CO;2

Löffler-Mang, M., Blahak, U., 2001. Estimation of the equivalent radar reflectivity factor from measured snow size spectra. *J. Appl. Meteorol.*, **40**, 843–849. https://doi.org/10.1175/1520-0450(2001)040<0843:EOTERR>2.0.CO;2

Lu, Y., Jiang, Z., Aydin, K., Verlinde, J., Clothiaux, E., Botta, G., 2016. A polarimetric scattering database for non-spherical ice particles at microwave wavelengths. *Atmos. Meas. Tech.*, **9**, 5119–5134. https://doi.org/10.5194/amt-9-5119-2016

Luan, T., Guo, X., Zhang, T., Guo, L., 2019. Below-Cloud Aerosol Scavenging by Different-Intensity Rains in Beijing City. *J. Meteorol. Res.*, **33**, 126–137. https://doi.org/10.1007/s13351-019-8079-0

Luke, E.P., Yang, F., Kollias, P., Vogelmann, A.M., Maahn, M., 2021. New insights into ice multiplication using remote-sensing observations of slightly supercooled mixed-phase clouds in the Arctic. *Proc. Natl. Acad. Sci.*, **118**, e2021387118. https://doi.org/10.1073/pnas.2021387118

Maahn, M., Kollias, P., 2012. Improved Micro Rain Radar snow measurements using Doppler spectra post-processing. *Atmos. Meas. Tech.*, **5**, 2661–2673. https://doi.org/10.5194/amt-5-2661-2012

Magono, C., 1960. Structure of snowfall revealed by geographic distribution of snow crystals. *Phys. Precipitation, Am. Geophys. Union*, 142–151.

Magono, C., Lee, C.W., 1966. Meteorological classification of natural snow crystals. *J. Fac. Sci. Hokkaido Univ. Ser. 7, Geophys.*, **2**, 321–335.

Mamali, D., Marinou, E., Sciare, J., Pikridas, M., Kokkalis, P., Kottas, M., Binietoglou, I., Tsekeri, A., Keleshis, C., Engelmann, R., Baars, H., Ansmann, A., Amiridis, V., Russchenberg, H., Biskos, G., 2018. Vertical profiles of aerosol mass concentration derived by unmanned airborne in situ and remote sensing instruments during dust events. *Atmos. Meas. Tech.*, **11**, 2897–2910. https://doi.org/10.5194/amt-11-2897-2018

Marshall, J., Speer, K., 2012. Closure of the meridional overturning circulation through Southern Ocean upwelling. *Nat. Geosci.*, **5**, 171–180. https://doi.org/10.1038/ngeo1391

Marshall, J.S., Palmer, W.M.K., 1948. the Distribution of Raindrops With Size. *J. Meteorol.*, **5**, 165–166. https://doi.org/10.1175/1520-0469(1948)005<0165:tdorws>2.0.co;2

Masic, A., Bibic, D., Pikula, B., Blazevic, A., Huremovic, J., Zero, S., 2020. Evaluation of optical particulate matter sensors under realistic conditions of strong and mild urban pollution. *Atmos. Meas. Tech.*, **13**, 6427–6443. https://doi.org/10.5194/amt-13-6427-2020

Matrosov, S.Y., 2007. Modeling backscatter properties of snowfall at millimeter wavelengths. *J. Atmos. Sci.*, **64**, 1727–1736. https://doi.org/10.1175/JAS3904.1

Matrosov, S.Y., Campbell, C., Kingsmill, D., Sukovich, E., 2009. Assessing snowfall rates from X-Band radar reflectivity measurements. *J. Atmos. Ocean. Technol.*, **26**, 2324–2339. https://doi.org/10.1175/2009JTECHA1238.1

Mayewski, P.A., Meredith, M.P., Summerhayes, C.P., Turner, J., Worby, A., Barrett, P.J., Casassa, G., Bertler, N.A.N., Bracegirdle, T., Naveira Garabato, A.C., Bromwich, D., Campbell, H., Hamilton, G.S., Lyons, W.B., Maasch, K.A., Aoki, S., Xiao, C., Van Ommen, T., 2009. State of the antarctic and southern ocean climate system. *Rev. Geophys.*, **47**, 1–38. https://doi.org/10.1029/2007RG000231

McGee, J., Edmiston, D., Haward, M., 2022. Antarctic Geopolitics: Background,

in: *The Future of Antarctica*. Springer, pp. 83–103. https://doi.org/10.1007/978-981-16-7095-4_5

Milani, L., Kulie, M.S., Casella, D., Dietrich, S., L'Ecuyer, T.S., Panegrossi, G., Porcù, F., Sanò, P., Wood, N.B., 2018. CloudSat snowfall estimates over Antarctica and the Southern Ocean: An assessment of independent retrieval methodologies and multi-year snowfall analysis. *Atmos. Res.*, **213**, 121–135. https://doi.org/10.1016/j.atmosres.2018.05.015

Mitchell, D.L., Zhang, R., Pitter, R.L., 1990. Mass-Dimensional Relationships for Ice Particles and the Influence of Riming on Snowfall Rates. *J. Appl. Meteorol.*, **29**, 153–163. https://doi.org/10.1175/1520-0450(1990)029<0153:MDRFIP>2.0.CO;2

Mitchell, D.L., 1996. Use of Mass- and Area-Dimensional Power Laws for Determining Precipitation Particle Terminal Velocities. *J. Atmos. Sci.*, **53**, 1710–1723. https://doi.org/10.1175/1520-0469(1996)053<1710:UOMAAD>2.0.CO;2

Moisseev, D.N., Lautaportti, S., Tyynela, J., Lim, S., 2015. Dual-polarization radar signatures in snowstorms: Role of snowflake aggregation. *J. Geophys. Res.*, **120**, 12,644-12,665. https://doi.org/10.1002/2015JD023884

Molthan, A.L., Colle, B.A., Yuter, S.E., Stark, D., 2016. Comparisons of modeled and observed reflectivities and fall speeds for snowfall of varied riming degrees during winter storms on long Island, New York. *Mon. Weather Rev.*, **144**, 4327–4347. https://doi.org/10.1175/MWR-D-15-0397.1

Mottram, R., Hansen, N., Kittel, C., Van Wessem, J.M., Agosta, C., Amory, C., Boberg, F., Van De Berg, W.J., Fettweis, X., Gossart, A., Van Lipzig, N.P.M., Van Meijgaard, E., Orr, A., Phillips, T., Webster, S., Simonsen, S.B., Souverijns, N., 2021. What is the surface mass balance of Antarctica? An intercomparison of regional climate model estimates, *Cryosphere.*, https://doi.org/10.5194/tc-15-3751-2021

Muramoto, K.-I., Matsuura, K., Shiina, T., 1995. Measuring the density of snow

particles and snowfall rate. *Electron. Commun. Japan Part III Fundam. Electron. Sci.*, **78**, 71–79. https://doi.org/10.1002/ecjc.4430781107

Murray, B.J., Broadley, S.L., Wilson, T.W., Atkinson, J.D., Wills, R.H., 2011. Heterogeneous freezing of water droplets containing kaolinite particles. *Atmos. Chem. Phys.*, **11**, 4191–4207. https://doi.org/10.5194/acp-11-4191-2011

Naaim-Bouvet, F., Bellot, H., Nishimura, K., Genthon, C., Palerme, C., Guyomarc'h, G., Vionnet, V., 2014. Detection of snowfall occurrence during blowing snow events using photoelectric sensors. *Cold Reg. Sci. Technol.*, **106–107**, 11–21. https://doi.org/10.1016/j.coldregions.2014.05.005

Nešpor, V., Krajewski, W.F., Kruger, A., 2000. Wind-induced error of raindrop size distribution measurement using a two-dimensional video disdrometer. J. *Atmos. Ocean. Technol.*, **17**, 1483–1492. https://doi.org/10.1175/1520-0426(2000)017<1483:WIEORS>2.0.CO;2

Nitu, R., Roulet, Y.-A., Wolff, M., Earle, M.E., Reverdin, A., Smith, C.D., Kochendorfer, J., Morin, S., Rasmussen, R., Wong, K., 2019. WMO Solid Precipitation Intercomparison Experiment (SPICE)(2012-2015). World Meteorological Organization, Geneva, Switzerland.

Nowell, H., Liu, G., Honeyager, R., 2013. Modeling the microwave single-scattering properties of aggregate snowflakes. *J. Geophys. Res. Atmos.*, **118**, 7873–7885. https://doi.org/10.1002/jgrd.50620

Ori, D., Maestri, T., Rizzi, R., Cimini, D., Montopoli, M., Marzano, F.S., 2014. Scattering properties of modeled complex snowflakes and mixed-phase particles at microwave and millimeter frequencies. *J. Geophys. Res. Atmos.*, **119**, 9931–9947. https://doi.org/10.1002/2014JD021616

Pal, S., Lee, T.R., Phelps, S., De Wekker, S.F.J., 2014. Impact of atmospheric boundary layer depth variability and wind reversal on the diurnal variability of aerosol concentration at a valley site. *Sci. Total Environ.*, **496**, 424–434. https://doi.org/10.1016/j.scitotenv.2014.07.067

Palerme, C., Kay, J.E., Genthon, C., L'Ecuyer, T., Wood, N.B., Claud, C., 2014. How much snow falls on the Antarctic ice sheet? *Cryosphere*, **8**, 1577–1587. https://doi.org/10.5194/tc-8-1577-2014

Pan, X.L., Li, B.F., Watanabe, Y.W., 2022. Intense ocean freshening from melting glacier around the Antarctica during early twenty-first century. *Sci. Rep.*, **12**, 383. https://doi.org/10.1038/s41598-021-04231-6

Paramonov, M., Grönholm, T., Virkkula, A., 2011. Below-cloud scavenging of aerosol particles by snow at an urban site in Finland. *Boreal Environ. Res.*, **16**, 304–320.

Patade, S., Nagare, B., Wagh, S., Maheskumar, R.S., Prabha, T. V., Pradeep Kumar, P., 2014. Deposition ice nuclei observations over the Indian region during CAIPEEX. *Atmos. Res.*, **149**, 300–314. https://doi.org/10.1016/j.atmosres.2014.07.001

Peters, G., Fischer, B., Andersson, T., 2002. Rain observations with a vertically looking Micro Rain Radar (MRR). *Boreal Environ. Res.*, **7**, 353–362.

Pfitzenmaier, L., Unal, C.M.H., Dufournet, Y., Russchenberg, H.W.J., 2018. Observing ice particle growth along fall streaks in mixed-phase clouds using spectral polarimetric radar data. *Atmos. Chem. Phys.*, **18**, 7843–7862. https://doi.org/10.5194/acp-18-7843-2018

Praz, C., Roulet, Y.A., Berne, A., 2017. Solid hydrometeor classification and riming degree estimation from pictures collected with a Multi-Angle Snowflake Camera. *Atmos. Meas. Tech.*, **10**, 1335–1357. https://doi.org/10.5194/amt-10-1335-2017

Previdi, M., Polvani, L.M., 2016. Anthropogenic impact on Antarctic surface mass balance, currently masked by natural variability, to emerge by mid-century. *Environ. Res. Lett.*, **11**, 94001. https://doi.org/10.1088/1748-9326/11/9/094001

Pruppacher, H.R., Klett, J.D., 2010. Microphysics of Clouds and Precipitation, Atmospheric and Oceanographic Sciences Library. Springer Netherlands,

Dordrecht. https://doi.org/10.1007/978-0-306-48100-0

Ranasinghe, R., Ruane, A.C., Vautard, R., Arnell, N., Coppola, E., Cruz, F.A., Dessai, S., Islam, A.S., Rahimi, M., Ruiz Carrascal, D., Sillmann, J., Sylla, M.B., Tebaldi, C., Wang, W., Zaaboul, R., 2021. Climate Change Information for Regional Impact and for Risk Assessment. In Climate Change 2021: The Physical Science Basis. Contribution of Working Group I to the Sixth Assessment Report of the Intergovernmental Panel on Climate Change.

Rasmussen, R., Dixon, M., Vasiloff, S., Hage, F., Knight, S., Vivekanandan, J., Xu, M., 2003. Snow nowcasting using a real-time correlation of radar reflectivity with snow gauge accumulation. *J. Appl. Meteorol.*, **42**, 20–36. https://doi.org/10.1175/1520-0450(2003)042<0020:SNUART>2.0.CO;2

Rasmussen, R., Baker, B., Kochendorfer, J., Meyers, T., Landolt, S., Fischer, A.P., Black, J., Thériault, J.M., Kucera, P., Gochis, D., Smith, C., Nitu, R., Hall, M., Ikeda, K., Gutmann, E., 2012. How well are we measuring snow: The NOAA/FAA/NCAR winter precipitation test bed. *Bull. Am. Meteorol. Soc.*, **93**, 811–829. https://doi.org/10.1175/BAMS-D-11-00052.1

Rasmussen, R.M., Hallett, J., Purcell, R., Cole, J., Tryhane, M., 2002. The hot plate snow gauge, in: Amer. Meteor. Soc. (Ed.), *Preprints, 11th Conference on Cloud Physics*. Odgen,UT,USA.

Renard, J.B., Thaury, C., Mineau, J.L., Gaubicher, B., 2010. Small-angle light scattering by airborne particulates: Environnement S.A. continuous particulate monitor. *Meas. Sci. Technol.*, **21**, 85901. https://doi.org/10.1088/0957-0233/21/8/085901

Rha, D.-K., In, H.-J., Choi, E.-J., Kim, H.-L., Lee, J.-E., Lee, G.-W., 2014. WMO Solid Precipitation Intercomparison Experiment (SPICE): Overview and results of Gochang site. [WWW Document]. URL https://library.wmo.int/pmb_ged/iom_116_en/Session 3/P3_20_Rha_SPICE_site_Korea.pdf (accessed 12.22.21).

Rignot, E., Mouginot, J., Scheuchl, B., Van Den Broeke, M., Van Wessem, M.J.,

Morlighem, M., 2019. Four decades of Antarctic ice sheet mass balance from 1979–2017. *Proc. Natl. Acad. Sci. U. S. A.*, **116**, 1095–1103. https://doi.org/10.1073/pnas.1812883116

Rome, E., Bogen, M., Lückerath, D., Ullrich, O., Worst, R., Streberová, E., Dumonteil, M., Mendizabal, M., Abajo, B., Feliu, E., Bosch, P., Connelly, A., Carter, J., 2019. Risk-based analysis of the vulnerability of urban infrastructure to the consequences of climate change, in: *Advanced Sciences and Technologies for Security Applications*. Springer, Berlin/Heidelberg, Germany, pp. 55–75. https://doi.org/10.1007/978-3-030-00024-0_4

Santachiara, G., Belosi, F., Prodi, F., 2014. The mystery of ice crystal multiplication in a laboratory experiment. *J. Atmos. Sci.*, **71**, 89–97. https://doi.org/10.1175/JAS-D-13-0117.1

Sarmiento, J.L., Gruber, N., Brzezinski, M.A., Dunne, J.P., 2004. High-latitude controls of thermocline nutrients and low latitude biological productivity. *Nature*, **427**, 56–60. https://doi.org/10.1038/nature02127

Savina, M., Schäppi, B., Molnar, P., Burlando, P., Sevruk, B., 2012. Comparison of a tipping-bucket and electronic weighing precipitation gage for snowfall. *Rainfall Urban Context Forecast. Risk Clim. Chang.*, **103**, 45–51. https://doi.org/10.1016/j.atmosres.2011.06.010

Saxena, V.K., Weintraub, D.C., 1988. Ice forming nuclei concentrations at Palmer Station, Antarctica, in: *Atmospheric Aerosols and Nucleation*. Springer, pp. 679–682.

Sayahi, T., Butterfield, A., Kelly, K.E., 2019. Long-term field evaluation of the Plantower PMS low-cost particulate matter sensors. *Environ. Pollut.*, **245**, 932–940. https://doi.org/10.1016/j.envpol.2018.11.065

Scarchilli, C., Frezzotti, M., Grigioni, P., De Silvestri, L., Agnoletto, L., Dolci, S., 2010. Extraordinary blowing snow transport events in East Antarctica. *Clim. Dyn.*, **34**, 1195–1206. https://doi.org/10.1007/s00382-009-0601-0

Scarchilli, C., Frezzotti, M., Ruti, P.M., 2011. Snow precipitation at four ice core

sites in East Antarctica: Provenance, seasonality and blocking factors. *Clim. Dyn.*, **37**, 2107–2125. https://doi.org/10.1007/s00382-010-0946-4

Scarchilli, C., Ciardini, V., Grigioni, P., Iaccarino, A., De Silvestri, L., Baldini, L., Roberto, N., Argentini, S., Bracci, A., Frezzotti, M., 2020. Characterization of snowfall estimated by in situ and ground-based remote-sensing observations at Terra Nova Bay, Victoria Land, Antarctica. *J. Glaciol.*, **66**, 1006–1023. https://doi.org/10.1017/jog.2020.70

Schirle, C.E., Cooper, S.J., Wolff, M.A., Pettersen, C., Wood, N.B., L'ecuyer, T.S., Ilmo, T., Nygård, K., 2019. Estimation of snowfall properties at a mountainous site in Norway using combined radar and in situ microphysical observations. *J. Appl. Meteorol. Climatol.*, **58**, 1337–1352. https://doi.org/10.1175/JAMC-D-18-0281.1

Schlenczek, O., Fugal, J.P., Lloyd, G., Bower, K.N., Choularton, T.W., Flynn, M., Crosier, J., Borrmann, S., 2017. Microphysical Properties of Ice Crystal Precipitation and Surface-Generated Ice Crystals in a High Alpine Environment in Switzerland. *J. Appl. Meteorol. Climatol.*, **56**, 433–453. https://doi.org/10.1175/JAMC-D-16-0060.1

Schneebeli, M., Dawes, N., Lehning, M., Berne, A., 2013. High-resolution vertical profiles of X-band polarimetric radar observables during snowfall in the Swiss Alps. *J. Appl. Meteorol. Climatol.*, **52**, 378–394. https://doi.org/10.1175/JAMC-D-12-015.1

Schoger, S.Y., Moisseev, D., von Lerber, A., Crewell, S., Ebell, K., 2021. Snowfall-Rate Retrieval for K- and W-Band Radar Measurements Designed in Hyytiälä, Finland, and Tested at Ny-Ålesund, Svalbard, Norway. *J. Appl. Meteorol. Climatol.*, **60**, 273–289. https://doi.org/10.1175/JAMC-D-20-0095.1

Seefeldt, M.W., Low, T.M., Landolt, S.D., Nylen, T.H., 2021. Remote and autonomous measurements of precipitation for the northwestern Ross Ice Shelf, Antarctica. *Earth Syst. Sci. Data*, **13**, 5803–5817. https://doi.org/10.5194/essd-13-5803-2021

Seigneur, C., 2019. Air Pollution: Concepts, Theory, and Applications. Cambridge University Press.

Seinfeld, J., Pandis, S., 2008. Atmospheric Chemistry and Physics, New York.

Shepherd, A., Ivins, E., Rignot, E., Smith, B., Broeke, V.D.M., Velicogna, I., Wouters, B., 2018. Mass balance of the Antarctic Ice Sheet from 1992 to 2017. *Nature*, **558**, 219–222. https://doi.org/10.1017/cbo9780511535659.014

Shepherd, A., Ivins, E., Rignot, E., Smith, B., Van Den Broeke, M., Velicogna, I., Whitehouse, P., Briggs, K., Joughin, I., Krinner, G., 2020. Mass balance of the Greenland Ice Sheet from 1992 to 2018. *Nature*, **579**, 233–239. https://doi.org/10.1038/s41586-019-1855-2

Smith, B., Fricker, H.A., Gardner, A.S., Medley, B., Nilsson, J., Paolo, F.S., Holschuh, N., Adusumilli, S., Brunt, K., Csatho, B., Harbeck, K., Markus, T., Neumann, T., Siegfried, M.R., Zwally, H.J., 2020. Pervasive ice sheet mass loss reflects competing ocean and atmosphere processes. *Science*, **368**, 1239–1242. https://doi.org/10.1126/science.aaz5845

Sousan, S., Koehler, K., Hallett, L., Peters, T.M., 2016. Evaluation of the Alphasense optical particle counter (OPC-N2) and the Grimm portable aerosol spectrometer (PAS-1.108). *Aerosol Sci. Technol.*, **50**, 1352–1365. https://doi.org/10.1080/02786826.2016.1232859

Souverijns, N., Gossart, A., Lhermitte, S., Gorodetskaya, I. V., Kneifel, S., Maahn, M., Bliven, F.L., van Lipzig, N.P.M., 2017. Estimating radar reflectivity - Snowfall rate relationships and their uncertainties over Antarctica by combining disdrometer and radar observations. *Atmos. Res.*, **196**, 211–223. https://doi.org/10.1016/j.atmosres.2017.06.001

Souverijns, N., Gossart, A., Gorodetskaya, I. V., Lhermitte, S., Mangold, A., Laffineur, Q., Delcloo, A., Van Lipzig, N.P.M., 2018a. How does the ice sheet surface mass balance relate to snowfall? Insights from a ground-based precipitation radar in East Antarctica. *Cryosphere*, **12**, 1987–2003. https://doi.org/10.5194/tc-12-1987-2018

Souverijns, N., Gossart, A., Lhermitte, S., Gorodetskaya, I. V., Grazioli, J., Berne, A., Duran-Alarcon, C., Boudevillain, B., Genthon, C., Scarchilli, C., van Lipzig, N.P.M., 2018b. Evaluation of the CloudSat surface snowfall product over Antarctica using ground-based precipitation radars. *Cryosphere*, **12**, 3775–3789. https://doi.org/10.5194/tc-12-3775-2018

Testik, F.Y., Rahman, M.K., 2016. High-speed optical disdrometer for rainfall microphysical observations. *J. Atmos. Ocean. Technol.*, **33**, 231–243. https://doi.org/10.1175/JTECH-D-15-0098.1

Textor, C., Schulz, M., Guibert, S., Kinne, S., Balkanski, Y., Bauer, S., Berntsen, T., Berglen, T., Boucher, O., Chin, M., Dentener, F., Diehl, T., Easter, R., Feichter, H., Fillmore, D., Ghan, S., Ginoux, P., Gong, S., Grini, A., Hendricks, J., Horowitz, L., Huang, P., Isaksen, I., Iversen, T., Kloster, S., Koch, D., Kirkevåg, A., Kristjansson, J.E., Krol, M., Lauer, A., Lamarque, J.F., Liu, X., Montanaro, V., Myhre, G., Penner, J., Pitari, G., Reddy, S., Seland, Stier, P., Takemura, T., Tie, X., 2006. Analysis and quantification of the diversities of aerosol life cycles within AeroCom. *Atmos. Chem. Phys.*, **6**, 1777–1813. https://doi.org/10.5194/acp-6-1777-2006

Thompson, D.W.J., Solomon, S., Kushner, P.J., England, M.H., Grise, K.M., Karoly, D.J., 2011. Signatures of the Antarctic ozone hole in Southern Hemisphere surface climate change. *Nat. Geosci.*, **4**, 741–749. https://doi.org/10.1038/ngeo1296

Tittarelli, A., Borgini, A., Bertoldi, M., De Saeger, E., Ruprecht, A., Stefanoni, R., Tagliabue, G., Contiero, P., Crosignani, P., 2008. Estimation of particle mass concentration in ambient air using a particle counter. *Atmos. Environ.*, **42**, 8543–8548. https://doi.org/10.1016/j.atmosenv.2008.07.056

Tomasi, C., Vitale, V., Lupi, A., Di Carmine, C., Campanelli, M., Herber, A., Treffeisen, R., Stone, R.S., Andrews, E., Sharma, S., Radionov, V., von Hoyningen-Huene, W., Stebel, K., Hansen, G.H., Myhre, C.L., Wehrli, C., Aaltonen, V., Lihavainen, H., Virkkula, A., Hillamo, R., Ström, J., Toledano, C., Cachorro, V.E., Ortiz, P., de Frutos, A.M., Blindheim, S., Frioud, M.,

Gausa, M., Zielinski, T., Petelski, T., Yamanouchi, T., 2007. Aerosols in polar regions: A historical overview based on optical depth and in situ observations. *J. Geophys. Res. Atmos.*, **112**. https://doi.org/10.1029/2007JD008432

Tositti, L., Brattich, E., Masiol, M., Baldacci, D., Ceccato, D., Parmeggiani, S., Stracquadanio, M., Zappoli, S., 2014. Source apportionment of particulate matter in a large city of southeastern Po Valley (Bologna, Italy). *Environ. Sci. Pollut. Res.*, **21**, 872–890. https://doi.org/10.1007/s11356-013-1911-7

Turner, J., Bindschadler, R., Convey, P., Di Prisco, G., Fahrbach, E., Gutt, J., Hodgson, D., Mayewski, P., Summerhayes, C., 2009. Antarctic climate change and the environment. Cambridge, SCAR.

Turner, J., Phillips, T., Thamban, M., Rahaman, W., Marshall, G.J., Wille, J.D., Favier, V., Winton, V.H.L., Thomas, E., Wang, Z., van den Broeke, M., Hosking, J.S., Lachlan-Cope, T., 2019. The Dominant Role of Extreme Precipitation Events in Antarctic Snowfall Variability. *Geophys. Res. Lett.*, **46**, 3502–3511. https://doi.org/10.1029/2018GL081517

Tyynelä, J., Leinonen, J., Moisseev, D., Nousiainen, T., 2011. Radar Backscattering from Snowflakes: Comparison of Fractal, Aggregate, and Soft Spheroid Models. *J. Atmos. Ocean. Technol.*, **28**, 1365–1372. https://doi.org/10.1175/JTECH-D-11-00004.1

Tyynelä, J., Chandrasekar, V., 2014. Characterizing falling snow using multifrequency dual-polarization measurements. *J. Geophys. Res.*, **119**, 8268–8283. https://doi.org/10.1002/2013JD021369

Ulbrich, C.W., 1983. Natural variations in the analytical form of the raindrop size distribution. *J. Clim. Appl. Meteorol.*, **22**, 1764–1775. https://doi.org/10.1175/1520-0450(1983)022<1764:NVITAF>2.0.CO;2

Vagnoni, F., Illuminati, S., Annibaldi, A., Memmola, F., Giglione, G., Falgiani, A.M., Girolametti, F., Fanelli, M., Scarponi, G., Truzzi, C., 2021. Seasonal evolution of the chemical composition of atmospheric aerosol in Terra Nova Bay (Antarctica). *Atmosphere (Basel).*, **12**.

https://doi.org/10.3390/atmos12081030

Vajda, A., 2015. RAIN - Impacts of severe winter weather events on critical infrastructure. *RAIN WP2 Work. Past Sev. Weather Hazards*, Berlin, 27 Febr. 2015 20.

Vali, G., 1985. Nucleation terminology. *J. Aerosol Sci.*, **16**, 575–576. https://doi.org/10.1016/0021-8502(85)90009-6

Van Tricht, L., Huybrechts, P., Van Breedam, J., Vanhulle, A., Van Oost, K., Zekollari, H., 2021. Estimating surface mass balance patterns from unoccupied aerial vehicle measurements in the ablation area of the Morteratsch-Pers glacier complex (Switzerland). *Cryosphere*, **15**, 4445–4464. https://doi.org/10.5194/tc-15-4445-2021

Van Wessem, J.M., Reijmer, C.H., Morlighem, M., Mouginot, J., Rignot, E., Medley, B., Joughin, I., Wouters, B., Depoorter, M.A., Bamber, J.L., Lenaerts, J.T.M., Van De Berg, W.J., Van Den Broeke, M.R., Van Meijgaard, E., 2014. Improved representation of East Antarctic surface mass balance in a regional atmospheric climate model. *J. Glaciol.*, **60**, 761–770. https://doi.org/10.3189/2014JoG14J051

Vaughan, D.G., J.C. Comiso, I. Allison, J. Carrasco, G. Kaser, R. Kwok, P. Mote, T. Murray, F. Paul, J. Ren, E. Rignot, O. Solomina, K.S. and T.Z., 2013. Observations: Cryosphere, in: *Climate Change 2013: The Physical Science Basis. Contribution of Working Group I to the Fifth Assessment Report of the Intergovernmental Panel on Climate Change*. Cambridge University Press, Cambridge, United Kingdom and New York, NY, USA. https://doi.org/10.1007/978-1-4020-4411-3_53

von Lerber, A., Moisseev, D., Bliven, L.F., Petersen, W., Harri, A.M., Chandrasekar, V., 2017. Microphysical properties of snow and their link to Ze-S relations during BAECC 2014. *J. Appl. Meteorol. Climatol.*, **56**, 1561–1582. https://doi.org/10.1175/JAMC-D-16-0379.1

Wang, J., Georgakakos, K.P., 2005. Effects of cold microphysical processes on the

surface precipitation variability of nonsquall tropical oceanic convection. *J. Geophys. Res. Atmos.*, **110**, 1–21. https://doi.org/10.1029/2005JD005787

Wang, P.K., 2013. Physics and dynamics of clouds and precipitation. Cambridge University Press.

Wang, X., Zhang, L., Moran, M.D., 2014. Development of a new semi-empirical parameterization for below-cloud scavenging of size-resolved aerosol particles by both rain and snow. *Geosci. Model Dev.*, **7**, 799–819. https://doi.org/10.5194/gmd-7-799-2014

Wehrmann, D., 2018. Critical geopolitics of the Polar Regions: An inter-American perspective. Routledge.

Welker, R.W., 2012. Size Analysis and Identification of Particles, in: *Developments in Surface Contamination and Cleaning*. Elsevier, pp. 179–213. https://doi.org/10.1016/B978-1-4377-7883-0.00004-3

Werner, K., 2021. Year of Polar Prediction – enhance observations to provide improved forecasts in polar regions. *Polarforschung*, **89**, 81–84. https://doi.org/10.5194/polf-89-81-2021

Wolff, E.W., Legrand, M.R., Wagenbach, D., 1998. Coastal Antarctic aerosol and snowfall chemistry. *J. Geophys. Res. Atmos.*, **103**, 10927–10934. https://doi.org/10.1029/97jd03454

Wood, N.B., 2011. Estimation of snow microphysical properties with application to millimeter-wavelength radar retrievals for snowfall rate. Colorado State University.

Wood, N.B., L'Ecuyer, T.S., Vane, D.G., Stephens, G.L., Partain, P., 2013. Level 2C Snow-Profile Process Description and Interface Control Document, Algorithm Version PR04 [WWW Document]. URL http://www.cloudsat.cira.colostate.edu/ICD/2C-SNOW-PROFILE/2C-SNOW-PROFILE_PDICD_P_R04.pdf (accessed 12.15.21).

Worm, B., Lotze, H.K., 2021. Marine biodiversity and climate change, in: *Climate Change*. Elsevier, pp. 445–464.

Wouters, B., Gardner, A.S., Moholdt, G., 2019. Global glacier mass loss during the GRACE satellite mission (2002-2016). *Front. Earth Sci.*, **7**, 96. https://doi.org/10.3389/feart.2019.00096

Yuter, S.E., Kingsmill, D.E., Nance, L.B., Löffler-Mang, M., 2006. Observations of precipitation size and fall speed characteristics within coexisting rain and wet snow. *J. Appl. Meteorol. Climatol.*, **45**, 1450–1464. https://doi.org/10.1175/JAM2406.1

Zemp, M., Huss, M., Thibert, E., Eckert, N., McNabb, R., Huber, J., Barandun, M., Machguth, H., Nussbaumer, S.U., Gärtner-Roer, I., Thomson, L., Paul, F., Maussion, F., Kutuzov, S., Cogley, J.G., 2019. Global glacier mass changes and their contributions to sea-level rise from 1961 to 2016. *Nature*, **568**, 382–386. https://doi.org/10.1038/s41586-019-1071-0

Zhang, L., Wang, X., Moran, M.D., Feng, J., 2013. Review and uncertainty assessment of size-resolved scavenging coefficient formulations for below-cloud snow scavenging of atmospheric aerosols. *Atmos. Chem. Phys.*, **13**, 10005–10025. https://doi.org/10.5194/acp-13-10005-2013

Zhao, S., Yu, Y., He, J., Yin, D., Wang, B., 2015. Below-cloud scavenging of aerosol particles by precipitation in a typical valley city, northwestern China. *Atmos. Environ.*, **102**, 70–78. https://doi.org/10.1016/j.atmosenv.2014.11.051

Zheng, Q., Chen, R. sheng, Han, C. tan, Liu, J. feng, Song, Y. xuan, Liu, Z. wen, Yang, Y., Wang, L., Wang, X. qiang, Liu, X. jiao, Guo, S. hai, Liu, G. hua, 2018. Adjusting precipitation measurements from the TRwS204 automatic weighing gauge in the Qilian Mountains, China. *J. Mt. Sci.*, **15**, 2365–2377. https://doi.org/10.1007/s11629-018-4839-z

Zheng, T., Bergin, M.H., Johnson, K.K., Tripathi, S.N., Shirodkar, S., Landis, M.S., Sutaria, R., Carlson, D.E., 2018. Field evaluation of low-cost particulate matter sensors in high-and low-concentration environments. *Atmos. Meas. Tech.*, **11**, 4823–4846. https://doi.org/10.5194/amt-11-4823-2018

Zikova, N., Zdimal, V., 2016. Precipitation scavenging of aerosol particles at a rural

site in the Czech Republic. *Tellus, Ser. B Chem. Phys. Meteorol.*, **68**. https://doi.org/10.3402/tellusb.v68.27343